DOMAINS, PHASE COEXISTENCE AND EXTINCTION PHENOMENA IN HELICAL AND MODULATED ANTIFERROMAGNETS.

Being submitted for the the Degree of Doctor of Philosophy

at the University of Warwick by

Adrian Simon Pearce B.Sc. (Hull)

The Department of Physics, University of Warwick, UK.

The Institute Max Von Laue - Paul Langevin, Grenoble, France.

October 1991

CONTENTS OF THESIS

CHAPTER THREE

Experimental techniques.

CHAPTER FOUR

Phase coexistence (I).

CHAPTER FIVE

Phase coexistence (II)

(Under a temperature gradient).

CHAPTER SIX

The 20K phase transitions in Holmium.

CHAPTER SEVEN

Acting on chirality domains.

Acknowledgements

I have decided to be brief and factual in my thanks to the individuals and institutions that have contributed to the realisation of this thesis. This method should not be misconstrued as a lack of gratitude on my part, but should simply emphasize the profound thanks I wish to offer to all those mentioned.

Firstly to the two institutions (The University of Warwick and The Institute Max Von Laue-Paul Langevin, Grenoble.) where I have carried out the majority of my research, I am grateful for the provision of their excellent scientific facilities. The extended use of the resources of the Laboratoire Louis Neel, Grenoble and LURE, Paris are also acknowledged.

I would like to offer special thanks to my two thesis directors, Prof. S B Palmer of the University of Warwick and Dr J Baruchel of the European Synchrotron Radiation Facility. Their advice and encouragement have been a huge asset to me over the last years and one from which I believe I have profited greatly. Thanks are also given to J. Kulda for his ever helpful comments and discussion.

The expert technical assistance of A. Draperi (CNRS), P. Keay (ILL), T. Manning (ESRF), J. Reed & S. York (Warwick University) and T. Aspinwall (Hull University) must also be acknowledged. Their experience was frequently sought and always given generously, for this I am very grateful.

Personal thanks are given to Jon, Andy, Michel, Marie-Rose, Chap, the SSB, Saxo and Rola & Maya for being more than "just there".

Finally I would like to thank both my parents and my wife to be, Kirsten for giving me their support throughout these last three years. It is to them that I dedicate this thesis.

Declaration

The work contained in this thesis is my own, except where specifically stated as otherwise, and was based at the Department of Applied Physics at the University of Warwick and the Institute Max Von Laue-Paul Langevin, Grenoble.

No part of this work has previously been submitted to this or any other academic institution for admission to a higher degree. Some of the work has already appeared in the form of publications which are listed at the end of the reference section.

ABSTRACT

Using neutron diffraction and topography techniques the phase transitions, domain structures and phase coexistence of a range of modulated antiferromagnetic materials have been studied.

(i) In chromium-0.6 atomic percent silicon (a modulated antiferromagnet) an inhomogeneous silicon content was detected by analysing backscattered x-rays from an electron beam. The variation of the magnetic intensity detected on a series of neutron topographs and the broadening of the first order transitions of Cr-0.6 at.% Si (as observed by neutron diffraction and elastic constant measurements), were attributed to this variation of silicon concentration within the sample.

(ii) The helimagnetic-ferromagnetic phase boundaries of terbium and manganese phosphide have been imaged using neutron and synchrotron topography under both zero and applied field conditions. Their resultant shapes are explained using a dimensionless parameter (ϵ), representing the ratio of the competing energy terms of the system, and taking into account the applied field, the ferromagnetic volume and sample dimensions.

The nucleation and growth of ferromagnetic regions isolated in the helimagnetic phase of a single crystal MnP sample have been studied under the application of a temperature gradient. With an additional applied field gradient the coexistence of three magnetic phases together with the associated triple point were observed. The third (fan) phase was nucleated from within the helimagnetic-ferromagnetic interface on the application of a b axis field. The Ferro-Fan and Ferro-Heli interface shapes can be understood in terms of magnetostatic and elastic energy considerations whilst the Heli-Fan interface is as yet not understood.

(iii) An anomalous increase, at around 20K in the integrated intensity of the 002$\pm\tau$ magnetic reflections of holmium has been modelled by the RED extinction theory. The resultant parameters are discussed in relation to the coexistence of regions of different interplanar turn angle as seen near the commensurate lock-in structures described in the spin slip model. The magnetisation data of this sample shows a field dependent, relative maximum of the c axis component of the magnetic moment below 20K. This is explained by the stabilisation of commensurate states as observed in the neutron diffraction data.

(iv) On cycling in temperature within the helimagnetic phase of MnP the reduction of the magnetic integrated intensity is interpreted (through a secondary extinction treatment) as a result of an increase in the average chirality domain size (from 8 to 10 μm). A mechanism is proposed for the temperature driven movement of chirality domain walls, which also accounts for the possibility of domain wall annihilation, leading to an increase in the average chirality domain size of the sample.

INTRODUCTION

The ability of neutrons to penetrate into most materials with a limited amount of absorption, whilst being sensitive to magnetic phenomena (through the interaction with the magnetic moment of the neutron) makes them an invaluable probe for the magnetic structure of bulk materials. Moreover by recording the spatial distribution of the diffracted intensity, the variation in magnetic behaviour across the sample can be imaged. For example neutron topography can be used to visualise magnetic domain structures and image phase coexistence in first order magnetic transitions.

The above simple description forms the basis of neutron diffraction topography (Schlenker & Baruchel (1988)) which has been used to image a variety of magnetic domain structures including the ferromagnetic domains of CoFe (Schlenker &Schull (1973)), and the antiferromagnetic domains in NiO (Baruchel et al.(1977) and Cr (Ando & Hosoya (1978)).

Polarised neutron diffraction topography has allowed the chirality domain structure of the helical antiferromagnet terbium to be observed (Baruchel et al (1981)). Chirality domains are distinguished by the lefthanded or righthanded rotation of the helimagnetic structure and have been imaged in a range of materials including holmium, manganese phosphide and terbium

The shapes of these helical domains were observed to be dependent on sample history. On re-entering the helimagnetic phase given regions of the sample were found to retain the same rotation sense. This effect is called the "memory effect". In some cases even the size and shape of the domains were reproduced, but as chirality domains have been shown to be susceptible to changes in sample purity and crystalline quality then this effect is dependent on the conditions imposed on the sample.

In the pioneering work on pure chromium (a modulated antiferromagnet), Ando & Hosoya (1978) used neutron diffraction topography to image the propagation vector associated (τ) domains on both sides of the spin flip transition. The characteristic size of the τ domains observed in this investigation (mm^3) were used to disprove the proposed thermal activation model where the domain size was predicted to be several orders of magnitude lower.

We use a similar imaging of magnetic satellites to investigate the phase coexistence of the chromium-0.6 atomic percent silicon. This work reported in chapter four was undertaken in order to image the domain structure of this compound and to clarify the nature of both the spin-flip and the higher temperature modulated spin density wave to paramagnetic phase transitions following the reported broadening of the latter by Palmer et al. (1988).

Baruchel et al (1988) described the ferromagnetic-helimagnetic phase coexistence of manganese phosphide in terms of the competing energy interactions (magnetostatic and elastic) using the complementary techniques of neutron diffraction topography and synchrotron radiation topography.

In the present work the phase coexistence of several different systems is investigated in order to gain a better understanding of the movement and shape of the phase boundary during phase coexistence. The analysis of the magnitudes of the various energy terms (interface, magnetoelastic, magnetostatic, anisotropy...) indicates which ones have greatest influence on the phase coexistence. The phase boundary is described in terms of these relevant energy terms for both the temperature or magnetic field driven transitions for several different sample orientations.

The role of the defects on the nucleation and subsequent stabilisation of the second phase is, in addition, investigated by directionally driving the phase boundary across the sample surface under the application a temperature gradient.

The simultaneous application of magnetic field and temperature gradients are proposed for the observation of a third coexisting phase around the low temperature triple point in manganese phosphide. The nucleation of this third (fan) phase is shown to be dependent on the direction of the applied magnetic field. For a purely b axis field the fan phase can be produced in the boundary between the ferromagnetic and helimagnetic phases as suggested by the behaviour of the critical fields in this region (Shapira et al. (1981)). This first observation of the coexistence of these three phases with three distinct phase boundaries is described as a function of varying the applied magnetic field.

New interest was generated in holmium following the high resolution magnetic x-ray resonance studies carried out by Gibbs et al. (1985), and the subsequent proposal of the magnetic spin slip model. The elastic constant measurements of Bates et al (1988) showed the presence of a double anomaly around 20K, near the transition to the $^1/_6$ commensurate lock in phase and the possible onset of a conical structure. Drillat (1983) reported an unexpected increase in the magnetic integrated intensity of holmium in the same 20K region. These two facts were not accounted for in the framework of the existing model and led to the further experiments on holmium reported in this work

An extinction treatment of the integrated intensities of the $002\pm\tau$ magnetic satellites of holmium in the 20K region is given to describe the anomalous intensity increase. The physical assumptions used in the extinction treatments, as well as the values of the extinction parameters, are interpreted for the specific case of a helimagnetic material and are discussed in relation to the characteristics of the neutron data.

A c axis component of the magnetic moment of holmium is detected on the neutron diffraction data of the 110 nuclear reflection in the 20K region. Magnetisation measurements confirm this observed c axis component and these results are concurrent with the previously measured values of Koehler et al (1967). The presence of a c axis

component and the neutron diffraction data of the 002-τ satellites are discussed in relation to the commensurate lock in structures of the spin slip model.

The variation of temperature within the helimagnetic phase was reported to enhance the average chirality domain size (ACDS) on a single crystal terbium sample (Baruchel et al (1988b)). A similar investigation is performed here on the helimagnetic phase of manganese phosphide. The integrated intensities of the magnetic satellite reflections reduce when cycling within the helimagnetic phase. This reduction is attributed to an increase in the ACDS through a secondary extinction treatment. A model is presented for the movement of domain walls, which depends on the temperature variation of the propagation vector of the helical structure. This model is then expanded to describe the annihilation of domain walls and hence the increase in the ACDS.

CHAPTER ONE

THE MAGNETIC PROPERTIES OF HOLMIUM, TERBIUM, MANGANESE PHOSPHIDE AND CHROMIUM - 0.6 % SILICON.

1.1 Introduction.

A brief description will be given of the spatial distribution of magnetic moments in helical antiferromagnetic ordering in terms of a characteristic inter planar turn angle (ϕ), and a helical propagation vector (τ). This system will then be extended to explain the two possible enantiomorphs of a helical system and their manifestation within a domain structure as a function of sample history.

The following sections will then describe the previous investigations of the three helimagnetic materials (terbium, holmium and manganese phosphide), which were studied in this investigation. As the two rare earths (Tb and Ho) have very similar electronic and magnetic structures, they will be initially treated together, before giving an in depth account of their individual magnetic structures. The fifth section of this chapter will be devoted to the magnetic ordering of manganese phosphide. The development of an understanding of all three materials will be described in chronological order so as to provide the reader with a thoroughly referenced guide to their magnetic properties.

The final compound described in this section will be the chromium-0.6 atomic percent silicon alloy, which exhibits a modulated antiferromagnetic structure. This section will include a description of the effect of a variation in the temperature and elemental composition on the magnetic order of the system. The domain size and distribution in the low temperature spin density wave phase will also be discussed in comparison to those previously observed in pure chromium.

The concluding remarks in the description of the magnetic properties of each material will provide the subject and background for the results presented in chapters four to seven.

1.2 Helimagnetism.

The helimagnetic structure basically consists of a series of ferromagnetically ordered planes, which are systematically misoriented along the stacking direction by an interplanar turn angle (ϕ) as shown in figure 1.1. This stacking direction is termed the propagation vector of the helix (τ), and corresponds to the magnetically hard axis of the system. The magnitude of the propagation vector is dependent on the value of the interplanar turn angle as described by the following simple relationship,

$$|\tau| = \frac{\phi}{x} \qquad (1).$$

In the specific cases studied here, the moment is held in the plane as a result of crystalline anisotropy, and interacts ferromagnetically through a positive exchange constant (J_0) with its "in plane" neighbours. The interaction between an atom and successive ferromagnetic planes can be represented by a series of exchange constants J_1, J_2... which correspond to the neighbouring plane and next nearest plane interactions. The total exchange for a given layer can be written as :

$$E_{Exchange} = J_0 + 2J_1 \cos\phi + 2J_2 \cos 2\phi + ... \qquad (2).$$

By considering the limited interaction of the nearest and next nearest ferromagnetic planes to a given atom, and differentiating this expression with respect to the interplanar turn angle the following condition for a minimum exchange energy can be derived,

$$-J_1 \sin\phi - 4J_2 \cos\phi \sin\phi = 0 \qquad (3).$$

There are two possible solutions to this equation and they are given as

$$\sin\phi = 0 \qquad (4)$$

or

$$\cos\phi = \frac{-J_1}{4J_2} \qquad (5)$$

If $\sin\phi$ is zero valued then it is possible to describe two solutions to equation (4): when ϕ = zero radians this describes the condition for ferromagnetic ordering, and when $\phi=\pi$ radians this describes a classical antiferromagnet. Equation (5) describes a helimagnetic structure with an interplanar turn angle of ϕ radians for the condition where $|J_1/4J_2|$ is less than one.

As the interplanar interaction is long range (as specified through the RKKY interaction) taking the simple approximation of a two nearest neighbour interaction does not allow a precise prediction of the interplanar turn angle. Indeed, it is often necessary to take into account up to eight exchange constants when interpreting experimental data. Determining these constants involves measuring the temperature variation of the magnon dispersion relationships. Whilst being a very accurate method to measure the temperature variation of ϕ, it is also very cumbersome and time consuming.

A more direct approach to observing the temperature evolution of interplanar turn angle is to measure the 1st order satellite separation, and substitute into the following equation :

$$\delta\theta = \text{Arcsin}\frac{\lambda}{c}\left(1+\frac{\phi}{2\pi}\right) - \text{Arcsin}\frac{\lambda}{c}\left(1-\frac{\phi}{2\pi}\right) \qquad (6)$$

where $\delta\theta$ is the angular separation of the first order satellites, λ is the wavelength of the incident neutron beam and c is the samples lattice constant.

From this elementary description of helimagnetism two possible senses to the spiral structure can be evoked; right handed and left handed, as illustrated in figure 1.2.

PAGE(S) MISSING
NOT AVAILABLE

FIGS. 1·1 + 1·2.

Both enantiomorphs have equal energy considerations, thus it is reasonable to infer that a domain structure should exist between regions of opposite spiral sense in the helimagnetic phase. The formation of these domains is expensive in terms of domain wall energy, because unlike their classical antiferromagnetic counterparts, decreasing domain size does not reduce the magnetostatic energy as helical domains do not have a net ferromagnetic moment. Thus the presence of these thermodynamically unstable spiral domains would actually increase the energy of the system through the formation of domain walls. These domains are termed chirality domains.

1.3 Chirality domains.

Following the above description of chirality domains there are very few reasons in terms of energy why a helimagnetic sample should be divided into domains, as it is clearly favourable to have a single domain phase, hence saving on domain wall energy. Chirality domains do however exist and have been previously observed in a variety of helimagnetic compounds as reviewed by Baruchel et al. (1990).

The shape of these domains is dependent on the sample history. If the sample passes into the helimagnetic phase from the paramagnetic phase the domain shape will be random with respect to crystalline axes and anisotropy directions. These domains are termed "P" domains. Whilst on entering the helimagnetic phase from the ferromagnetic phase the domains take the form of stripes aligned parallel to the ferromagnetic domains, and are termed "F" domains. These two domain configurations are illustrated in figure 1.3.

The formation of "F" domains has since been attributed (Mitsek 1973, Palmer 1975, Lajzerowicz & Niez 1979) to nucleation and growth of the helimagnetic region from within the ferromagnetic Bloch walls. The Bloch walls are basically a region of the sample where the moments in one domain are rotated to the direction of the moments in the neighbouring domain. This directional rotation (chirality) is conserved on passing into

Figure 1.3 : The characteristic domain shapes observed in chirality domains.

"F" domains

"P" domains

the helimagnetic phase and is thought to be one of the reasons why "F" domains exhibit such a strong "memory effect". That is, where a given region of the sample returns to the same chirality on successive cycling into the ferromagnetic phase. This is no longer the case when passing into the paramagnetic phase, as the Bloch walls are then lost. However, a similar memory effect also exists in "P" domains, but in this case the driving mechanism is thought to be an interaction with lattice defects and impurity sites. A similar effect has been observed in the case of antiferromagnetic domains in MnF_2 (El Kadiri et al 1986).

An interesting question related to "P" domains is why do chirality domain walls form in apparently random directions? Calculations have been performed on the simplest possible boundary, where the domain walls are perpendicular to the propagation vector of the helix (Thomas and Wolf 1964, Hubert 1974 and MacKenna 1980). Much more complex situations can be envisaged, for example when the domain walls are parallel to the propagation vector, which could imply a large wall formation energy. However no preferential orientation of "P" domain walls has been observed on previously recorded neutron topographs.

Palmer et al (1986) studied chirality domain size and shape as a function of impurity concentration. On increasing the impurity content they found that the average chirality domain size was reduced. The reduction of domain size was so profound for the case of terbium samples that below resistance ratios of 50 no chirality domains were imaged. This was either as a consequence of the average domain size being smaller than the 60 μm resolution of the instrument, or just being smaller than the crystal thickness which was typically 300 μm.

1.4 The heavy rare earths; terbium and holmium.

Terbium and holmium both crystallize into an hexagonal close packed structure, with a $P6_3/nnc$ space group. Their electronic configurations are given by the following expression;

$$(Pd)^{46}\ 4f^{n}\ 5s^2\ 5p^6\ 5d^1\ 6s^2 \qquad (7)$$

where n is 8 in the case of terbium and 10 for holmium. The two additional 4f electrons in the electronic structure of holmium do not change the trivalency shown by terbium. Moreover, because the inner 4f electrons are shielded by the outer 6s electrons the whole series of heavy rare earths exhibit very similar chemical properties. However, these 4f electrons have a high angular momentum, and as a result determine the magnetic properties of the rare earth series.

The direct exchange interaction between the 4f electrons of atoms which occupy neighbouring sites in the lattice is very weak, as their corresponding wavefunctions do not overlap. Nevertheless, their indirect exchange interaction through the polarization conduction band electrons can be explained by the RKKY interaction proposed by Ruderman & Kittel (1954), Kasuya (1956) and Yosida (1957). This is a long range interaction, which exhibits large variations in magnitude and sign. Changes in sign of the exchange interaction are possible at a lattice site as a result of the changes in the interatomic separation and the periodic spin density. This is illustrated by the profound difference in the magnetic ordering of terbium and holmium as a result of introducing two extra electrons into the partially filled 4f shell.

The competing exchange interactions between neighbouring atoms not only allow the description of ferromagnetic and antiferromagnetic systems, but also helimagnetic structures as shown by Villain (1959). Both terbium and holmium exhibit such a structure

on cooling from the paramagnetic phase with characteristic Néel points at 229K, and 132K respectively (Koehler, 1965).

1.4a Terbium.

The temperature dependence of the magnetic structure of terbium has been thoroughly charted by Koehler et al. (1962, 1963, 1965) using neutron diffraction measurements on large single crystals, and with the complementary magnetisation techniques as employed by Flippen (1963). The magnetic phase diagram of terbium is illustrated in figure 1.4. as measured by Drillat et al. (1984). Throughout the ordered phases the magnetic moment is confined to the hexagonal basal plane by large anisotropy fields (Rhyne & Clark 1967). Magnetisation measurements of Hegland et al. (1963) indicate that the $(10\bar{1}0)$ or b axis is the easy axis, with a saturated magnetic moment of 9.34 μ_B at very low temperatures. The helical antiferromagnetic phase exists over a narrow temperature range with a variation in the interplanar turn angle from 20.5° at T_N (229K), passing through a minimum of 17° to 18.5° at T_C (221K) as recorded by Koehler (1965) and Dietrich & Als-Nielsen (1967).

Neutron diffraction data (reported by Jiles et al. 1981), taken on a high purity single crystal sample by Crangle exhibit a very different behaviour, with the interplanar turn angle increasing linearly from 15° at T_C to 26.7° at T_N. A similar linear temperature variation of ϕ was also measured in terbium by Drillat (1983) and is illustrated in figure 1.5. Discrepancies such as those mentioned above also occur in the measured transition temperatures of different single crystal terbium samples. This was initially thought to be a result of the hysteresis in T_C on warming and cooling through the ferromagnetic transition. However, values of T_N have also been previously quoted over a large temperature range (223.3K to 230.0K) by various authors (Jiles et al. 1984), when this transition is thought to be second order and non-hysteretic.

Figure 1.4 : The critical field of terbium as deduced from magnetisation measurements taken by Drillat (1983).

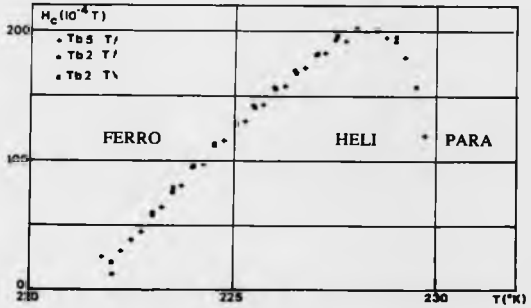

Figure 1.5: The temperature variation of the interplanar turn angle of terbium, as measured by Drillat (1983).

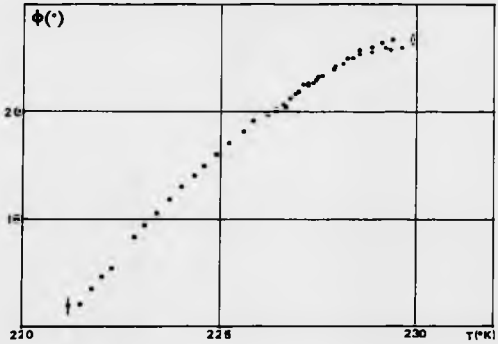

Figure 1.6: Passing into the helimagnetic phase under the influence of an externally applied magnetic field.

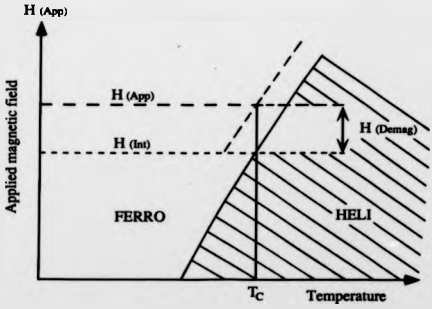

A more convincing explanation can be found by considering the fine balance between the exchange interaction energy, and the basal plane anisotropy. Enz (1960) showed that the exchange interaction favours the helimagnetic phase, but the basal plane anisotropy increases on decreasing the temperature, thus favouring the ferromagnetic phase (Mackintosh 1977). In the terbium system these two terms are so critically adjusted that the antiferromagnetic phase is only stable over a temperature range of ≈ 10 K. Consequently it is not surprising that the critical field required to destabilize the helimagnetic structure is dependent on sample history and purity as shown by Palmer et al. (1979). As the magnetic ordering of terbium is particularly sensitive to the effects of impurities this clearly necessitates high purity, high quality single crystal samples in order to reduce spurious results related to impurity effects.

Cooling below T_C (≈ 221K), or applying a sufficient magnetic field whilst in the helical phase will drive the sample into a ferromagnetic state. Considering the field driven case (illustrated in figure 1.6), the internal field (H_{Int}) of the sample can be determined at a given sample temperature from the externally applied field (H_{App}), and the demagnetising field (H_{Demag}) produced by the ferromagnetic volume of the sample. This relationship can be represented as,

$$H_{Int} = H_{App} - H_{Demag} \qquad (8).$$

Assuming the internal field is constant across the transition, then the application of an external magnetic field to the sample at a temperature T such that $T_C < T < T_N$ will drive the sample into the ferromagnetic phase. The constant internal field will be produced from the arrangement of magnetic phases within the sample. This implies from (8) that H_{Demag} will increase when H_{App} is increased over the applied field range of phase coexistence. The calculation of the conditions required to produce a constant internal field can be seen (chapter four), to help the understanding this phase coexistence process.

The modification of the demagnetising field can be inferred from the change in the arrangement of the ferromagnetic and helimagnetic phases within the sample. Both of these phases can be imaged using polarised neutron diffraction topography on the magnetic reflections of the sample. The imaging of the ferromagnetic-helimagnetic phase coexistence is made easier (than in the zero field case) on the application of a magnetic field as this stabilises the phase boundary by producing a range of applied field values in which the sample will undergo phase coexistence.

The temperature driven transition does not exhibit a temperature range for the phase coexistence in zero field, thus the phase transition is almost instantaneous and very difficult to image. However, if the phase coexistence could be imaged, then it would reveal a phase boundary orientation which is no longer dominated by demagnetising effects. In this case there would be a competition between the limited magnetostatic energy term (related to the ferromagnetic domains), the phase boundary energy, and elastic compatibility conditions. These situations will be described in chapter four.

1.4b Holmium.

Holmium exhibits a helimagnetic phase in which the propagation vector of the helix is parallel to the hard magnetic axis (c axis), with a magnetic moment of 10.9 μ_B being held in the basal plane (Rhodes et al. 1958). The transition from a helical state to a "ferromagnetic state" (T_C) was first observed by Gerstein et al. (1957) at ~ 20K. Shortly afterwards Strandburg et al. (1962) showed the b axis to be the easy axis (as in terbium), and measured an extrapolated effective magnetic moment of 10.34 μ_B in this direction. On passing through T_C they observed a spontaneous magnetisation of 1.7 μ_B in the c direction. This value was later confirmed in the neutron diffraction data of Koehler et al. (1966) and a reduced value of 9.5 μ_B was reported for the component of the magnetic moment which remains in the basal plane configuration. The interplanar turn angle was seen to decrease linearly from $51^o \pm 1^o$ at 133K to 30^o at approximately 20K, where it

remains constant down to 4.2K in zero field conditions (Koehler et al. 1967). However on performing the same interplanar turn angle measurements on two different holmium crystals Koehler et al. (1966) observed dramatically different results. This sample dependency of turn angle variation was attributed to the different impurity distributions of each sample. The magnetic phase diagram of holmium which resulted from this work is illustrated in figure 1.7.

Koehler et al. (1966) also observed higher order magnetic satellites in the diffraction patterns of holmium from ~45K to base temperature. These higher order satellites indicated a distortion of the previously postulated perfect helical structure. A model in which the moments were bunched around the hexagonal basal plane anisotropy directions was proposed in order to describe the distortion in the low temperature "conical" phase. Felcher et al.(1976) studied the 5th and 7th harmonics and observed additional 3rd order satellites on both a $Ho_{0.9}Sc_{0.1}$ alloy and a pure holmium sample. From their results they proposed an additional modulated amplitude to the bunched basal plane magnetic moment model of Koehler et al (1966).

Following reported ultrasonic attenuation anomalies near 24K (Tachiki et al. 1974, Lee et al. 1972) and 90K (Simpson et al. 1976 and Lee et al. 1975), Tindall et al. (1977) performed high resolution capacitance dilatometric measurements of thermal expansion along both a and c axis. They were unable to observe any anomalous behaviour at 90K, but the existence of a further transition at 25K was confirmed. A neutron diffraction study by Pechan & Stassis (1984) also indicated points of inflection in the temperature variation of the magnetic propagation vector which corresponded to a commensurability with the chemical lattice. This work was not confirmed by Drillat et al. (1984), who found no evidence of incommensurate-commensurate effects in the temperature dependence of the helical interplanar turn angle.

With the advent of magnetic x-ray scattering and its natural application to the holmium system, an investigation of the incommensurate magnetic spiral was undertaken

Figure 1.7: The magnetic phase diagram of holmium as measured by Koehler et al . (1967) using neutron diffraction techniques.

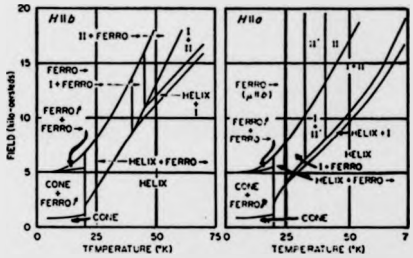

by Gibbs et al. (1985). The increased resolution provided by this technique allowed the observation of several "lock in" transitions at modulation wavevectors of $^1/_6$, $^2/_{11}$ and $^5/_{27}$. This data is illustrated along with previously measured neutron data in figure 1.8.

The bunching of moments around the six equivalent easy directions was not sufficient to explain the $^2/_{11}$ and $^5/_{27}$ lock in structures. Bohr et al. (1986) describe in a related paper the "spin slip system", which by allowing a periodic absence of one layer in the bunching around the easy basal plane axes, gives a suitable explanation to the additional order satellites seen in the earlier neutron diffraction work. Two examples of the proposed arrangement of moments in the "spin slip" model are given in figure 1.9 for the $^1/_6$ and $^2/_{11}$ commensurate structures. The spin slip system has been related to ultrasonic attenuation data taken around the Curie point and at the higher temperature (96K) $^1/_4$ commensurate modulated wave vector by Bates et al. (1988). However the double anomaly they observed at 24.5K in the ultrasound work was not in keeping with the spin slip theory. This fact and the increased neutron intensity observed by Drillat (1983) on passing through the ferromagnetic transition prompted the present study of the low temperature properties of holmium.

This study is limited to small magnetic fields < 3kOe, thus neglecting the more exotic structures observed in high fields, such as the "helifan" structure of Jensen & Mackintosh (1990), and the devils staircase structure which was observed by Cowley et al.(1990). However, several commensurate "lock in" structures were studied, and this neutron diffraction data was analysed using several extinction theories in order to explain the anomalous intensity increase.

Both magnetisation and neutron diffraction data were taken in an attempt to trace the c axis component of the magnetic moment (reported by Koehler et al. (1966)), but which had not been detected in the neutron diffraction measurements of Cowley & Bates (1988). This discrepancy leads to ambiguity about the "ferromagnetic component" in the conical phase and the general low temperature structure of holmium.

Figure 1.8: The temperature variation of the interplanar turn angle of holmium as measured by Gibbs et al (1985) using magnetic x ray scattering (open circles) and neutron diffraction data (closed circles).

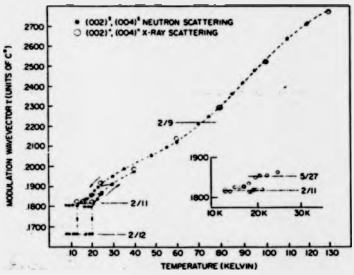

Figure 1.9: The basal plane magnetic moment distribution for the "spin slip system".

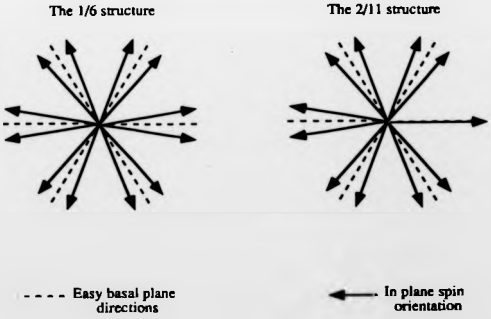

1.5 Manganese phosphide (MnP).

The long range RKKY interaction resulting from a localised moment system can also be applied to manganese phosphide just as for the two heavy rare earths, thus allowing the description of a helical antiferromagnetic phase. The transition from a ferromagnetic phase to a helical phase is also dependent on the minimisation of the relation between the interplanar exchange interaction and the in-plane crystal field anisotropy considerations.

Contrary to the rare earths, manganese phosphide crystallises into an orthorhombic structure with Pbnm space group as shown in Figure 1.10. The magnetic properties of manganese phosphide were first investigated by Huber & Ridgley (1964) in which they observed a ferromagnetic transition with a Curie point at 291.5K. Since then Ishizaki et al.(1971), Komatsubara et al.(1964, 1970, 1974), Obara (1980) and Shapira et al.(1981) have all studied the magnetic properties of MnP in detail. A precis of this work is best illustrated through the two magnetic phase diagrams depicted in Figure 1.11 for a) an applied c axis and b) a b axis field.

Neutron diffraction studies by Forsyth et al. (1966) and Felcher (1966) indicated the onset of a double helical structure (figure 1.12) at a Néel temperature (T_N=47K). The propagation vector of the helix is parallel to the a axis (in the axial system defined by Huber & Ridgley). The projection of the helical structure onto the (b,c) plane was thought to have an elliptical envelope, with associated components of the magnetic moment of 1.74 and 1.41 μ_B per Mn atom respectively. However the saturated magnetic moment was measured as 1.29 μ_B at 4.2K; a value which is independent of the direction of the applied field. Hiyamizu & Nagamiya (1971) proposed a model to explain this, with the moments being bunched around the c axis, thus explaining the apparently elliptical behaviour, whilst maintaining an isotropic distribution of the magnitude of the magnetic

Figure 1.10: The unit cell of the orthorhombic crystal structure of MnP.

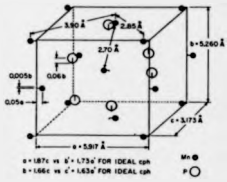

Figure 1.11: The critical field values of manganese phosphide for an applied field along a) the c axis (Huber & Ridgley, 1964) and b) the b axis (Shapira et al. 1981).

a)

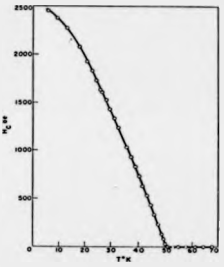

b)

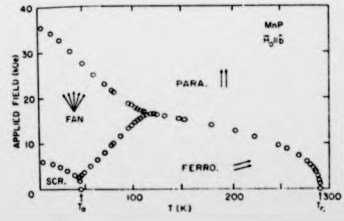

Figure 1.12: The double spiral structure as observed in MnP.

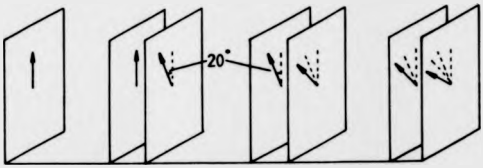

Figure 1.13: The temperature variation of the linear thermal expansion in MnP.

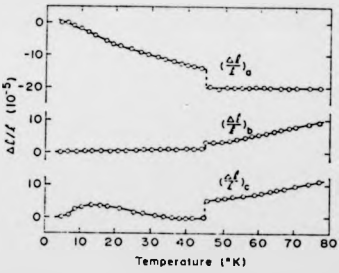

The above data contains an error. The graphs labelled Δl/l for the **a** and **b** axes should be reversed so that on descending the page the graphs represent the thermal expansions along the **b**, **a** and **c** axes respectively.

moment in the (b,c) plane. This structure was later confirmed by Moon (1982) in work on neutron polarisation analysis.

The linear thermal expansions measurements of Okamoto et al.(1968) show large magnetostrictive effects ($\Delta l/l = 10^{-4}$) on passing through the ferromagnetic-helimagnetic transition (figure 1.13). These magnetostrictive effects are sufficient to allow an indirect observation of the phase coexistence in MnP using synchrotron radiation topography as shown by Baruchel et al. (1988).

Early neutron diffraction topography measurements of the chirality domain structure of manganese phosphide (Patterson et al. 1985) taken on a spark cut and chemically etched sample showed a very uneven relative domain population. After polishing the sample surface, the preferential chirality selection was lost and the relative domain population became very near to unity. The reason for the imbalance in domain population was thought be a result of surface impurities or stress centres which were consequently removed on polishing. But on the application of a uniaxial stress along the b axis of the sample the average chirality domain size was reduced, but the relative domain populations remained very close to unity.

The preferential population of a specific chiral state is known to occur under an externally applied field in MnSi (Shirane et al 1983), and can be produced in $ZnCr_2Se_4$ by the simultaneous application of orthogonal electric and magnetic fields (Siratori et al. 1980). Unfortunately neither of these two structures have yet been imaged by polarised neutron topography due to problems of sample preparation and resolution limitations.

The above reported reduction of the average chirality domain size of manganese phosphide could be caused by local stress points forming within the sample as a result of a non uniform application of stress. The helimagnetic-ferromagnetic transition temperature of the MnP system is known to be stress dependent (Hirahara 1968) and hence the application of a stress gradient would provide a multitude of nucleation centres,

thus reducing the average chirality domain size. The effect of defect induced stresses will be investigated in chapter five.

From the a magnetic phase diagram (for an applied c axis field), it is clear that it is only possible to produce chirality domains by passing from the ferromagnetic phase. These domains will be parallel to ferromagnetic domain walls in the high temperature ferromagnetic phase, as previously observed by Patterson et al. (1985). However, on the application of a b axis field the helimagnetic phase can be entered from either the ferromagnetic phase or (in fields larger than approximately $2.5 .10^{-2}$ Tesla) from the fan phase. Such a phase diagram (figure 1.11b) allows the possibility of imaging (during phase coexistence) the meeting point of all three phase boundaries. This point is termed the triple point. The application of a temperature gradient and/or an applied field gradient across the sample should simplify the observation of this phenomenon. This investigation will be described in chapter five.

The value of the interplanar turn angle (ϕ) of helimagnetic materials is normally temperature dependent (in manganese phosphide it reduces on increasing temperature, thus approaching the ferromagnetic phase). In a recent investigation on terbium (Baruchel et al 1988) it was observed that the average chirality domain size (ACDS) of the sample was enhanced on increasing the sample temperature from 221K to 228K within the helimagnetic phase. This effect was thought to result from the temperature variation of ϕ. Manganese phosphide exhibits a helimagnetic phase which exists over a large temperature range (47K) and it is also possible to produce samples of high crystalline quality (resistance ratios up to 1300). Hence we decided to examine the effect of temperature cycling (within the helimagnetic phase of manganese phosphide), on the ACDS through a modulation of the interplanar turn angle.

This investigation will be shown in chapter seven where the increase of domain size will be inferred through an extinction theory treatment of the integrated intensity, as described by Baruchel and Schlenker (1989). The domain size returns to its initial value

after cycling into the paramagnetic phase. A mechanism for the movement and annihilation of domain walls will be produced.

1.7 Chromium-0.6 at.% Silicon.

$Cr_{1-x}Si_x$ can be described as an itinerant antiferromagnet for solid solutions where $x < 7$ atomic percent. Within this compositional range three distinct magnetic phases exist according to both temperature and composition (Cable 1977, Mizuki et al 1986), as illustrated in Figure 1.14. The region between 0 to 1 atomic percent of silicon undergoes a transition from the paramagnetic phase to a wholly incommensurate structure at lower temperatures. This incommensurate phase is subdivided into two regions as the incommensurate transversely modulated spin density wave (TSDW) is transformed into a longitudinally modulated one (LSDW) at the spin flip transition temperature. A schematic diagram of both these modulated spin density wave structures can be seen in figure 1.15.

Chromium silicon exhibits a BCC structure where the modulated spin density wave propagation vector τ is along one of the cube edges. Such a structure defines six possible transverse domains (where τ is perpendicular to two of the three crystalline axes), and three possible longitudinal domains (where τ is parallel to a given crystalline axis). Once cooled from the paramagnetic phase the crystal will be divided amongst these "τ" domains. The sample can be driven to a single domain by cooling in a magnetic field (Fawcett et al. 1988 used a 12 Tesla field for pure chromium) aligned along a crystalline axis. This facility was not used in these investigations and hence all the measurements reported here were carried out on a multi-domain sample.

At this point it is necessary to state that regions which have a given propagation vector τ at high temperature will be assumed to exhibit the same propagation vector at low temperatures as previously shown in the case of pure chromium (Ando and Hosoya 1978). This assumption is valid because of the similarities between the magnetic properties of these low silicon concentration compounds to those of pure chromium

Figure 1.14: The magnetic phase diagram of Cr-Si as a function of the percentage of silicon in the compound as reported by Mizuki et al (1986). The full and open circles represent the results of Endoh et al (1982) and Cable (1977) respectively.

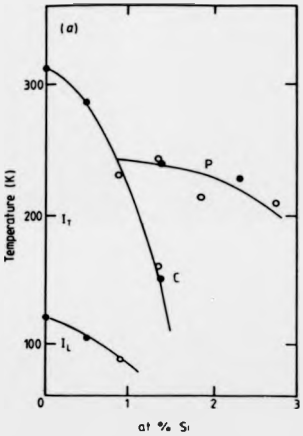

Figure 1.15a: A Schematic diagram of an Incommensurate Transverse Spin Density Wave

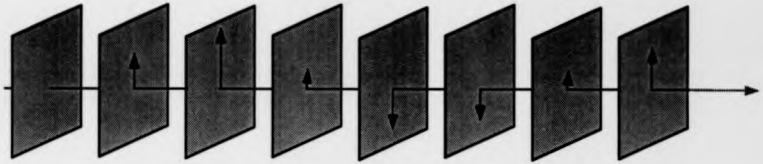

Figure 1.15b A Schematic diagram of a Commensurate Longitudinal Spin Density Wave

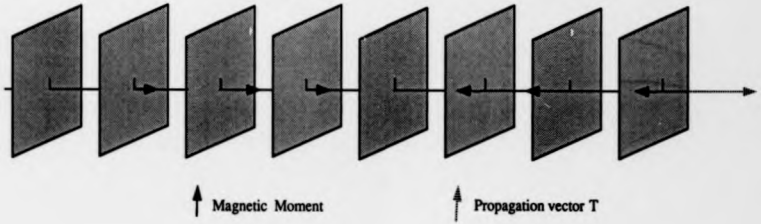

(Bacon 1961, Shirane & Takei 1962, Steinitz 1986, and Fawcett 1988). The two major differences between pure chromium and low concentration silicon-chromium alloys being the lowering of the transition points and the enhancement of the magnetic moment.

Previous studies have shown the transition from the paramagnetic (P) to the commensurate (C) state is of second order, whereas the P to incommensurate (I) state transition (in samples with a silicon content < 1%) is generally believed to be a first order one. However, close inspection of available data on the thermopower (Arajo et al, 1971) reveals that the P to L transition is sharp in pure chromium, but gets increasingly broad in Cr-0.4 at.% Si and Cr-0.9 at.% Si before sharpening again for silicon concentrations greater than 1%. It was this broadening of the P to L transition which suggested the possible existence of a complex magnetic structure.

Recent work carried out on the same single crystal as used in this investigation (Cr-0.6 at.% Si) proposed to explain the observed facts by considering the possible existence of a mixed magnetic phase over a temperature range of 10K (Palmer et al, 1988). This assumed phase coexistence could result from complicated magnetic interactions induced by the silicon presence, or more simply, it could be a direct result of silicon inhomogeneity across the bulk. This would appear to be feasible as metallurgically a noticeable degree of inhomogeneity is expected in such an alloy prepared by a process of zone refining. It was thus proposed that a reduction of the silicon inhomogeneity would be expected to reduce the width of the P to L transition.

As well as studying the phase coexistence of the Cr-0.6 at.% Si sample, it is possible to detect and image the actual antiferromagnetic domains present within the crystal structure. The size and behaviour of the magnetic domains in pure chromium have been previously investigated (Ando and Hosoya 1978), and a direct comparison to this data is made in order to investigate the effect that the introduction of silicon could have on the domain pattern of chromium.

CHAPTER TWO

NEUTRON DIFFRACTION FROM SINGLE CRYSTALS AND EXTINCTION PHENOMENA.

2.1 Introduction.

The aim of this chapter is to give an introduction to some of the more relevant aspects of neutron diffraction theory when applied to single crystal samples, and particularly those of high crystalline quality. This treatment is by no means exhaustive but it will hopefully provide the necessary background to understand the physics involved in this research.

As all the samples studied here are magnetic, we will make the distinction between magnetic and nuclear scattering and show their dependence on lattice spacing. The magnetic structure factor will then be derived for the particular case of a helimagnetic structure in a hexagonal close packed lattice, as exhibited by the two rare earths holmium and terbium. This system will then be further restricted to cover the effect of neutron polarisation on the diffraction from a given chirality domain of a 002±τ reflection. The necessary changes will then be discussed for adapting to the helimagnetic structure of orthorhombic manganese phosphide and the modulated spin density wave structure of body centered cubic chromium - 0.6 atomic percent silicon.

Having predicted the positions of the reflections from Bragg's law and their amplitude by defining the structure factor it is then important to define their intensity. This is done by describing the actual measured quantity in a diffraction experiment in terms of two limiting theoretical cases: an "ideally imperfect" crystal as described in the kinematical theory and a "perfect" crystal as in the dynamical theory.

The deviation of the experimentally detected intensity from that predicted by the kinematical theory will be described in terms of extinction theory. This section will be divided into two subsections; the first of which will deal with the description of secondary extinction from within the "mosaic model", as interpreted by Zachariasen (1967, 1968), Becker & Coppens (1974), and Sabine (1988, 1990). The free parameters of the mosaic model will be described in terms of measurable quantities and will be used to classify materials which exhibit secondary extinction. A distinction will be made between secondary and primary extinction and the latter will be described through the dynamical treatment of the random elastic deformation (RED) theory, as proposed by Kulda (1988).

2.2 Bragg diffraction.

The interaction of neutrons with magnetic materials can be described by the superposition of two different types of scattering, firstly from the interaction of the neutron with the nuclei of the material, and secondly the interaction of the magnetic moment of the neutron with the materials electronic magnetic structure.

The angular position of a neutron beam which has been diffracted by an ordered arrangement of such scattering centres can be predicted by considering a neutron (described by a wave vector $\mathbf{k}$), to be incident on a series of crystalline lattice planes, as illustrated in the real space representation of figure 2.1. The diffracted neutron can be described by a wave vector $\mathbf{k}'$ where the elasticity condition is fulfilled by the following relation,

$$|\mathbf{k}| = |\mathbf{k}'|.$$

Such an event can be equally described in reciprocal space (Figure 2.2) where the incident wave vector $\mathbf{k}$ is represented by the line AO, which is the radius of the circle centered at A and the diffracted wave is represented by the wave vector $\mathbf{k}'$, which is the radius of the circle centered at B.

Figure 2.1 : A real space representation of the diffraction geometry.

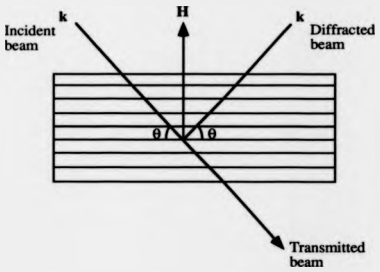

Figure 2.2 : A reciprocal space representation of the condition for Bragg diffraction from a crystalline lattice.

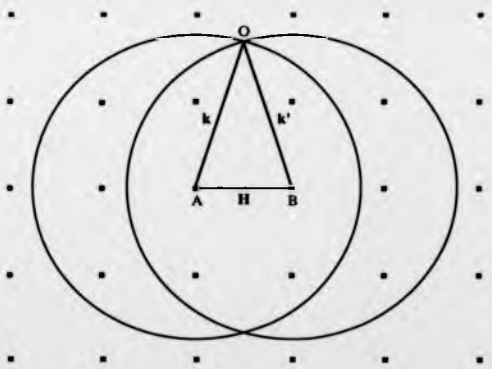

A diffraction vector (**H**) can be defined where $\mathbf{H} = \mathbf{k}' - \mathbf{k}$, which in the specific case of diffraction from the crystalline lattice must be equal to a reciprocal lattice vector (**h**) to satisfy Bragg's law. Hence the two points A and B must lie on two reciprocal lattice points. This is normally achieved by either rotating the sample position (which is equivalent to rotating the reciprocal lattice), or changing the incident wave vector by varying the incident neutron wavelength.

Figure 2.2 describes such a diffraction event where both wave vector states are matched to reciprocal lattice sites and hence the resultant diffraction vector H is equal to a reciprocal lattice vector (**h**). It follows from the sine rule that **h** can be written as,

$$\sin\theta = \frac{|\mathbf{h}|}{2|\mathbf{k}|}$$

$$|\mathbf{h}| = 2|\mathbf{k}|\sin\theta \qquad (9)$$

where the magnitude of the reciprocal lattice vector is given by

$$|\mathbf{h}| = \frac{2\pi n}{d_{hkl}} \qquad (10)$$

where n is an integer and d_{hkl} is the spacing of the reflecting planes of the crystal. The magnitude of the wave vector **k** is given by,

$$|\mathbf{k}| = \frac{2\pi}{\lambda} \qquad (11)$$

Hence by substituting the magnitudes of equations (10) and (11) into equation (9) the condition for elastic diffraction from a crystalline lattice can be defined in the customary form of Braggs law,

$$n\lambda = 2\,d\sin\theta \qquad (12)$$

2.2a The nuclear interaction.

The interaction of a neutron and an atomic nucleus is characterised by the nuclear scattering length (b). As the nucleus can be spatially described by a mathematical delta function, then the scattering length (which is proportional to the Fourier transform of the size of the nucleus), will have a constant value as a function of the incident neutron wavevector (figure 2.3) and hence is not reflection dependent.

Having predicted the angular positions of the neutrons diffracted by a crystalline lattice it is also necessary to predict what the relative amplitudes will be for a given crystallographic reflection. This information can be taken from the expression for the nuclear structure factor (F_{hkl}). which is defined as,

$$F_{hkl} = \sum_n b_n \exp\left(2\pi i\left(\mathbf{h}_n.\zeta_n\right)\right) \qquad (13)$$

where ζ gives a description of the unit cell of the sample.

2.2b Magnetic interaction.

Magnetic diffraction is more complex as it depends on the magnetic structure of the material. Just as for the nuclear interaction, the magnetic interaction of a neutron and a magnetic atom can be described by a magnetic scattering length but multiplied by a form factor. This form factor accounts for the spatial distribution of the electronic cloud, which can not be represented as a delta function, but takes a more extended form. The magnetic scattering length (p) is illustrated in Figure 2.3 where it has been multiplied by a magnetic form factor. This product is clearly reflection dependent in contrast to the previously described nuclear scattering length (b).

2.2c The magnetic structure factor.

The magnetic structure factor F(H) is defined as

Figure 2.3 : The nuclear and magnetic scattering lengths.

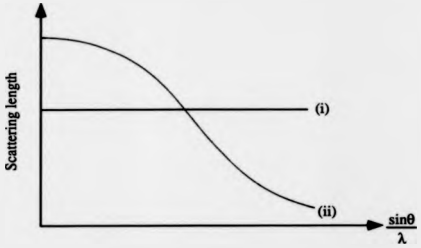

(i) The nuclear scattering length (b).

(ii) The magnetic scattering length (p) multiplied by the magnetic form factor.

Figure 2.4 : The definition of the unit vectors for an hexagonal close packed lattice.

With the c axis into the page where

o ; z = 0
+ ; z = 0.5 c

$$F(\mathbf{H}) = \Sigma_i P_i \exp i(\mathbf{H}.\mathbf{r}_i) \qquad (14)$$

where P_i is the diffraction amplitude of an ion at the ith position. The wave function of the neutron is a spinor with two components, P_i is a matrix of 2nd order,

$$P_i = f(\mathbf{H}) . \mu_N . \sigma . \mu_{\perp\perp} \qquad (15)$$

where $f(\mathbf{H})$ is the form factor of ith magnetic ion. μ_N is the magnetic moment of the neutron and σ are the Pauli spin matrices as described below,

$$\sigma_x = \begin{pmatrix} 0 & 1 \\ 1 & 0 \end{pmatrix} \qquad \sigma_y = \begin{pmatrix} 0 & -i \\ i & 0 \end{pmatrix} \qquad \sigma_z = \begin{pmatrix} 1 & 0 \\ 0 & -1 \end{pmatrix} \qquad (16)$$

$\mu_{\perp}$ is the projection of the magnetic moment μ_i onto the reflecting plane, and is given by

$$\mu_{\perp\perp} = \mu_i - \mathbf{H}\left(\frac{\mu_i . \mathbf{H}}{|\mathbf{H}|^2}\right) \qquad (17)$$

2.3 Helical antiferromagnets and hexagonal close packed structures.

The three helical antiferromagnets studied in this research can be divided into two, the heavy rare earths which crystallise in a hexagonal close packed (HCP) structure (holmium and terbium) and manganese phosphide which has an orthorhombic structure. This discussion will initially consider diffraction from a HCP structure, under the assumption that the magnetic structure is that of a non-distorted helix. Although this is a considerable simplification of some of the actual magnetic structures (eg. holmium), it is particularly relevant as all the recorded and imaged magnetic data in this thesis were collected solely on first order magnetic satellites.

Working within this regime the magnetic moment at a given atomic site is described by

$$\mu_{id} = \mu \begin{pmatrix} \cos(\tau . \mathbf{R}_{id}) \\ \sin(\tau . \mathbf{R}_{id}) \\ 0 \end{pmatrix} \qquad (18)$$

where, $\mu = g_i \mu_B J$ is the magnetic moment of the ith atom, J being the atoms kinetic moment, and g_i the Landé factor. The propagation vector of the helix (τ) can be written:

$$\tau = \tau c^* = 2\pi \tau \left(\frac{c}{|c|^2} \right) \qquad (19)$$

R_{ld} is the vector position of the atom at the site ld, where (l) gives the position within the hexagonal lattice and (d) defines the position within the unit cell as described below

$$R_{ld} = \left(m + \frac{1}{3}d\right) a + \left(n + \frac{2}{3}d\right) b + \left(p + \frac{1}{2}d\right) c \qquad (20)$$

where m, n and p can take all integer values and d is limited to either 0 or 1. The three vectors a, b, c are defined as illustrated in Fig. 2.4.

By substituting equation (18) into equation (17) the component of the magnetic moment in the reflecting plane, for an ion positioned at a site R_{ld} can be written as

$$\mu_{ld\perp} = \mu \begin{pmatrix} \cos(\tau.R_{ld}) - [H_x \cos(\tau.R_{ld}) + H_y \sin(\tau.R_{ld})] \dfrac{H_x}{|H|^2} \\ \sin(\tau.R_{ld}) - [H_x \cos(\tau.R_{ld}) + H_y \sin(\tau.R_{ld})] \dfrac{H_y}{|H|^2} \\ 0 \quad - [H_x \cos(\tau.R_{ld}) + H_y \sin(\tau.R_{ld})] \dfrac{H_z}{|H|^2} \end{pmatrix} \qquad (21)$$

It is possible to write the sine and cosine functions as an exponential function, and hence a volume related structure factor can be defined from equation (14) as,

$$F(H) = \alpha \Sigma_{ld} \left(A \exp i(H+\tau).R_{ld} + B \exp i(H-\tau).R_{ld} \right) \qquad (22)$$

where $\alpha = 1/2\ f(H)\ \mu_N \cdot \mu$. The indices l and d signify that the summation is taken over both the lattice sites (l) and the atomic positions (d), within each unit cell. In the above expression A and B are independent of R_{ld} and can be expressed as :

$$A = \left(1 - \frac{H_x H_-}{H^2}\right)\sigma_x - \left(i + \frac{H_y H_-}{H^2}\right)\sigma_y - \frac{H_z H_-}{H^2}\sigma_z$$

$$B = \left(1 - \frac{H_x H_+}{H^2}\right)\sigma_x + \left(i - \frac{H_y H_+}{H^2}\right)\sigma_y - \frac{H_z H_+}{H^2}\sigma_z \qquad (23)$$

with $H_+ = H_x + iH_y$ and $H_- = H_x - iH_y$.

By taking into account the definition of R_M given in equation (20) the expression for the structure factor given in equation (22) can be simplified by carrying out the summation over the positions in the unit cell (d) to give,

$$F(H) = \alpha\left(A\left(1 + \exp i(H + \tau).\zeta\right)\Sigma_i \exp i(H + \tau).R_i + B\left(1 + \exp i(H - \tau).\zeta\right)\Sigma_i \exp i(H - \tau).R_i\right) \qquad (24)$$

The summation is now only taken over the hexagonal lattice sites and the expression ζ simply describes the unit cell as seen below,

$$\zeta = \frac{1}{3}a + \frac{2}{3}b + \frac{1}{2}c \qquad (25)$$

For F(H) to be non zero, the diffraction vector (H) should be such that $H = h + \tau$, where h is a hexagonal reciprocal lattice vector.

From this result it is clear that magnetic and nuclear diffraction do not correspond to the same diffraction vectors. Moreover it can be seen that each nuclear peak (which corresponds to a reciprocal lattice vector) is centered between two purely magnetic satellite reflections, which are displaced by $+\tau$ and $-\tau$ one side and the other. The absent positions in the diffraction spectrum (which occur when F(H) = 0) correspond to the forbidden Bragg reflections of the hexagonal close packed lattice. The condition for an absent position being satisfied when,

$h.\zeta = (2k + 1)\pi$ where k takes integer values

with solutions occuring when $h_3 = 2n$ and $h_1 - h_2 \neq 3n$, , where h_1, h_2 and h_3 are components of the reciprocal lattice vector **h**, which is written as

$$\mathbf{h} = h_1 \mathbf{a}^* + h_2 \mathbf{b}^* + h_3 \mathbf{c}^* \qquad (26)$$

2.3a The 0002±τ reflection

In both of the hexagonal close packed systems studied the reflection of major interest has been the 0002±τ where the reciprocal lattice vector (**h**) is parallel to propagation vector of the helix (τ). In this configuration it is possible to have a zero valued structure factor on one magnetic satellite when the neutron polarization vector (**p**) is also parallel to **h** and τ, and a zero valued structure factor on the opposite satellite when **p** is antiparallel to **h** and τ.

In this particular case the equations given in (23) can be simplified to the following notation,

$$\left.\begin{aligned} A &= \sigma_x - i\sigma_y \\ B &= \sigma_x + i\sigma_y \end{aligned}\right\} \qquad (27)$$

By substituting these values into the following expression

$$F_\pm = F(0002 \pm \tau) \qquad \text{at} \quad \alpha_\pm = \frac{1}{2} f(0002 \pm \tau)\ \mu_N.\mu \qquad (28)$$

the volume related structure factor of each domain type can be written as,

$$F_+ = N\alpha_+ (\sigma_x + i\sigma_y) = \beta_+ \begin{pmatrix} 0 & 1 \\ 0 & 0 \end{pmatrix} \quad \text{where } \beta_+ = 2N\alpha_+ \qquad (29)$$

and

$$F_- = \beta_- \begin{pmatrix} 0 & 0 \\ 1 & 0 \end{pmatrix} \qquad (30)$$

If the neutron beam is polarized in the horizontal plane then there are two possible eigenstates which can describe the neutron spin. These can be written as:

$$|+\rangle = \begin{pmatrix} 1 \\ 0 \end{pmatrix} \text{ and } |-\rangle = \begin{pmatrix} 0 \\ 1 \end{pmatrix} \tag{31}$$

Simple matrix algebra yields that

$$\left.\begin{aligned} F_+ |+\rangle &= |0\rangle \\ F_- |+\rangle &= \beta_- |-\rangle \\ F_+ |-\rangle &= \beta_+ |+\rangle \\ F_- |-\rangle &= |0\rangle \end{aligned}\right\} \tag{32}$$

where $|0\rangle$ represents $\begin{pmatrix} 0 \\ 0 \end{pmatrix}$. From the above result it is clear that each satellite reflection only diffracts a specific neutron polarisation state and this is reversed when diffracting from the adjacent satellite. These results have been previously shown in another way in the publications of Izyumov (1962), Blume (1963) and Sivardiere (1967).

The description of the distribution of magnetic moments given in equation (18) only allows the description of the chirality of an isolated single domain crystal. Experimental evidence has shown that helimagnetic crystals are divided into a domain structure, which isolate regions of opposite chirality as described by the propagation vectors $+\tau$ and $-\tau$. These two domain types exhibit different structure factors.

Type I domains (characterised by a positive propagation vector ($+\tau$)), can be described as follows :

$$\begin{aligned} F_{I+} &= 2N_I \alpha_+ \begin{pmatrix} 0 & 1 \\ 0 & 0 \end{pmatrix} = \beta_{I+} \begin{pmatrix} 0 & 1 \\ 0 & 0 \end{pmatrix} \\ F_{I-} &= 2N_I \alpha_- \begin{pmatrix} 0 & 0 \\ 1 & 0 \end{pmatrix} = \beta_{I-} \begin{pmatrix} 0 & 0 \\ 1 & 0 \end{pmatrix} \end{aligned} \tag{33}$$

where N_I is the number of atoms in the domains of type I.

For domains of type II (characterised by a negative propagation vector ($-\tau$)), $F_{II}(H)$ can be obtained by inverting A and B in equation (24), which gives

$$F_{II+} = 2N_{II}\,\alpha_{+}\begin{pmatrix} 0 & 0 \\ 1 & 0 \end{pmatrix} = \beta_{II+}\begin{pmatrix} 0 & 0 \\ 1 & 0 \end{pmatrix}$$

$$F_{II-} = 2N_{II}\,\alpha_{-}\begin{pmatrix} 0 & 1 \\ 0 & 0 \end{pmatrix} = \beta_{II-}\begin{pmatrix} 0 & 1 \\ 0 & 0 \end{pmatrix} \qquad (34)$$

For a given polarisation, the overall structure factor for a multi-domain sample will given by summing the structure factors for the two types of domains as seen below

$$F_{+} = F_{I+} + F_{II+} = \beta_{I+}\begin{pmatrix} 0 & 1 \\ 0 & 0 \end{pmatrix} + \beta_{II+}\begin{pmatrix} 0 & 0 \\ 1 & 0 \end{pmatrix}$$

$$F_{-} = F_{I-} + F_{II-} = \beta_{I-}\begin{pmatrix} 0 & 0 \\ 1 & 0 \end{pmatrix} + \beta_{II-}\begin{pmatrix} 0 & 1 \\ 0 & 0 \end{pmatrix} \qquad (35)$$

In this case neither F_{+} nor F_{-} will be zero valued in a normal case. Bearing in mind that the two types of chirality domain usually occupy equal volumes of the sample (Baruchel et al 1990), even when using polarised neutron diffraction it is difficult to distinguish a difference in the diffraction from F_{+} and F_{-}, although a slight difference was observed by Felcher et al (1971).

However, by detecting the diffracted intensity from a single crystal sample (placed in an incident polarised neutron beam in the Bragg position for a magnetic satellite reflection), on a photographic film it is possible to obtain a direct image of the diffracting domain type. This technique is an example of polarised neutron diffraction topography, and will be explained in more detail in the experimental techniques of chapter three.

2.4 The adaptation to other samples.

As stated in chapter one, the magnetic structure of manganese phosphide takes the form of a double helix in the antiferromagnetic phase. The double helix structure modifies the above described behaviour as the domains characterised by a positive propagation vector will have a larger intrinsic structure factor than those of negative τ. This is evident in the neutron diffraction data of MnP (presented in chapters 4, 5 and 7),

where all the neutron topographs were taken on the $+\tau$ satellites in order to have the maximum intensity possible.

The single helical structures of terbium and holmium do not show this effect and it is the negative τ satellite which has the larger intensity. In this case the difference in the intensity of the two satellites results from the relative sizes of their Bragg angles. Secondly, the difference in crystal structure (orthorhombic for manganese phosphide), should be taken into account when defining the absent positions of the system.

The magnetic structure of chromium-silicon can be described in a similar way to that of a helix, but with the difference that the magnitude of the magnetic moment will be modulated along a single axis. This is represented by adapting equation (18) to the following value

$$\mu_{ld} = \mu \begin{pmatrix} \cos(\tau . R_{ld}) \\ 0 \\ 0 \end{pmatrix} \qquad (36)$$

Transverse and longitudinal spin density waves are described by the relative orientation of the propagation vector of the system to the plane of the magnetic moment. Just as in the previously described cases the sample will be subdivided into a domain structure in the ordered magnetic phase. As the propagation vector lies along the cube edges of this body centered cubic system, it is possible to have a multiple domain structure existing in the ordered phase. The classification of these domain structures has already been discussed in chapter one under a similar nomenclature as described by Ando and Hosoya (1978). As for manganese phosphide the change in crystal structure (body centered cubic for chromium - 0.6 at. % silicon) should also be taken into account in the above structure factor calculations.

2.5 Kinematical Theory.

Having derived an expression for the structure factor of a given reflection from the crystalline structure and magnetic moment distribution of the sample, it is possible to calculate the amplitude of the reflection and its position can be predicted from Bragg's law as described in equation (12). However, most diffraction experiments require a predicted value of the intensity of the diffraction peaks and this cannot be derived from these expressions, but should be calculated from the complete scattering cross-section. By following the method of Squires (1978) this is achieved by integrating the differential cross-section with respect to the solid angle (Ω) as shown below

$$\mathcal{R}_{KIN} = \int (2\Pi)^3 \frac{N}{V_c} \Sigma_\tau |F(H)|^2 \delta(H-\tau)\, d\Omega \qquad (37)$$

However, the detected integrated intensity of the diffracted beam from a typical diffraction experiment does not give a direct measurement of the total cross-section. The reason for this disparity is that the delta function contained in the above theoretical expression is not normally realised experimentally, as the diffraction peaks have a finite width due to the sample mosaic spread and the instrumental resolution. The general solution to the problem caused by this angular broadening, is to allow the detection collimation to be sufficiently relaxed so that all the scattered neutrons can be detected.

The most common method for measuring the integrated intensity involves rotating the sample in an incident neutron beam and detecting the diffracted neutrons in an open, fixed position counter which is placed at twice the calculated Bragg angle from the incident monochromatic beam. The wide acceptance of the open detector allows the detection of all the neutrons which are diffracted by the sample. This type of scan is termed an omega scan. It allows the mosaic spread of the sample to be derived from the full width half maximum (FWHM) of the rocking curve.

A second method for measuring the integrated intensity involves rotating the detector through the diffraction condition at twice the angular velocity of the sample. This scan is termed an omega-two theta scan. It should be noted here that collimating the detector will restrict the detected integrated intensity to a local region of the sample (of a given misorientation) and the FWHM of the rocking curve will only represent the mosaic spread of a specific region of the sample and not the whole of it. If the detector is not collimated this scan reduces to the previous one.

The omega and omega-two theta scans are analogous to the integration over all omega values in the theoretical expression of equation (37). The integrated intensity is given by the following equation :

$$I = \phi \int_{0}^{\pi} \mathcal{R}_{KIN}\, d\psi \tag{38}$$

where ϕ is the incident neutron flux and $d\psi$ is the change in angular position of the sample. On integrating and taking into account the crystal volume ($V = N v_c$) the integrated intensity can be written as follows;

$$I = \phi V Q \tag{39}$$

where the kinematic reflecting power is given by

$$Q = \lambda^3 \frac{|F(H)|^2}{V_c^2 \sin 2\theta} \tag{40}$$

The kinematical reflectivity per unit beam area is plotted in Figure 2.8 as a function of crystal thickness, where the linear relationship is described by the following expression;

$$\mathcal{R}_{KIN} = Q.t \tag{41}$$

where t is the neutron path length within the sample. The main assumption made in this derivation is that each unit cell within the sample receives an equal amount of incident neutron flux. These constraints provide a basic description of an "ideally imperfect crystal", where the individual intensities from different parts of the sample can be summed to give the total diffracted intensity of the sample. Diffraction from such a sample will yield the maximum possible value for the integrated intensity of a reflection, but clearly most crystalline samples do not behave in an ideal manner. Moreover, as crystal quality improves large deviations from the predicted integrated intensity of equation (38) can be seen from the experimental data.

2.6 Dynamical Theory.

The other limiting value to crystal behaviour is that of a "perfect crystal", which is said to consist of a perfectly periodic arrangement of unit cells. The propagation of a neutron through such a medium is described by the dynamical theory of diffraction in which the diffracted wave is coupled through the crystalline lattice to a refracted wave, and these two waves are then coherent. Acknowledging the existence of a refracted wave implies a neutron refractive index (n). This is in fact the case and a derivation of its value can be found in Squires (1978). For our particular purposes it is sufficient to state that the refractive index is dependent on incident wavelength, the number of nuclei per unit volume and the mean scattering length of the nuclei. It is not dependent on crystal structure. A typical value of n is given from

$$1 - n \simeq 10^{-5}$$

which although small, is enough to permit both refraction and total reflection events to occur at sample boundaries.

Hence each single wave vector radius (as previously described in Figure 2.3), must now be represented as two spheres, one for the waves in vacuo and the other for

Figure 2.5. A reciprocal space representation of the condition for Bragg diffraction from a crystalline lattice.

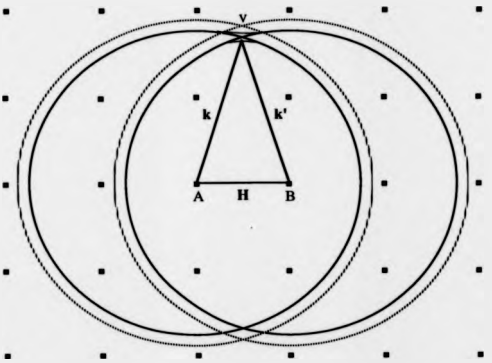

Figure 2.6. An enlargement of the dispersion surface for the specific case of a sample in the Laue geometry

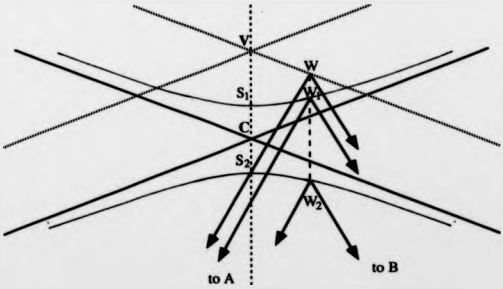

waves in the crystal (Figure 2.5). The dynamical theory describes the convergence of these two wave vectors by solutions of the Schrödinger equation for a neutron beam incident on a perfectly periodic crystalline lattice. The periodicity of the lattice is introduced as a periodic potential and the predicted wave vector solution of the original geometrical condition for Bragg diffraction (which corresponds to the intersection of the two spheres centered at A and B in figure 2.3), can be represented as a two wave solution as described by Schlenker (1991).

These two waves propagate from every point on the double branched hyperbola (as seen on the enlargement of the intersection region in Figure 2.6.), whose asymptotes correspond to the wave vector spheres of figure 2.5 (now represented as straight lines). This two branched hyperbola is called the dispersion surface and contains information about which waves will propagate in the crystal. It should be noted that the size of the dispersion surface has been grossly exaggerated as the change in wave vector is typically only one part in 10^5. The actual corresponding real space length of the diameter of the hyperbola (S_1S_2) can be represented by,

$$\frac{1}{S_1S_2} = \frac{\pi V_c \cos\theta}{\lambda |F[H]} = \Lambda \cos\theta \qquad (42)$$

where Λ is the extinction length of the sample. This quantity is particularly useful for defining extinction types when dealing with integrated diffracted intensities which are less than the values predicted by the dynamical theory as will be seen in section seven of this chapter.

An incident wave (represented by W on the vacuum sphere of figure 2.6) will create two waves at the intersection of the normal to the entrance surface and the two branches of the dispersion surface (W_1 and W_2). Consequently it is important to take into account the specific diffraction geometry of the sample, which in this case is that of the symmetrical Laue geometry.

2.6a The Laue or transmission geometry.

This geometry is defined so that the inward normal to the crystal surface lies between the incident and reflected beams. The incident plane wave in figure 2.6 produces two waves as characterised by the wavevectors W_1A and W_2A, which then define the diffracted wave. As in the kinematical approximation it is important to appreciate exactly what quantities are being physically measured when performing diffraction experiments in the dynamical limit. Once again it is the integrated reflectivity (ie. the area under the rocking curve) which is measured in these investigations. The "intrinsic" rocking curve (for an incident plane wave), produced by samples in the Laue orientation can be seen in figure 2.7.

In the Laue geometry the reflected beam passes through the sample mass and thus the angular reflectivity will be dependent on the crystal thickness. This dependence is illustrated for an incident spherical wave in figure 2.8 where the total reflectivity is plotted by integrating over the crystal rotation angle as a function of the crystal thickness. The expression which describes the total reflectivity takes the following form,

$$\mathcal{R} = \left\{ \left| \frac{\lambda^2 F(H)}{\pi V_c} \right| . \frac{1}{\sin 2\theta} \right\} W(A) \qquad (43)$$

where W(A) is the Waller integral defined as

$$W(A) = \frac{\pi}{2} \int_0^{2A} J_o(u)\, du \qquad (44).$$

$J_o(u)$ is a Bessel function of rank 0, and A is the reduced crystal thickness as defined by $(\pi t_0 / \Lambda)$. The limiting value of W(A) for large A is given as $\pi/2$, and as such the oscillating W(A) function will converge to a limiting reflectivity value. This limiting value which is defined for a non absorbing crystal can be described by the following expression,

Figure 2.7. The rocking curve for a perfectly flat crystal in the Laue orientation for a incident plane wave.

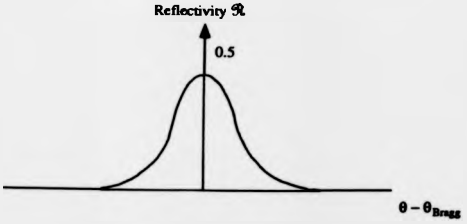

Figure 2.8. The reflectivity plotted as a function of a reduced crystal thickness for an incident spherical wave.

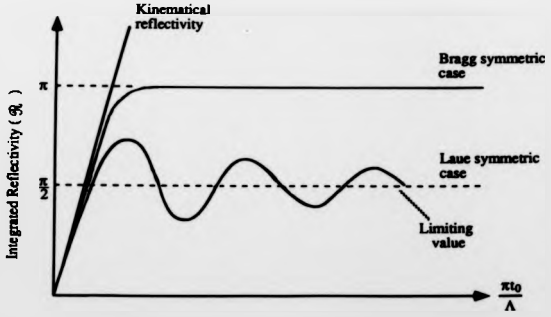

$$\mathcal{R}_{Lim} = \frac{\lambda^2 F(H)}{2 V_c \sin 2\theta} \qquad (45)$$

2.6b The Bragg or reflection geometry.

The Bragg geometry, which is defined such that the outward normal to the crystal surface lies between the incident and diffracted beams is illustrated in the reciprocal space representation of figure 2.9. An interesting situation arises when the incident beam is located at W on the spherical wavevector surface, as the normal to the crystal surface does not intercept the two branches of the dispersion surface. In this case the incident wave will be totally reflected. The angular range over which a sample will exhibit total reflection is simply described by the range of incident wavevectors which lie on the sphere from R_1 to R_2 and is given by the expression,

$$\varepsilon = \frac{2 \lambda^2 |F(H)|}{\pi V_c \sin 2\theta} \qquad (46)$$

where ε is termed the Darwin width. A typical rocking curve (for an incident plane wave), produced from a sample which is in symmetrical Bragg geometry is shown in figure 2.10. The flat top of this rocking curve represents the angular region in which the sample undergoes total reflection. The Darwin width corresponds to $2/\pi$ of the FWHM of this curve.

The reflectivity decreases steadily with increasing deviation from the Bragg angle on either side of the Darwin width. Clearly the width at the base of the rocking curve is greater than the Darwin width and hence in the limit of an infinitely thick, non absorbing crystal in symmetrical geometry the reflectivity has a limiting value which is described by,

$$\mathcal{R} = \pi \cdot \frac{\varepsilon}{2} = \frac{\lambda^2 |F(H)|}{V_c \sin 2\theta} \qquad (47)$$

Figure 2.9. An enlargement of the dispersion surface for the specific case of a sample in Bragg symmetrical geometry

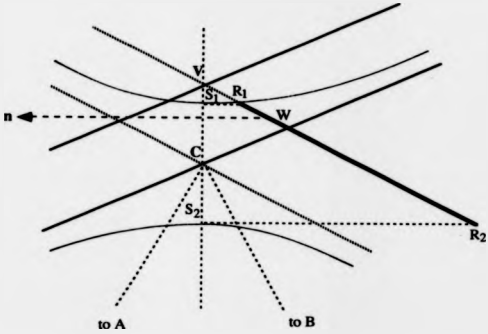

Figure 2.10. The rocking curve for a crystal in the Bragg geometry.

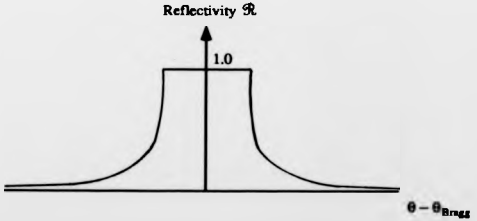

which is exactly twice the value of the reflectivity predicted by the Laue geometry. When dealing with real crystals of finite thickness, the reflectivity can be expressed as a function of thickness as described below and illustrated in Fig. 2.8.

$$\mathcal{R} = \frac{\lambda^2 |F(H)|}{V_c \sin 2\theta} \tanh A \qquad \text{where } A = \frac{\pi t_0}{\Lambda} \tag{48}$$

where Λ is the extinction length which is again defined from the diameter (S_1S_2) of the dispersion surface, but because of the change in geometry of the incident wave it takes the form of,

$$\Lambda \sin\theta = \frac{1}{S_1S_2} = \frac{\pi V_c \sin\theta}{\lambda |F(H)|} \tag{49}$$

At very low values of A (when $t < \Lambda$), the dynamical expressions for the Laue and Bragg integrated reflectivities in the dynamical theory have approximately the same value. Moreover, as this value approaches zero the tangent of these two curves describes the kinematical reflectivity as a function of the reduced crystal thickness (A).

It should be noted that in the dynamical limit the reflectivity ($\mathcal{R}$) is proportional to the magnitude of the structure factor (F(H)) and not to its square as in the case of the Kinematical theory. Also for neutron path lengths in the sample (t), greater than the extinction length (Λ) the reflectivity will be nearly constant which is not the case in the kinematical theory (figure 2.8)

2.7 Extinction.

In diffraction experiments involving real crystals the measured integrated intensity falls between the two limiting values; the maximum possible intensity being that predicted for an ideally imperfect crystal as described by the kinematical theory and the minimum being that of a perfect crystal as described by dynamical theory. The ratio of the

measured integrated intensity to that predicted by kinematic theory is termed the extinction coefficient (y).

The treatment of crystals which have diffracted intensities less than those predicted by the kinematical theory were initially classified into primary and secondary extinction models. Throughout this discussion primary extinction will be described with reference to a single diffraction event occurring within a sample which has been irradiated by a neutron beam. The intensity diffracted by such a system will be coherent and as such is well adapted to a dynamical treatment. The above tentative definition of primary extinction (as illustrated in Figure 2.11) allows the diffracted intensities of both thin, poor quality crystals, or thicker, better quality samples to be described by primary extinction. A more quantitive description of this condition can be made by considering a characteristic size parameter of the diffracting regions (for example the mosaic block size R as used in the mosaic model). When this mosaic block size is of the same order or bigger than the extinction length (as described in equation (42) for the Laue geometry), then the sample is said to undergo primary extinction.

The condition for the scattering of the same beam by different regions within the crystal is illustrated in Figure 2.12. It is clear that the intensity of a beam incident on a correctly oriented block at B will be depleted with respect to that incident at A. The reduced incident intensity at the entrance face of block B does not allow the block to diffract the intensity predicted from its associated kinematical reflecting power. Hence the diffracted intensities of such a system will be diminished from those predicted for an ideally imperfect crystal in the kinematical theory. This reduction in the diffracted intensity is described by secondary extinction effects.

In the primary and secondary extinction models described in this work the absorption coefficient of the sample is assumed to be small as is concurrent with the holmium and manganese phosphide samples which have been treated.

Figure 2.11. A single diffraction event ocurring in a crystalline sample.

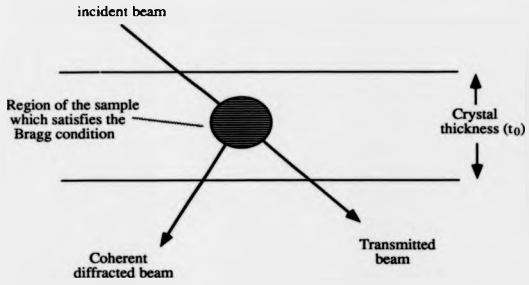

Figure 2.12. A series of diffraction events ocurring in a crystalline sample.

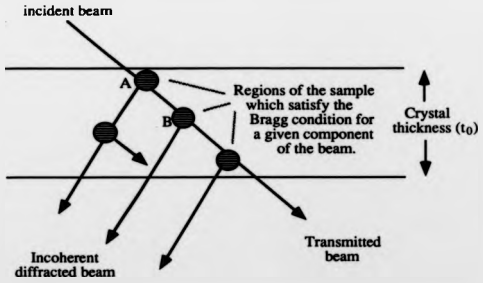

2.7a Secondary extinction.

Historically extinction effects have been described by a mosaic model, where the sample is said to be composed of a distribution of small perfect crystalline blocks of characteristic dimension R, with an average angular misorientation (η), from the mean orientation of blocks within the sample.

Working within these constraints a variety of extinction treatments have been produced (Bacon & Lowde 1948, Zachariasen 1967, 1968, Becker & Coppens 1974, and Sabine 1990). In each of the above mentioned cases the starting point has been the Energy Transfer Equations (ETE) as described by Darwin (1922) and Hamilton (1957), and illustrated below.

$$\begin{aligned} \frac{\partial P_i}{\partial t_i} &= \tau P_i + \sigma P_d \\ \frac{\partial P_d}{\partial t_d} &= \sigma P_i + \tau P_d \end{aligned} \qquad (50)$$

where P_i and P_d are the current densities at a position in the crystal (t_i, t_d). The distance t_i is measured along the incident beam direction and t_d along the diffracted beam direction. τ is the removal cross-section per unit volume and includes all processes which remove energy from the incident beam, as such it always has a negative value. σ is the cross-section per unit volume for Bragg scattering at an angle 2θ between t_i and t_d.

Zachariasen assumed that the only removal process was that of Bragg scattering ($\tau = -\sigma$, zero absorption) and by using a Gaussian functional form for the coupling coefficient σ, derived the following expression for the secondary extinction coefficient

$$y_s = (1 + 2x)^{-\frac{1}{2}} \qquad (51)$$

where x is given by

$$x = \frac{R Q t}{\lambda} \left\{ 1 + \left(\frac{3 \eta R}{\lambda} \right)^2 \right\}^{-\frac{1}{2}} \qquad (52)$$

From this expression it is possible to define two types of behaviour, these depending on the relative magnitudes of the mosaic block size (R) and the average angular misorientation (η) as shown below,

$$\eta >> \lambda/R \qquad \text{Type I}$$

$$\eta << \lambda/R \qquad \text{Type II} \tag{53}$$

The type I system is dependent on the misorientation between blocks, whilst in type II the dominant term is the mosaic block size.

Becker & Coppens (1974) expressed the ETE's in integral form and solved them using numerical methods for a spherical mosaic crystal using Gaussian, Lorentzian and Fresnellian coupling coefficients. The analysis of these calculations indicated that the formulae of Zachariasen (equations 51 & 52) were only valid for a small amount of extinction ($y > 0.8$). The most consistent solutions to the equations of of Becker & Coppens were achieved when using a Lorentzian functional form for the coupling coefficient. These solutions lead to the suggested modification of Zachariasen's value of y_s, where the average mosaic block size (R) should be represented as $R\sin 2\theta$ in order to take into account the actual neutron path length. This factor has the effect of reducing the validity of the previous sample classifications given at (53), as at small angles nearly all samples are described in the type II regime.

Sabine's treatment of the secondary extinction regime (1990) deals with solutions to the ETE's for a selection of functional forms for the coupling coefficient (σ). By substituting a Lorentzian functional form for the coupling coefficient of the ETE's different expansions are derived for the extinction coefficient when the sample is either wholly in the Laue or the Bragg geometry. In the case of Laue geometry the extinction coefficient takes the form of the following two expansions

$$y_{Laue} = 1 - \frac{x}{2} + \frac{x^2}{4} - \frac{5x^3}{48} + \frac{x^4}{192} \ldots \qquad \text{when } x \leq 1 \tag{54}$$

and

$$y_{Laue} = \left(\frac{2}{\pi x}\right)^{\frac{1}{2}} \cdot \left[1 - \frac{1}{8x} - \frac{3}{128x^3} - \frac{15}{1024x^4}\right] \qquad \text{when } x > 1 \tag{55}$$

where x is given by the following expression for the case of non absorbing crystals,

$$x = \left(\frac{F\lambda R}{V_c} + \frac{F^2\lambda^3 g(t_0 - R)}{V_c^2 \sin 2\theta}\right)^2 \tag{56}$$

t_0 represents the sample thickness and g the average mosaic misorientaton parameter where $g = (3\eta)^{-1}$. In the Bragg case only one expansion was derived and this is given as,

$$y_{Bragg} = \left(\frac{1}{1+x}\right)^{\frac{1}{2}} \qquad \text{for all values of x.} \tag{57}$$

The angular variation of the extinction coefficient is represented by the angular coupling of the extinction parameters for the Laue and Bragg geometries as shown below,

$$y_{(2\theta)} \approx y_{LAUE} \cos^2\theta + y_{BRAGG} \sin^2\theta \tag{58}$$

Whilst this may be a valid assumption in the case of a spherical crystal, it is not so practical when considering flat platelet samples as have been used in this investigation. Moreover, in the case of holmium where the platelet sample was in Laue geometry then only equations (54) and (55) were considered and the effects of the Bragg geometry were ignored. Care must be taken when passing from one regime to the other in the Laue geometrical case, as the two series expansions are not continuous at the cross-over point, when x=1.

The major deficiency of the mosaic theory is its failure to adequately describe primary extinction. This arises because no practical solutions have been produced for a finite block size (ie where R ≈ A) in the dynamical theory, as a result of the complexity of

the mosaic block boundary conditions. Whilst this was avoided to some degree by a first order approximation of Becker & Coppens (1974) when solving the energy transfer equations for single blocks, this is still not a satisfactory solution, as no analogous physical situation exists.

2.7b Primary Extinction.

As was hinted in the previous section, solutions of the ETE equations produce an acceptable treatment of secondary extinction effects, but this method is of no use for describing single, isolated regions which diffract coherently and whose intensities can be described through primary extinction. In this investigation such systems have been interpreted through the random elastic deformation model (RED) as developed by Kulda in the following series of publications (Kulda 1984, 1987, 1988, 1991).

The general structure of this model can be described by a sample which is divided into an arrangement of spherical domains (of diameter d), which are distorted from a perfect crystalline structure by an elastic deformation. This deformation is assumed to be random in both magnitude and direction on traversing domains. The misorientation from the Bragg condition is assumed continuous across the domain boundaries, thus allowing the description of primary extinction without the obligatory assumption of the sample being a single domain as in the treatment of Becker & Coppens (1974).

The elastic deformation is one of the free parameters of the RED model and it takes the form of a uniform bending of constant radius (R). This bending radius is analogous to the angular misorientation from an arbitrary mean value ($\Delta\omega$) in the mosaic model. The second free parameter $\bar{t}$, is the mean free path between subsequent reflections and this is used to describe the probability of an incident neutron beam undergoing multiple scattering within the sample. When $\bar{t}$ is less than neutron path length in the crystal (T) the ETE's can be solved using the RED model to describe the diffracted

intensity through secondary extinction. However for primary extinction we will be limited to the case where $\bar{t} >> T$.

In this general case the reflecting power of the crystal can be described by two continuous distributions $\omega_1(t_0)$ and $\omega_2(R)$, where t_0 is the crystal thickness and R the bending radius. However, in the specific case of the holmium sample which was investigated here, the sample thickness was approximately constant so the integrated reflecting power of the sample could be reduced to the following single integral expression, which assumes a fixed average crystal thickness (t).

$$\overline{\mathcal{R}} = \int \mathcal{R}(t,R)\,\omega_2(R)\,dR \qquad (59)$$

The function $\omega_2(R)$ is assumed to be an asymmetric γ function as it is clear from experimental evidence that highly distorted regions can be responsible for producing the majority of a crystals diffracted intensity when they are surrounded by nearly perfect regions as found in high crystalline quality samples. Kulda (1990) represented this function in the following form,

$$\omega_2(\eta) = \frac{\eta^{\alpha} \exp -(\eta)}{\Gamma(\alpha+1)} \qquad (60)$$

where $\eta = (\alpha+1)R / \bar{R}$, with $\bar{R}$ being the mean effective bending radius and α is a parameter related to the angular width of the mosaic regions. Figure 2.13 shows a plot of the γ function as a function of α, where with a small distribution of bending radii (large α) the γ function can be approximated to a Gaussian form, whilst at small α the function takes the form of an exponential thus allowing for the small highly distorted regions which diffract a large intensity.

By substituting equation (60) into (59) and solving, Kulda has shown that the integrated reflectivity can be represented by the following expression,

Figure 2.13: The assymetric γ distribution as a function of the magnitude of the effective bending radius for a series of increasing values of the α parameter as produced by Kulda (1991).

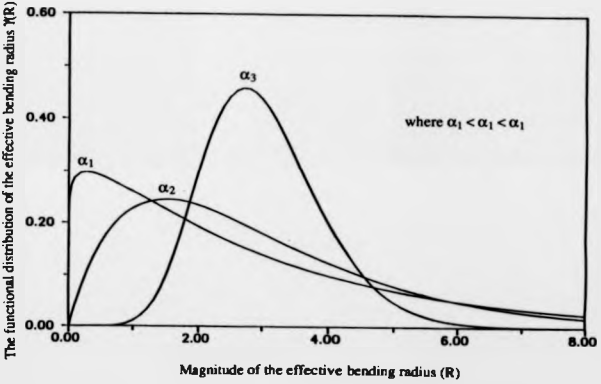

$$\overline{\mathcal{R}_{RED}} = \frac{T}{\overline{R}}\, C(c,\theta)\, \frac{\alpha+1}{\alpha} \left(1 - \frac{1}{\left(1 + \frac{Q_{KIN}\,\overline{R}}{C(c,\theta)}\, \frac{1}{\alpha+1} \right)^{\alpha}} \right) \qquad (61)$$

The variable function C(c,θ) defined as,

$$C(c,\theta) = \frac{\left[c + (1-2c)\cos^2\theta \right]}{\cos\theta} \qquad (62)$$

allows for the two particular effects of the elastic deformation on the specific sample regions to be taken into account through the variation of the parameter (c). That is as c tends to one the misorientation can be represented as a lattice spacing gradient and when c tends to zero as the misorientation of lattice planes.

From the relationship for the primary extinction coefficient y_p given below,

$$y_p = \frac{\mathcal{R}_{RED}}{\mathcal{R}_{KIN}} \qquad (63)$$

it immediately follows that the y_p can be expressed in terms of the free parameters of the RED model as,

$$y_p = \frac{C(c,\theta)}{Q_{kin}\,\overline{R}}\, \frac{\alpha+1}{\alpha} \left(1 - \frac{1}{\left(1 + \frac{Q_{KIN}\,\overline{R}}{C(c,\theta)}\, \frac{1}{\alpha+1} \right)^{\alpha}} \right) \qquad (64)$$

where the relative proportions of the sample which exhibit primary and secondary extinction are described by the ratio of the mean free path of the neutrons to their path length in the sample.

2.8 Summary.

The contents of this chapter were almost completely pre-determined by the use of monochromatic, polarised neutrons as a probe of the crystalline and magnetic structure of our samples and the constraints imposed on the sample quality and orientation by the

specific application of neutron diffraction topography. Initially the effect of neutron polarisation and a chirality domain structure on the diffracted neutrons were described through the definition of a magnetic structure factor (F(H)). The deviation of the observed integrated intensity from the $(F(H))^2$ dependence of the kinematical theory and the approach to the F(H) dependence of the dynamical theory was described through extinction theory. The classification of primary and secondary extinction was described with attention being given to the sample orientation (as a result of the platelet sample shape required in neutron topography).

From within this simple framework the neutron diffraction results presented in the following chapters can be clearly understood. Moreover the combination of such results to those of other complementary techniques (synchrotron radiation topography, magnetisation, elastic constant, and compositional analysis measurements) will be seen to be essential in providing a thorough understanding of our samples. All of these techniques will be described in the following chapter.

CHAPTER THREE

EXPERIMENTAL TECHNIQUES.

3.1 Introduction.

Throughout this research the majority of measurements have been carried out at the Institute Laue-Langevin on the special beam instrument S20, a two axis diffractometer situated on the H24 thermal beam line. The instrument has the capability to be used to study neutron diffraction or high resolution neutron diffraction topography.

The basic principles involved in elastic neutron scattering have already been dealt with in the previous chapter, but it is worth emphasing that the technique of neutron diffraction provides an excellent probe for the investigation of solid state materials, due to the weak interaction of the neutron with atomic nuclei (typical neutron absorption cross sections being at least three orders of magnitude smaller than their corresponding x-ray cross-sections). The neutron is especially useful when investigating magnetic systems as its magnetic moment interacts with the systems magnetic arrangement, thus providing information about the materials magnetic structure. However, the technique of neutron diffraction is at best a volume averaged one. That is to say the specific regions of a sample that contribute to diffraction such as domains, defects, phase boundaries, and impurities cannot be observed in isolation. However, with the advent of neutron diffraction topography this is now a possibility. Moreover when observing solely magnetic reflections under polarised neutron conditions it is possible to directly image several exotic domain structures (Baruchel et al. 1990) which cannot be achieved by any other technique.

When monitoring a magnetic phase transition with neutron diffraction it is often possible to observe a variation in detected intensity due to a variation in the magnitude of

CHAPTER THREE

EXPERIMENTAL TECHNIQUES.

3.1 Introduction.

Throughout this research the majority of measurements have been carried out at the Institute Laue-Langevin on the special beam instrument S20, a two axis diffractometer situated on the H24 thermal beam line. The instrument has the capability to be used to study neutron diffraction or high resolution neutron diffraction topography.

The basic principles involved in elastic neutron scattering have already been dealt with in the previous chapter, but it is worth emphasing that the technique of neutron diffraction provides an excellent probe for the investigation of solid state materials, due to the weak interaction of the neutron with atomic nuclei (typical neutron absorption cross sections being at least three orders of magnitude smaller than their corresponding x-ray cross-sections). The neutron is especially useful when investigating magnetic systems as its magnetic moment interacts with the systems magnetic arrangement, thus providing information about the materials magnetic structure. However, the technique of neutron diffraction is at best a volume averaged one. That is to say the specific regions of a sample that contribute to diffraction such as domains, defects, phase boundaries, and impurities cannot be observed in isolation. However, with the advent of neutron diffraction topography this is now a possibility. Moreover when observing solely magnetic reflections under polarised neutron conditions it is possible to directly image several exotic domain structures (Baruchel et al. 1990) which cannot be achieved by any other technique.

When monitoring a magnetic phase transition with neutron diffraction it is often possible to observe a variation in detected intensity due to a variation in the magnitude of

the magnetic moment or its orientation with respect to the scattering plane. Conformation of these results can be obtained by magnetisation measurements in the region of the phase transition. While magnetisation is again volume averaged, it does have the advantage of being much easier to analyse, as there is no need to consider effects like extinction or multiple scattering which could be present in associated neutron single crystal diffraction data. All the magnetisation results presented here were taken at the Laboratoire Louis Néel, CNRS, Grenoble.

Even though synchrotron radiation has a much larger absorption coefficient than that of neutron radiation it does possess two major advantages, namely its intensity and low divergence. This not only dramatically reduces the exposure time required in synchrotron radiation topography (typically 10^3 times shorter than neutron topography), but it also allows the real time imaging of phase coexistence through a scintillator and video camera arrangement. The low divergence results in a resolution limit of approximately 5μm, which is an order of magnitude better than that achieved with neutrons. However, synchrotron radiation topography is limited to systems where the magnetoelastic effects are large enough to produce crystal strains greater than 10^{-6}, as below this the indirect imaging of the phase boundary is not possible. The white beam synchrotron radiation topography data produced in this investigation were accrued on the D25 beam line at the LURE synchrotron radiation facility, Orsay, Paris.

Complementary to the above mentioned direct and indirect observation methods of phase transitions and coexistence is the study of the temperature and field variation of the velocity of ultrasound using the pulse echo overlap technique. The application of an ultrasonic modulation to a magnetically ordered sample has the effect of reducing the anisotropy energy through the magnetoelastic effect. When passing through a magnetic transition the anisotropy is generally at a minimum within the system, and as the moments are relatively free to move, large magnetoelastic effects can be seen. These normally manifest themselves in a softening of appropriate ultrasonic modes leading to a reduction

of the elastic constant and an increase in the ultrasonic attenuation. By propagating ultrasound parallel to a given crystallographic axis and measuring the corresponding ultrasonic velocity and attenuation we have a very sensitive method for the detection of a magnetic phase transition. Once magnetic transitions have been located, the direct techniques of neutron diffraction and topography can be applied, to further characterize these transitions.

The quantitative analysis of backscatted x-ray spectra from a scanning electron microscope is a very effective elemental probe. This technique is confined to the surface region of the sample due to the limited penetration of the x-rays (typically of the order of a few microns). This value is slightly adjustable by varying the incident energy of the x-rays. The technique also has the ability to directly image the elemental composition, but this requires a high quality sub-micron surface finish. The measurements of elastic constant and elemental analysis were carried out in the solid state physics and materials science laboratories at the University of Warwick.

3.2 The S20 diffractometer.

This special beam instrument was originally installed at the Institute Laue-Langevin in 1975, as a simple monochromatic topography station with a crude option for using polarised neutrons. Since then the instrument has been moved up the H24 beam by approximately three metres, thus increasing the intensity by a factor of three, whilst retaining the relatively 'clean' beam conditions characteristic of the end of a long beam guide. The gentle curvature of the beam guide eliminates fast neutrons or gamma rays and the beam profile has a characteristic weak divergence (which can be reduced still further by collimation with a diaphragm at the end of the beam line).

As as result of a series of improvements S20 is now an automated two axis diffractometer and high resolution polarized neutron topography station. A schematic

illustration of the main features of the present instrument are given in Figure 3.1a with the particular adaptations employed in neutron topography being illustrated in Figure 3.1b.

The instrument is such that the incoming white beam is incident on a preselected monochromator producing a diffracted monochromatic beam in accordance with Bragg's law, as previously described in chapter 2. The monochromator carousel allows a choice of four different monochromators giving a wavelength range from 0.9 Å to 2.4 Å. For polarised neutrons the monochromator is a magnetically saturated Heusler Alloy on a 111 reflection. However, in unpolarized work there is a choice between a Cu 220, Cu 111 and silicon 111 monochromators, all of which show different resolution and intensity responses as a function of wavelength. These characteristics will be described in section 3.6 of this chapter.

The resulting monochromatic beam is subjected to two stages of collimation, the first being a fixed circular hole of diameter 3 cm at the exit of the monochromator housing, and the second, a variable slit (normally being critically reduced to the sample size) situated ~10 cm from the sample position. The sample itself is housed in a specially designed tail of a closed cycle helium flow cryostat ("Displex"), which provides a temperature range from 11K to 300K with an accuracy better than ± 0.05K.

The samples studied on S20 are normally mounted on a thin rigid aluminium plate by a small amount of GE varnish at one extremity of the sample. The sample is then surrounded by a cadmium fiducial mark, to aid the aligning and centering of the crystal. A second mounting system allows the possibility of applying a temperature gradient across the sample by clamping the opposite extremity of the sample to a thermally isolated section below the cold head of the cryostat, as illustrated in Figure 3.2. The temperature gradient can be modified by applying a current across the 100 Ohm heating resistance situated below the sample. The warm edge of the sample is clamped between two flush sheets of aluminium. Absolute care must be taken not to apply too much pressure to the sample, and thus introduce strain which could affect the crystalline quality of these near

Figure 3.1a: A schematic plan view of the instrument S20

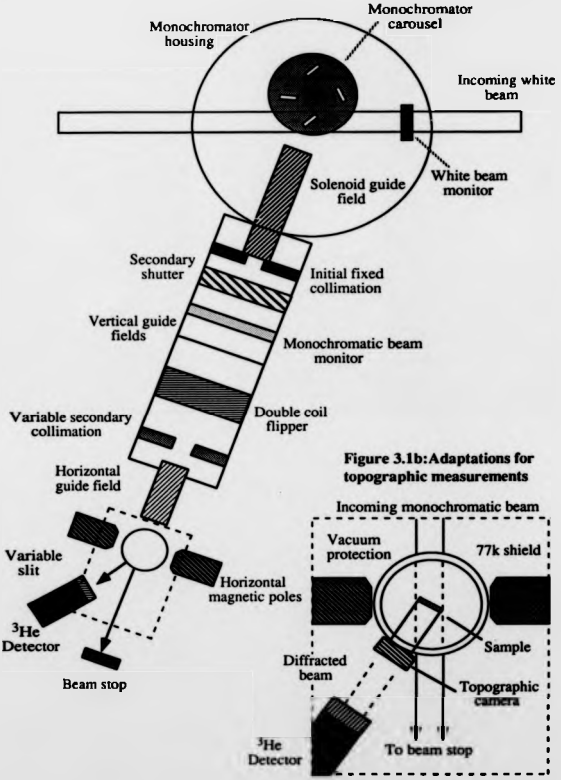

Figure 3.1b: Adaptations for topographic measurements

Figure 3.2: The sample holder for applying a thermal gradient across the sample

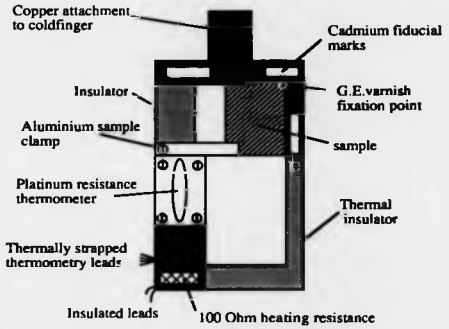

Figure 3.3: A schematic representation of the flux guidance system in the vertical electromagnets

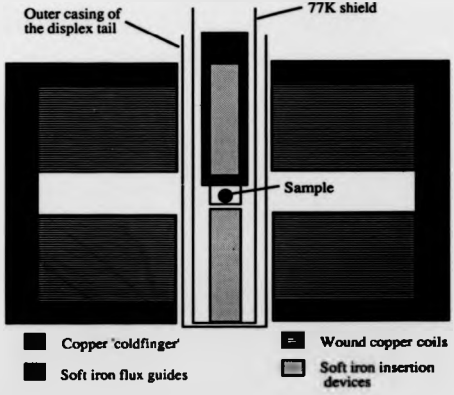

perfect, thin, single crystal plates. In fact this poor thermal contact proved instrumental in producing a stable, reproducible temperature gradient across the sample.

External to the cryostat there is the facility to apply both vertical and horizontal magnetic fields by means of two air cooled electromagnets. In the case of a horizontal field, the geometric restrictions imposed by the need for the highest resolution possible necessitated the development of a series of adjustable polepieces, which allowed variable fields of up to 0.3 Tesla to be applied over several hours. The introduction of magnetic flux guides in the vertical magnet was initially hindered by the solid copper 'cold finger' at the end of the second stage refrigeration device onto which the sample is mounted. This problem was solved by hollowing out the central chamber and inserting a piece of soft iron inside the coldfinger. A second soft iron piece was attached to the base of the 77K shield, thus providing a more effective flux guide in the vertical direction, as illustrated in Figure 3.3. In this configuration a field of ~ 0.2 Teala could be continuously applied.

The diffracted neutron beam is detected by a ^{3}He detector which has an efficiency in excess of 96% over the wavelength range considered in these investigations. The deadtime related to the pre-amplification of the signal from the detection of neutrons is of the order of 1μs.

The instrument is driven by a PDP 11-73 Cubus machine processor through a Camac crate, to give automated omega and theta scans. Whilst the detector was normally used in the plane there was the facility to move off axis by $\pm$ 25 degrees but until now this has remained an uncoded, manual movement, and as such has been seldom used.

3.3 Polarised neutrons.

Neutrons leaving a field saturated Heusler alloy 111 reflection will be polarised in the opposite direction to that of the applied field. It is imperative that this degree of polarisation be retained until the neutrons impinge on the sample. Depolarisation effects are prevented by incorporating a sufficiently large guide field to overcome the parasitic

field effects at the partially iron made monochromator housing. This will then adiabatically rotate the polarisation in accordance with the following inequality as shown by Mezei (1979), and adapted to this particular case by El Kadiri in 1986:

$$\omega_L B > \frac{h}{8 \pi \lambda m D} \qquad (65)$$

where, ω_L is the Larmor Frequency, h is Planck's constant, m the neutron mass, λ the wavelength, and D is the distance required for the field to rotate through 180 degrees. Figure 3.4 shows a schematic illustration of the apparatus used to adjust the direction of the polarisation of the neutrons on S20. The first guide field directs the polarisation along the axis of a solenoid. The polarisation is then rotated into the vertical plane by two permanently magnetised ferrite sheets around which a soft iron circuit has been constructed. In the absence of any current in the flipper coils the polarisation will remain in this direction until it passes into the final rotation field which rotates the polarisation into the horizontal plane. The field at A is roughly 0.01Tesla, which when considering D to be of the order of 10 cm, allows the previous inequality to be satisfied by a factor of around 20. The neutron polarisation is "down" (i.e. antiparallel to the guide field), over the whole path.

In order to change the polarisation of the beam a current is applied to the two flipper coils. The first flipper coil produces a vertical field to nullify the effect of the surrounding guide fields, after which the neutrons magnetic moment is free to precess around the horizontal field produced by the second flipper coil. By placing a second magnetically saturated Heusler alloy (on the 111 reflection) at the sample position these two fields can be critically adjusted to give an optimum flipping ratio. The polarisation is now "up", (i.e. parallel to the guide field). It will be held in the vertical plane until it is rotated, (remaining "up") into the horizontal plane by the horizontal guide field. Thus the neutron polarisation will be almost parallel and anti-parallel to the scattering vector of the

Figure 3.4: A schematic representation of the method of neutron polarisation used on S20.

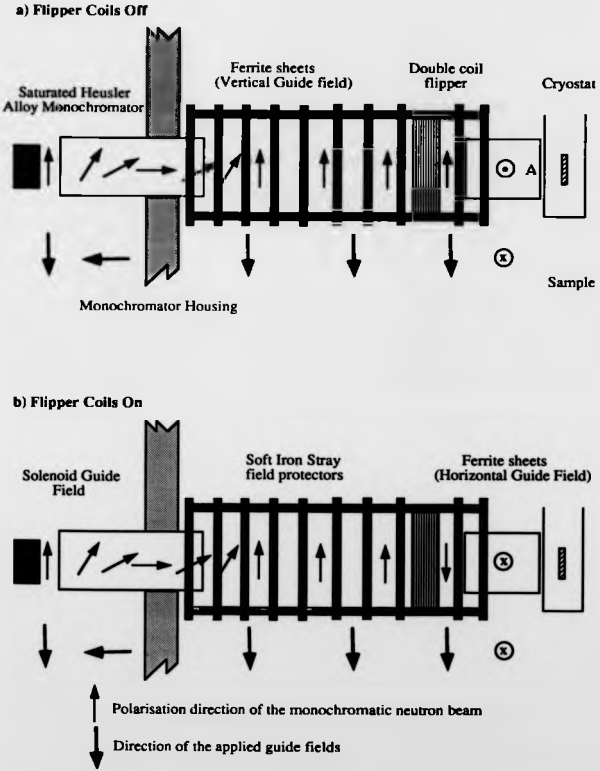

samples used in these investigations. This satisfies the condition for observing chirality domains as described in equation (35).

The facility exists on S20 to rotate the final polarisation either vertically or horizontally perpendicular to the beam direction by use of two guide fields constructed from pairs of magnetic ferrite sheets similar to those illustrated in figure 3.4. The polarisation can also be rotated along the beam direction by applying a sufficiently large field to a solenoid, which surrounds the neutron beam with its axis along the neutron beam. This ability to rotate the polarisation of the incident neutron beam allows a great deal of flexibility for the initial sample orientation.

3.4 Neutron topography.

Since the first published trials of neutron topography by Doi et al (1971), in which contrast effects were observed on a single crystal of germanium, there has been a natural progression in the research applications of this technique. In 1973 Schlenker & Schull observed ferromagnetic domains in Co-Fe, and this was followed by the observation of antiferromagnetic domains in NiO by Baruchel, Schlenker and Roth (1977). Then in 1981 (Baruchel et al), following an attempt to explain hysteretic behaviour in elastic constant measurements where chirality domains were inferred, these domains were imaged for the first time in the helically antiferromagnetic system of terbium.

The basic technique of neutron diffraction topography (Schlenker & Baruchel (1986)), involves recording the spatial distribution of the diffracted intensity from a single crystal sample bathed in an incident monochromatic neutron beam, as illustrated in the schematic diagram of Figure 3.5. The specific regions of the sample which contribute to the diffracted intensity correspond to regions satisfying the Bragg condition for a family of hkl crystalline planes at a given position. The direct recording of this intensity on a photographic medium would allow a simple translational mapping of the internal structure

Figure 3.5: The basic technique of Neutron Topography

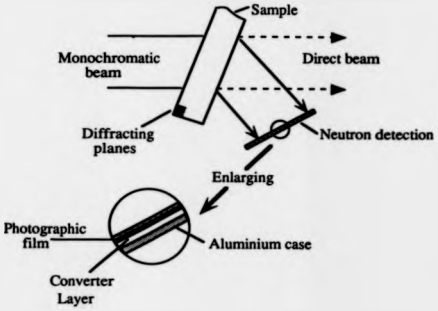

Table 1. The neutron density required for the adequate exposure of a range of photographic films and their intrinsic resolution.

Film Type	Neutrons / cm^2 required	Approximate Intrinsic resolution (μm)
Polaroid 667	$3 .10^5$	300
Agfa Osray	$6.5 .10^6$	100
Kodak Ektaspeed	$1.1 .10^7$	40
Kodak Ultraspeed	$2.2 .10^7$	30
Kodak AX	$3.0 .10^7$	20
Kodak MX	$7.2 .10^7$	15
Kodak M	$1.2 .10^8$	10
Kodak R	$8.0 .10^8$	3

of the sample onto a two dimensional image. This being the case it is clear that topography samples should be of platelet shape and good crystalline quality, thus avoiding complicated analysis caused by the superposition of differing contrasts, originating from various depths within the crystal.

3.4a Topographic detection of diffracted neutrons.

Unfortunately, the interaction of neutrons with sensitive photographic film is very weak and as such we are obliged to use a converter to produce either an electron, a photon or an alpha particle to expose the film. Early trials using ^{6}LiF (a neutron to alpha particle converter), where the α particles actually created defects in polymer emulsions were found to be unsuitable (Malgrange et al. 1976), mainly because these films are very fragile, and have the added disadvantage of producing low contrast topographs.

The converter presently used is a 9μm thick foil of enriched ^{157}Gd which undergoes a nuclear reaction on interaction with a thermal neutron to produce an electron. The emitted electron is then recorded on standard x-ray films. Maximum resolution is achieved by mounting the x-ray film in contact with the gadolinium converter. There are a wide range of x-ray films available, and Table 1 indicates the amount of neutrons per cm^2 required for an adequate exposure of each film together with their intrinsic resolution. These values give typical exposure times between 2 to 36 hours. A much quicker alternative (but obviously at the cost of resolution), is to use normal Polaroid film with a ^{6}LiF-(Ag)ZnS neutron to photon converter, via an α particle (Wang et al 1962, and Smith 1962). This is particularly useful in alignment and preliminary measurements as exposure times are reduced to the order of minutes.

3.5 Synchrotron radiation topography.

White beam synchrotron radiation topography (as described by Miltat & Sauvage-Simkin 1984), has been used for the indirect observation of phase coexistence in this investigation. Figure 3.6 shows a schematic diagram of the apparatus used on

Figure 3.6. A schematic diagram of the white beam synchrotron radiation topography station on the D25 beam line at L.U.R.E.

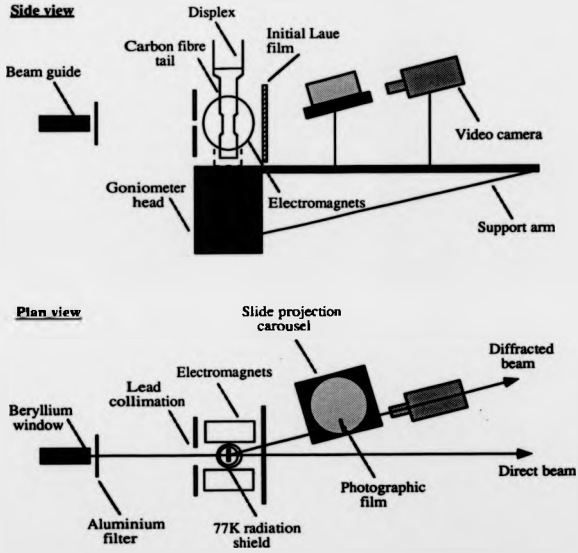

D25. Whilst there are many similarities with the previously described neutron case the differences serve to highlight the intrinsic properties of synchrotron radiation.

The white beam which emerges from the beryllium window of the beam guide is filtered by a 1 mm thick piece of aluminium. The aluminium filter removes the low energy photons and so reduces the excess heating of the sample, which even after filtering was still measured to be of the order of 10K on the MnP samples used. The beam size is then critically collimated to the sample shape by two pairs of lead slits.

As in the neutron case the sample is housed in a "Displex" closed cycle helium cooler. There are however two slight modifications, as the outer casing is fabricated from woven carbon fibre to reduce the absorption effects (previously fabricated from aluminium), and there are two small holes in the 77K radiation shield to allow the x-rays to pass unhindered through the sample. External magnetic fields can be applied in both the horizontal and vertical directions using the two electromagnets previously described in section 3.2.

The synchrotron radiation at LURE is polarised in the horizontal plane and this produces two different dependencies of the scattering cross-section in the horizontal and vertical planes. Across the vertical plane the scattering cross-section is constant and the beam divergence is approximately 20" of arc. In the horizontal plane the scattering is dependent on a $\cos 2\theta$ factor, where θ is the angle of diffraction in the horizontal plane away from the incident direction and the divergence has an increased value of a few seconds of arc. Consequently the diffraction vector is always taken in the vertical direction, thus avoiding any $\cos 2\theta$ dependence. The low divergence of the beam produces a Laue diffraction pattern when the sample is placed in transmission geometry as illustrated in figure 3.7. Each of these "spots" corresponds to a given topographic image when recorded on film. The ionizing nature of synchrotron radiation allows the diffracted beam to be detected directly onto x-ray film and its characteristic high flux (between 10^6 and 10^7 photons/mm^2/second), removes the previous temporal restrictions imposed in

Figure 3.7. The Laue diffraction pattern produce from a sample placed in transmission geometry

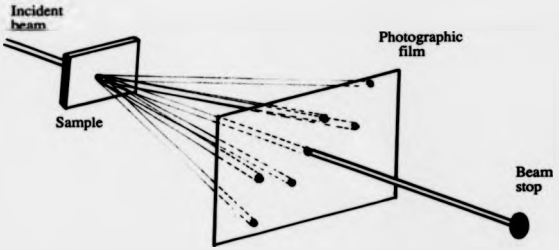

Figure 3.8. The variation of diffracted intensity from two regions of different structure factor.

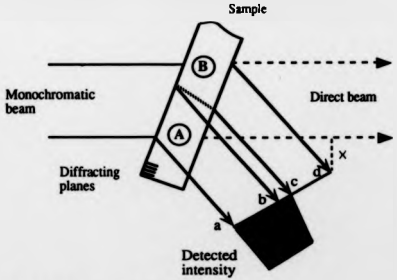

Structure factor in A is non zero

Structure factor in B is approximately zero

neutron work and permits the use of higher resolution films (e.g. MX, AX), at exposure times of the order of 10-15 seconds. Short wavelength x-rays were used (typically of the order of 1Å), in order to reduce both absorption effects and $\lambda/2$ contamination.

The real time imaging of the phase coexistence throughout a phase transition is possible by placing a video camera (equipped with a Gd_2SO_4, terbium doped x-ray to β particle coverter), on a given reflection and varying the sample conditions. This process is often necessary simply to locate the transition in the temperature domain, as it is not possible to measure the actual sample temperature due to the localised beam heating and the fragility of the sample. Once located the individual topographs are taken by exposing the x-ray film to the diffracted beam for a measured time period. The exposure procedure is performed using a manually controlled lead encased slide projector carousel. The topographs are placed into the diffracted beam for a specific time period which allows the continuous illumination of the sample by the incident beam. In this way the heating effect at the sample surface is kept constant.

3.6 Formation of images.

The formation of contrast on topographic images is subject to the condition that a localised variation of a given diffraction parameter exists across the sample. That is to say that a uniformly perfect, non deformed, single domain crystal will produce a uniformly grey image. Likewise, a uniformly deformed and imperfect crystal will also produce a uniformly grey image. The only distinguishing feature between the two being their relative diffracted intensities, and hence their exposure times. We will now describe the various mechanisms that can lead to a contrast on topographic images.

3.6a Variation of the structure factor.

Variation of the structure factor across the sample will occur in the case of magnetic domains, where a given domain exhibits a particular structure factor, as illustrated in figure 3.8. In the particular case illustrated, the region marked A has a non

zero structure factor and thus diffracts a constant intensity between a and b. The radiation which passes through the boundary between A and B will diffract a reduced value due to the diffracting volume which has a near zero structure factor in region B. From c to d the detected intensity will be near zero and constant. This mechanism is particularly important in helical antiferromagnetic systems, since it provides the only method of imaging chirality domains and as such is the main image formation mechanism used in neutron diffraction topography. In this case the Bragg diffraction is either purely nuclear (structure factor F_N), or purely magnetic (structure factor F_M). By considering the magnetic scattering under polarised neutron conditions, where the polarisation vector is parallel to the propagation vector of the helix, the structure factor for one type of chiral domain can be reduced to zero. Reversing the polarisation will produce a zero valued structure factor for the opposite chirality. Thus when imaging a magnetic satellite, neutrons will only be diffracted by one chirality in a given polarisation and on reversing the polarisation the opposite chirality domains will diffract.

In the case of synchrotron radiation the variation of structure factor does not exist between the two enantiomorphs of the chiral system. Moreover, with the exception of the very novel experiments carried at on magnetic resonance x-ray scattering the structure factors for purely magnetic x-ray scattering are very small compared to nuclear scattering and thus undetectable for these purposes. The mechanism of structure factor contrast thus plays a minor role in the formation of images in synchrotron topography .

3.6b Misorientation contrast.

The basic principle of misorientation contrast involves one region of the sample satisfying the Bragg condition in an incident monochromatic beam, whilst an adjacent region may only be partially or non diffracting. This effect could be caused by angular misorientations related to strain gradients, twinning, or subgrain boundaries for example. It should be stated that these misorientations will not necessarily lead to the same contrast on all reflections as quite frequently these effects are anisotropic. Their observation is also

dependent on the localised misorientation being large enough with respect to the divergence of the incident beam. Consequently misorientation contrast plays a more influencial role in the synchrotron topography work where the divergence is typically an order of magnitude less than that of the neutron case.

3.6c Extinction contrast.

Extinction contrast involves the formation of a "direct image" due to a localised reduction of extinction and is common in materials where absorption effects are weak, as described by Authier (1967) and Armstrong (1980). Consider a dislocation surrounded by a perfect crystal matrix which will diffract according to the dynamical theory. A strain field will occur around the defect, and will result in a localised crystal volume which diffracts an increased intensity to that of the surrounding regions due to a localised reduction of extinction. Extinction contrast is obviously limited to the condition that the relative change in intensity between the strained region and the bulk sample is large enough to be imaged. Such a condition implies very good crystal quality, but is also dependent on the reflection, the incident wavelength, and the crystal thickness.

Extinction contrast can also be applied to imaging phase boundaries when the difference in lattice parameter between the two phases can be sufficient to cause a localised stress field, and hence a reduction in extinction. An example of extinction contrast in neutron topography is given in chapter four.

It is this localised stress field which is the main contributory factor to the indirect imaging of phase coexistence in synchrotron topography. In fact what is actually imaged is the phase boundary as it passes across the sample on changing the temperature or applied magnetic field. An example of this effect will be shown in chapter four on the MnP system.

Special care must be taken with synchrotron radiation when dealing with highly absorbing crystals as the diffraction properties change substantially as a result of the

Borrmann effect (Batterman & Cole 1964). In this regime the highly perfect crystal regions which previously diffracted weakly now diffract more intensely than the deformed regions. The classification for the onset of the Borrmann effect is given from the simple product of the neutron path length in a crystal (t) multiplied by its absorption coefficient (μ). The Borrmann effect can be neglected when μt is less than two, which is the case on the manganese phosphide samples studied in this work. With an approximate thickness of 150 μm and an incident wavelength of 1Å the μt product is of the order of one.

3.7 The resolution of neutron and synchrotron topography.

There are four main parameters which contribute to the actual resolution of a recorded topograph; statistical fluctuations of recorded radiation, photographic detection, instrumental resolution, and the intrinsic defect size. These contributory effects are considered individually.

3.7a Statistical fluctuations.

The limited neutron flux present on S20, is such that statistical fluctuations must be taken into account when considering neutron image formation. For example producing an adequate exposure on CX film requires 3.10^7 neutrons per cm^2, which corresponds to a total count of only 30 neutrons over an area of $10*10\ \mu m^2$. The best possible resolution available from such a neutron signal was calculated in 1983 by Baruchel et al to be ~30μm. The high flux associated with synchrotron sources ensures that the statistical fluctuations produce a limiting value of less than 10μm to the resolution.

3.7b Photographic detection.

The photographic detection of incoming neutrons relies on the isotropic nuclear emission of a beta particle from the ^{157}Gd converter to expose the film. By placing the

film in direct contact with the converter, the possible exposure radius is ~ 20 μm around the actual position of the incoming neutron as described by Berger (1963).

As synchrotron radiation does not require a converter to expose photographic film, the resolution limit can be severely reduced as long as the photographic detector is placed parallel to the reflecting planes of the sample. This ensures that the detection is a point and not an extended line through the depth of the photographic emulsion. The resolution limit of the detection of x-rays is thus limited by the intrinsic resolution of the of the x-ray films as listed in table 1.

3.7c Direct image size.

The intrinsic size of the "direct images" is not solely related to the defect size, but it is also inversely proportional to the Darwin width of the considered region of the sample. The Darwin width is dependent on the neutron wavelength and the structure factor of the reflection, hence increasing either of these parameters will allow the beam to diffract from more misoriented regions nearer to the heart of the defect, thus improving the resolution of the technique. Increasing the divergence of the incoming beam will have a similar effect, but unfortunately at the cost of the geometric resolution as will be seen in the following section. These effects are minimal in this particular investigation as we have seldom studied the nuclear peaks in neutron topography and the main mechanism employed in the synchrotron work has been that of extinction contrast.

3.7d Geometrical resolution.

The inherent simplicity of white beam synchrotron radiation topography reduces the geometrical resolution to the product of the divergence of the diffracted beam emanating from a point within the sample (Φ), and the distance from this point to the photographic film (l).

$$R = l * \Phi \qquad (66)$$

Evidently the resolution of the technique is optimised by placing the film as near to the sample as possible, whilst ensuring that the direct beam does not impinge on the topographic image.

The above factors still hold for neutron diffraction topography, but as will be shown shortly the system is a little more complex due to the inclusion of a selection of monochromators and the variable orientation of the sample. The minimum distance at which the topographic camera can be set is clearly more critical in the neutron case due to the large beam divergence. Although this value was calculated by Baruchel (1980), the external limitation of 2.0 cm due to the outer casing of the displex tail on S20 is generally larger and as such can be taken as the minimum film to sample distance.

The instrumental divergence can be separated into a horizontal component (Φ_h), and a vertical component (Φ_v). This later component is dependent on the vertical divergence of the incident neutron beam (α_v), and the vertical mosaic spread (η_{mv}) of the monochromator as shown below;

$$\Phi_v = [(\alpha_v)^2 + (\eta_{mv})^2]^{1/2} \qquad (67)$$

The expression for the horizontal component must also take into consideration the diffraction geometry of the particular reflection, which determines the value of $\mathfrak{C}$ (the full width half maximum of the rocking curve). The value of $\mathfrak{C}$ is given (in a simple form which corresponds to that of S20) by Dachs (1978) as,

$$\mathfrak{C} = [(2 - A)^2 . (\eta_{mh})^2 + (1- A)^2 . (\alpha_h)^2 + (\eta_s)^2]^{1/2} \qquad (68)$$

Where $A = \tan \theta_s / \tan \theta_m$, and θ_s and θ_m are the Bragg angles at the sample and monochromator respectively. α_h is the horizontal divergence of the incident white beam, and η_{mh} is the horizontal mosaic spread of the monochromator.

Usually, η_s (the sample mosaic spread) is much smaller than the other two terms involving α_h and η_{mh}.

The horizontal divergence can then be derived from the work of Werner (1971), with the specific adaptation to the case of S20, neglecting secondary collimation effects to give:

$$\Phi_h = (A . \alpha_h . \eta_{mh}) / \mathcal{C} \qquad (69)$$

α_h varies with neutron wavelength within the beam guide as the critical angle for total internal reflection is also wavelength dependent. The following empirical formula can be applied to the neutron radiation within the guide

$$\alpha = 10 \lambda \qquad (70)$$

where the divergence α is in minutes of arc and the wavelength is in angstroms.

S20 is however situated several meters after the end of the guide and hence the variation of α as a function of λ is a little more complicated. The experimental results obtained on holmium when using a monochromator with a negligible mosaic spread lead to the wavelength dependence of the horizontal divergence shown in Figure 3.9. On fixing the sample to film distance at 2 cm, the geometric resolution of the instrument can be calculated by substituting values for the horizontal beam divergence at a given wavelength, the mosaic spread of the monochromator, and the corresponding Bragg angle into equation (69). The resolution response to a change in sample Bragg angle at a fixed wavelength of 1.7Å is illustrated in Figure 3.10. Values of Bragg angle smaller than 22 degrees have not been plotted as in this condition the the sample to film distance is increased dramatically (in order to separate the transmitted and diffracted beams), which severely reduces the resolution.

Figure 3.9 The variation of the horizontal divergence as a function of the incident neutron wavelength for the instrument S20

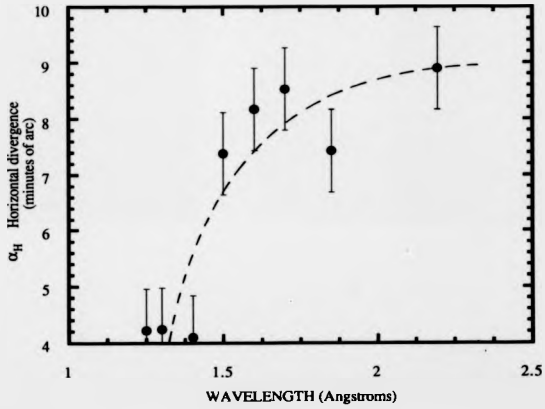

The dashed line is a guide for the eye

Figure 3.10: The geometrical resolution (microns) as a function of the incident Bragg angle at the sample.

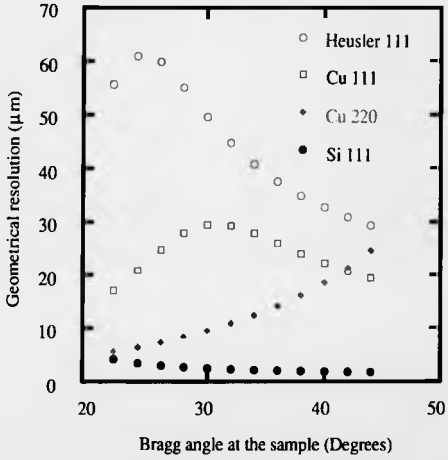

The Cu 111, Cu 220 and Si 111 monochromators can be seen to give a relatively small and homogeneous resolution (< 30 μm), which is almost insignificant when convoluted with the resolution loss of the other effective parameters. It is clear that the worst case scenario, and one which has been frequently employed (due to the need for polarised neutrons), is that of the Heusler alloy 111 reflection. In this case for Bragg angles around 25 degrees the geometrical resolution will be the major cause of resolution loss.

However, the geometrical resolution is only of interest when recording diffraction topographs. When measuring rocking curve widths and peak positions in diffraction scans then a large angular resolution is required. The angular resolution is related to the expression for the FWHM of a reflection (equation 68) from which it can be seen that if the ratio of the tangents of the sample and monochromator Bragg angles are equal then T will be a minimum. This is in fact the case for the Si 111 reflection at 1.7Å and the holmium 002 reflections and hence the Si 111 monochromator was used for some of the diffraction scans taken on holmium in chapter six.

The silicon 111 monochromator is unusual in that it has been annealed in a controlled environment to diffuse oxygen into its structure, which has the advantage of increasing the diffracted intensity by a factor of 40 times that of pure silicon. By diffusing oxygen into the silicon lattice the mosaic spread is increased, but as pure silicon can be grown to such perfection the mosaic remains less than one minute of arc after the diffusion process.

The convolution of the monochromator mosaic spread (which ranges on S20 from 12 minutes of arc for the Heusler alloy to less than one minute of arc for the silicon 111), with the above parameters gives a conservative estimate of the geometric resolution of S20 as 50 ± 5 μm.

In brief the convolution of these four parameters yields a limiting resolution of 60 ± 5 μm to the technique of polarised neutron diffraction topography, a value which falls to 50 ± 5 μm when using one of the three non polarising monochromators available on S20. The most critical parameter is the geometrical resolution of the instrument. The convoluted resolution of the synchrotron case is approxiamately 10 μm. This value is principally influenced by the divergence of the diffracted beam.

3.8 Magnetisation measurements.

By applying a magnetic field to a magnetic sample surrounded by a pick up coil, and by extracting the sample the signal detected in the coil will be proportional to the sample magnetisation. A precise value of the magnetisation can be obtained by comparing the signal detected with sample inside the coils, to the zero valued signal after extraction. The technique of axial extraction requires a stable magnetic field, which in this particular case, was produced by an 8 Tesla superconducting magnet at the Laboratoire Louis Néel, Grenoble.

The samples were mounted on a non-magnetic sample holder normally just at one point by GE varnish. The temperature was controlled by a standard helium flow cryostat which gave a temperature range of from 4.2 to 300K with an accuracy in regulation, of $\pm$ 0.01K.

3.9 Determination of elemental composition by S.E.M.

Using a scanning electron microscope in normal mode is a very accurate method for observing surface 'topography'. There is however a second possibility to use the SEM as an elemental sub surface probe by exciting a given sample volume and analysing the emitted x-rays. In order to do this the detector and analyser should be calibrated using a standard cobalt sample, at a given angle of incidence (30 degrees in this particular case) to an electron beam of known energy. The depth of the excited region (which is teardrop

in volume), is dependent on both the sample density and incident electron energy and is given as approximately 1.5 μm for Cr -0.6 at. % Si at 10 keV. The illuminated surface area of the sample is controlled by a variable aperture and focussing mechanism.

The experiments were carried out on a Cambridge S250 mark III scanning electron microscope at an incident energy of 10 keV. The spot size was fixed at 1μm during localised elemental analysis, but was increased to around 10 μm for the x ray mapping. By simply selecting a binary elemental trace it was possible to have an accuracy ± 0.3 atomic percent in the detected composition of the sample. The sample was mounted on the device head using silver paste to ensure good electrical contact.

3.10 The measurement of elastic constants.

By measuring the velocity of ultrasound υ in a material it is possible to deduce the elastic constant C_{ij} from the following relation:

$$C_{ij} = \rho \upsilon^2 \qquad (71)$$

where ρ is the material density. In the particular case studied, (Cr-0.6% Si which has a body centered cubic crystal structure), a longitudinally polarised ultrasonic pulse propagating down a (100) direction is related directly to C_{44}. The velocity of the ultrasound is measured by producing a suitable trigger frequency to overlap two ultrasonic echoes on an oscilloscope. This trigger frequency is the inverse of the time period between the two echoes, which when multiplied by the ultrasonic path length will yield the ultrasonic velocity, and hence the elastic constant.

A 15 MHz RF pulse was applied to a gold plated quartz transducer, bonded to the sample with epoxy resin and used to generate and detect the the ultrasonic pulse. On detection of the first selected echo, the oscilloscope was initially triggered and then re-triggered a short time later at the arrival of the second echo. The time lapse between these two events is sufficiently small (a few micro seconds), to allow both images to be retained

on the oscilloscope. The image is stabilised by repeating this operation at a frequency two orders of magnitude down on the trigger pulse. The echoes are overlapped by manually changing the trigger frequency from a frequency generator to superimpose the two peaks on the oscilloscope screen. Particular care must be taken when passing through phase transitions as the attenuation due to critical phenomena can become so large that the echoes are momentarily lost.

A standard Oxford Instruments liquid flow cryostat gave a range of temperatures from 10 to 300K with an absolute accuracy of ± 1.0K. The resolution of the technique is dependent on the sensitivity of the frequency synthesizer, and the stability of the echoes but is typically one part in 10^4.

CHAPTER FOUR

PHASE COEXISTENCE (I).

4.1 Introduction.

This chapter will deal with magnetic phase coexistence as observed in the first order transitions of chromium-0.6 atomic percent silicon, terbium and manganese phosphide. The driving mechanism of the phase coexistence will be described for each of the above systems, with particular attention being paid to the effect this has on the phase boundary.

The first case discussed is that of chromium-0.6 atomic percent silicon, where initial measurements of the C_{44} elastic constant indicated a broadening of the transition from the paramagnetic to the transverse spin density wave (TSDW) phase. The same effect was also observed on the spin flip (TSDW to LSDW) transition. The low temperature spin reorientation transition was investigated further by a combination of neutron diffraction, topography and sample annealing techniques. Finally a compositional analysis of the annealed topography sample was undertaken to hopefully give conclusive evidence of a variation of silicon concentration across the sample volume.

Phase coexistence is also observed on the first order transition from the helimagnetic to ferromagnetic phase in terbium. Crossing the phase boundary can be achieved either by cooling from the helimagnetic phase (or warming from the ferromagnetic phase) in zero field, or by the application of a magnetic field at a constant temperature within the helimagnetic phase. In the later case the phase coexistence will be stable over a range of externally applied magnetic field. This phase coexistence range in the "field driven" case is principally dependent on the sample shape and the demagnetising field necessary to provide a constant internal field within the sample. The phase boundary

orientation will be determined from the contributions of the two above mentioned effects along with those related to the elastic and phase boundary energies.

In comparison the passage from the helimagnetic to ferromagnetic phase in zero field conditions occurs at a given temperature. Manganese phosphide and terbium both exhibit such a phase transition, where the phase boundary conditions are dependent on the competition between the magnetostatic energy, the elastic compatibility and the energy of the phase boundary. The experimental data for these transitions were produced by neutron and synchrotron radiation topography.

4.2 Chromium-0.6 atomic percent silicon.

All of the results presented in this section were taken from two samples which were cut from the same chromium-0.6 atomic percent silicon single crystal sample as previously investigated by Palmer et al (1988). Figure 4.1 illustrates the dimensions of the samples and their crystallographic orientation by marking the two faces which are perpendicular to the [100] and [110] directions. The upper, thinner sample ($t_o \approx 0.5$mm) will be referred to from here onwards as the topography platelet and the thicker section ($t_o \approx 5.5$mm) as the bulk sample. The initial condition of the samples after spark erosion and polishing are referred to as being "as produced" as opposed to "after annealing", when both the above described samples were annealed at 950°C in an inert argon atmosphere for a period of 96 hours.

The transition from the paramagnetic to the incommensurate transverse spin density wave phase has been investigated by propagating a longitudinally polarised ultrasonic pulse down a [110] crystalline direction of the bulk sample and measuring the C_{44} elastic constant. Figure 4.2 illustrates the temperature variation of the C_{44} elastic constant across this transition for the bulk sample in both the as produced and after annealing states. The temperature variation of the C_{44} elastic constant was also measured (figure 4.3) across the low temperature spin flip transition from a TSDW to a LSDW

Figure 4.1. A schematic diagram of the physical dimensions and crystallographic orientation of the two chromium-0.6 atomic percent silicon samples.

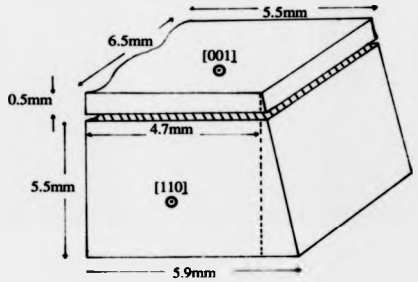

Figure 4.2. The temperature variation of the C_{44} elastic constant across the transition from a paramagnetic to a TSDW phase in both the as prepared and the annealed sample states.

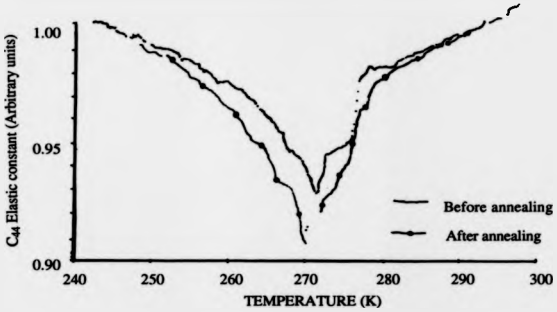

Figure 4.3. The temperature variation of the C_{44} elastic constant across the low temperature spin flip transition from a TSDW to a LSDW phase in both the as prepared and the annealed sample states.

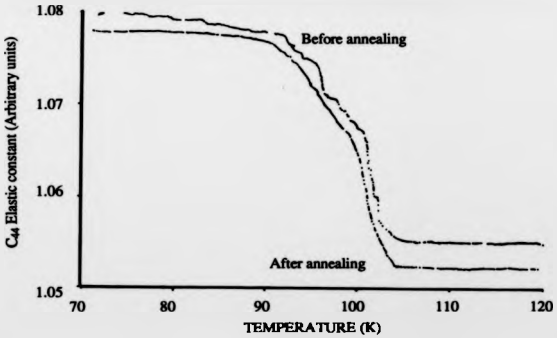

phase for both sample states. A general trend which can be seen from both these sets of ultrasonic data is that the lineshape of the annealed data appears to have a smoother form than that of the as prepared sample.

Figure 4.4 shows the temperature variation of the intensity of the [0,0,0+τ] magnetic satellites and the (0,0,1) 'nuclear like peak' as detected on a series of omega-two theta scans taken along the [001] direction. These data were taken on the topography platelet (as were all the following neutron data), in a 1.7Å monochromatic neutron beam. From the two peaks observed at both satellite positions it is clear that the sample contains a subgrain (the small shoulder in the wing of the large peak). This subgrain peak is misoriented from the main peak of the magnetic reflection for these particular lattice planes by approximately 9 minutes of arc. On reducing the temperature the intensity of the satellite reflections diminish, and the peak intensity position is slightly shifted so that it resides mainly on the small misoriented subgrain in the base of the transition.

Figure 4.5 shows a combination of neutron diffraction and neutron diffraction topography data taken on the [0,0,0+τ] magnetic reflection of the topography platelet in the as produced state. The neutron diffraction data in this figure represent the intensity values detected on the peak position of the [0,0,0+τ] reflection as a function of temperature. The neutron topographs which are plotted indicate the regions of the sample which have a [0,0,0+τ] propagation vector and are in the TSDW phase at a given position of the intensity plot. These recorded intensity regions on the topographs of figure 4.5 & 4.6 clearly decrease non uniformly as a function of temperature.

Figure 4.6 illustrates exactly the same type of data as those displayed in the previous figure with the exception that these data were recorded on the temperature annealed topography platelet. After studying the high temperature paramagnetic and low temperature spin flip transitions through neutron and ultrasonic techniques the next step was to directly measure the the silicon concentration of the sample.

Figure 4.4. The diffracted intensity measured from the as produced sample in an omega-two theta scan along the (001) direction as function of the sample temperature.

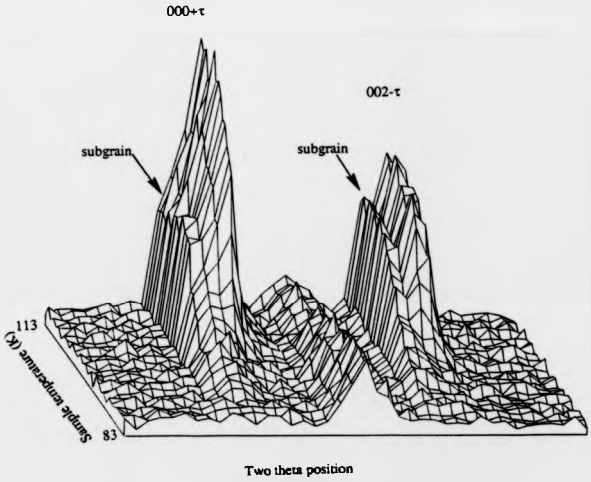

Figure 4.5. The temperature variation of the peak diffracted intensity detected on the 000+τ magnetic reflection of the as prepared topography platelet and the associated neutron diffraction topographs showing the regions of the sample which are in the TSDW phase for the above propagation vector.

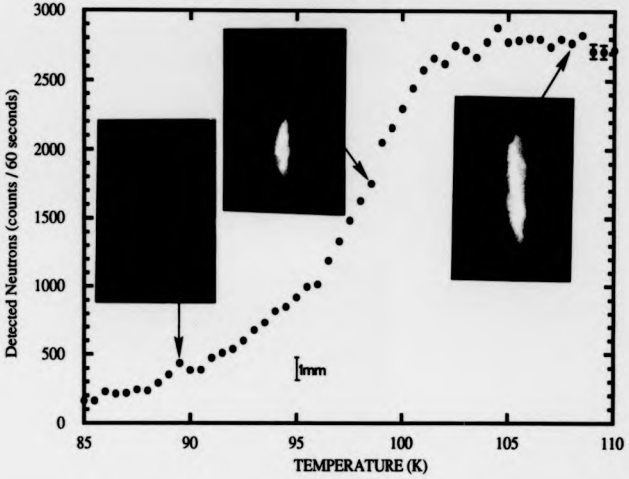

Figure 4.6. The temperature variation of the peak diffracted intensity detected on the 000+τ magnetic reflection of the annealed topography platelet and the associated neutron diffraction topographs showing the regions of the sample which are in the TSDW phase for the above propagation vector.

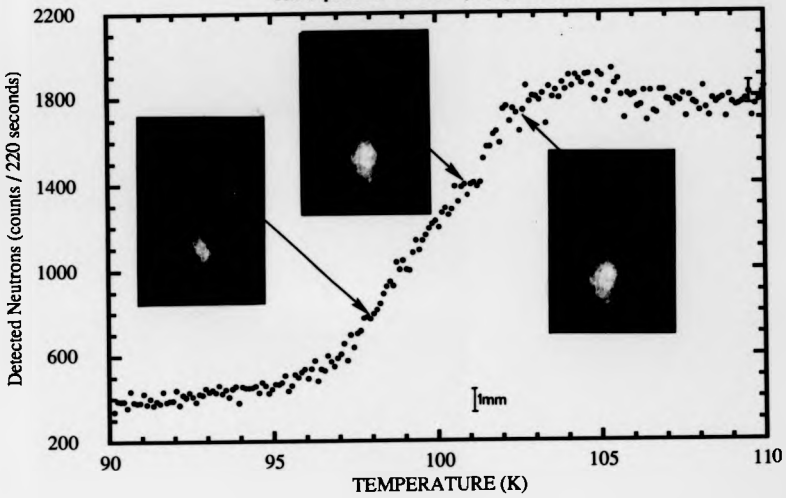

Figure 4.7 shows such an analysis as was performed on an initial nine point by nine point lattice mapping on the unpolished surface of the annealed topograph platelet, by the spectral analysis of x-rays which have been back scattered from a sample illuminated by the electron beam of a scanning electron microscope. The numerical values included in this figure represent the atomic percentages of silicon which were detected from a specific position (as marked on the scaled diagram) of the sample surface. In each of these measurements the electron beam was limited to an incident area of 2 μm^2 and the microprobe was set to detect the two major alloy components ie. silicon and chromium. Figure 4.8. shows an electron micrograph of the sample surface after it had been polished with 1 μm diamond paste. The surface of the sample can be seen to be covered by a series of small pit-like defects.

These pitted regions were then closely examined by localised probing using a reduced incident beam diameter of approximately 1 μm. Figure 4.9 shows an enlarged region of the sample which contains one of these pit defects. Marked on this figure are the positions of the three regions which were locally scanned for their silicon content. The defect itself contains a very high silicon content, but this decreases rapidly on moving radially outward from the defect position, with the silicon content falling from nearly 92 percent on the defect to values of 0.26 and 0.78 percent only 4μm either side of the defect.

Figure 4.10a indicates the specific regions (B and C), on the sample surface where the two respective electron micrographs of figure 4.10b & 4.10c were taken. At position B the density of pits was measured as 120 defects in an area approximately 720 by 540 μm^2, whilst at position C this value was reduced to only 81 defects in the same area. The difference in defect density between both of these regions, is thought to correspond to the regions of different silicon concentration seen in figure 4.7.

Figure 4.7. An schematic diagram showing the silicon content which was measured over a coarse lattice on localised $2\mu m^2$ excited regions of the surface of the annealed unpolished topography platelet.

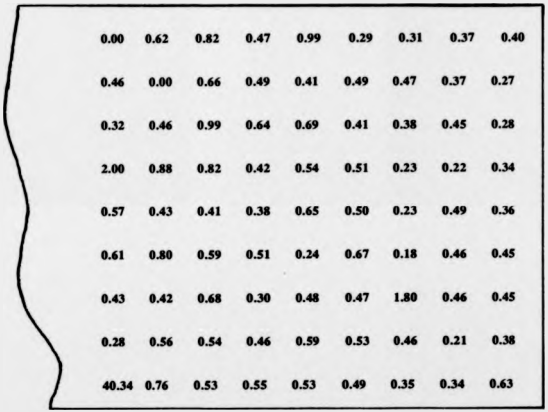

0.00	0.62	0.82	0.47	0.99	0.29	0.31	0.37	0.40
0.46	0.00	0.66	0.49	0.41	0.49	0.47	0.37	0.27
0.32	0.46	0.99	0.64	0.69	0.41	0.38	0.45	0.28
2.00	0.88	0.82	0.42	0.54	0.51	0.23	0.22	0.34
0.57	0.43	0.41	0.38	0.65	0.50	0.23	0.49	0.36
0.61	0.80	0.59	0.51	0.24	0.67	0.18	0.46	0.45
0.43	0.42	0.68	0.30	0.48	0.47	1.80	0.46	0.45
0.28	0.56	0.54	0.46	0.59	0.53	0.46	0.21	0.38
40.34	0.76	0.53	0.55	0.53	0.49	0.35	0.34	0.63

Figure 4.8. An electron micrograph of a region of the surface of the annealed and polished topography platelet.

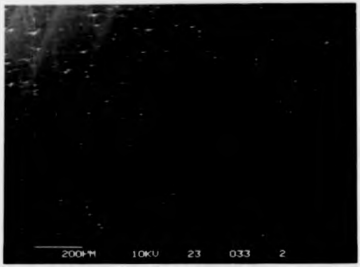

Figure 4.9. An electron micrograph of one of the many surface pit defects with the measured values of the silicon content (in atomic percent) displayed at the locations of the localized scans.

Figure 4.10. A schematic diagram (a) indicates the regions of the sample surface where the two electron micrographs shown in (b) and (c) were measured.

(a) The sample surface

(b) The electron micrograph taken at B

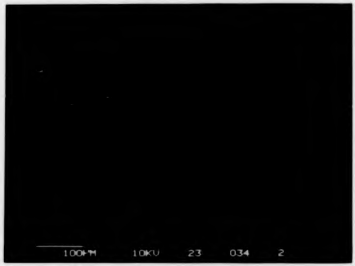

(c) The electron micrograph taken at C

An x-ray mapping was then performed across the whole surface of the polished sample (which had approximately 18 μm removed from its thickness during polishing) where the detector was only set to detect the x-ray spectrum related to regions of the sample surface which contain silicon. The variation of this intensity data can be seen figure 4.11.

Figure 4.12 shows two neutron topographs which were both taken on the reflection in the middle of the spin flip transition at 102.5K on the annealed sample. The difference between the two topographs is that figure 4.12b was taken after the sample had been thermally cycled through the transition and reset to 102.5K. Both topographs show the same phase interfaces and only minor differences in their intensity distributions can be seen as a function of thermal cycling.

4.2a Discussion.

From the brief introduction to the magnetic properties of Cr-0.6 at.% Si given in chapter one, there is a certain ambiguity about the nature of the phase transition from the paramagnetic to the incommensurate transverse spin density wave phase. The original results of Palmer et al (1988) were remeasured at the high temperature transition as well as at the spin flip transition on the bulk as produced sample. The temperature variation of the C_{44} elastic constant data taken on this sample (shown in figures 4.2 and 4.3), indicate three distinct temperature ranges within both transitions where the rate of change of elastic constant with temperature undergoes an abrupt change. These anomalous changes in the elastic constant result in a broadening of the overall width of the transition. A comparison of these data to those of the annealed sample in the same figures indicates that the annealing process appears to have produced a smoother lineshape to the transition and a narrower transition width.

The reduction of transition broadening after annealing could be interpreted as a reduction in the silicon inhomogeneity across the sample volume, but in order to clarify

Figure 4.11. An x-ray mapping depicting the silicon content detected at the surface of the topography sample.

Figure 4.12. Two neutron topographs taken on the 000+τ magnetic reflection at a) 102.5K upon descending in temperature into the TSDW phase and b) 102.5K after descending to 60K in the LSDW phase.

a) Before cycling.

b) After cycling.

this a more direct method of observation was required. The application of neutron diffraction techniques to this problem provide the average volume of one of the phases during the spin flip transition (which is very sensitive to the silicon content of the sample Mizuki et al. (1986)), through the analysis of the diffracted intensity, and as a direct image of this phase by neutron diffraction topography.

The spin flip transition is susceptible to observation by neutron diffraction when scanning along a four fold crystalline axis as a function of temperature. However, on scanning radially outward along a four fold axis the first diffraction centre (a (001)* reciprocal space position) will not be present due to the definition of the nuclear structure factor for a body centered crystal. Hence having passed this position the first detected intensity peak will correspond to the 002-τ magnetic satellite of the 002 nuclear peak, which is present. The spacing between the nuclear peak and its associated satellite reflections are very large (τ=0.952a*) and ordered along the cube axes. Consequently the absent (001)* position is surrounded by the satellites of its nearest lattice neighbours, as illustrated in figure 4.13. The nomenclature has been adopted where the 002-τ is actually referred to as the 001+q (where q=1-τ), and the 000+τ as the 001-q

Scanning along a four fold axis will therefore detect the neutrons which are diffracted from the TSDW when a component of the magnetic moment lies in the scattering plane. When the sample passes to the LSDW the magnetic moment will rotate parallel to the direction of propagation (which is out of the scattering plane), and as a result the detected intensity on the 0,0,1±q magnetic satellites will fall off to zero. The detection neutron intensity diffracted from the TSDW phase when scanning on the 001±q magnetic satellites will therefore give a direct indication of the specific regions of the sample which exhibit the TSDW phase at a given temperature.

The temperature variation of the omega-two theta scans plotted in figure 4.4 (which were taken with a relaxed detector collimation), show this reduction in intensity on the 0,0,1±q magnetic satellites. However, these data also indicate that an intensity has

Figure 4.13. The reciprocal space positioning of the magnetic satellites of the Cr-0.6%Si sample in the low temperature LSDW phase.

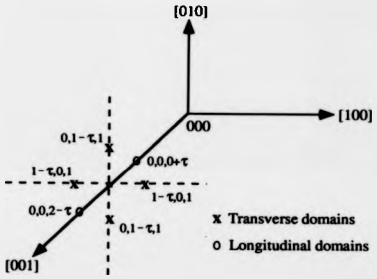

been detected on the absent (001)* position. This spurious intensity is related to the four transverse satellites (figure 4.13), which are situated so close to the absent position that they are detected in the acceptance of the detector. The increase in intensity (detected at the "nuclear position") on decreasing the temperature is a result of the relative orientation of the τ vectors of the transverse domains to the scattering plane when scanning along the [001] direction. In the high temperature TSDW phase only half of the possible transverse domains will have a magnetic moment component in the scattering plane. However, on passing into the LSDW phase all the possible transverse domains will show a component in the scattering plane. This spin rotation is detected on the absent position as an increase in the diffracted intensity as seen in figure 4.4.

The velocity of ultrasound and neutron diffraction data are detected as a volume average across the crystal, and hence any investigation into the properties of a specific region of the sample is not possible using these techniques. In order to clarify the broadening of the spin flip transition neutron diffraction topography was employed to directly image the TSDW phase on passing through the transition. Figure 4.5 shows the regions of the sample which have a $[0,0,+\tau]$ propagation vector and are in the TSDW phase being imaged as a function of temperature for both the annealed sample state. The images on these topographs clearly reduce inhomogeneously as a function of temperature, with isolated regions remaining in the TSDW phase even as low as 93K.

Topographs taken after annealing (figure 4.6.) show a more homogeneous distribution of intensity on passing through the transition than those of the "as produced" sample. However it should be noted that a direct comparison between the contrast on these two sets of topographs is difficult as a different domain has been considered in the "as produced" sample to that of the annealed case. Both sets of topographs do actually show that localised regions of intensity disappear on reducing temperature, which infers that specific regions of the sample pass through the spin flip transition at different temperatures. These localised variations in the topographic intensity invoke a variation in

the silicon content throughout the sample, as it is known that the addition of silicon to pure chromium has the effect of lowering the transition point in the alloys (Mizuki et al 1986). Hence if this effect is simply driven by a variation of the silicon content across the sample volume, then from the phase diagram of figure 1.14 the occurrence of the TSDW phase at 93K (figure 4.5) would imply a localised silicon concentration of 0.9 ± 0.05 atomic percent.

The topographs of figures 4.5 & 4.6 are indicated on the plot of the temperature variation of the peak diffracted intensities observed on the same satellite reflection, from which it is possible to extract the width of the spin slip transition for both sample states. The width of this transition can be seen to reduce from approximately 12K on the as produced sample to around 9K on the annealed sample. Again, by extrapolating the data of figure 1.14 these two transitions can be described by a silicon homogeneity of 0.75 ± 0.2 atomic percent for the as prepared sample (the transition centered at 97K with a width of 12K as seen in figure 4.5), and 0.70 ± 0.2 atomic percent for annealed sample (the transition centered at 99K with a width of 8K as seen in figure 4.6).

Having proposed a silicon concentration gradient as the driving mechanism of the phase coexistence in this particular chromium-silicon alloy, a quantitative measurement of the silicon content of the sample is necessary in order to validate this claim. From the initial measurements of the silicon content displayed in figure 4.7 it is clear that there is in fact a variation of the silicon distribution across the sample surface. It should be noted that these results are limited to a very localised excited sample volume (~3 μm^3) on a very coarse lattice grid which has a typical spacing between points of 0.3 mm. These values of the silicon concentration are however very close to those predicted from the phase diagram of Mizuki et al.(1986).

By polishing the sample it was hoped that the samples surface topography would be sufficiently reduced to allow the imaging of the backscattered x-rays which emanate solely from the silicon centres. However, after polishing with 1μm diamond paste the

sample surface appeared pitted (figure 4.8.), rendering it impossible to distinguish the images of the pitted regions from those of the silicon concentrations.

From the silicon concentration values displayed in figure 4.9 the pitted regions appear to be centres of very high silicon concentration. The large pit defect seen in this figure was measured to have a silicon content around 92 atomic percent. On moving only 4μm to either side of the defect, the silicon concentration was measured to be similar to previously detected values. This indicates that these pit defects are in fact extremely localised centres of high silicon concentration. These pit defects are not observed on the topographs because their size (typically several μm^2) is below the resolution of neutron topography. In addition these very high silicon concentration centres will diffract at a different Bragg angle to that of the surrounding matrix. It was hoped that the precipitation centres could be indirectly imaged through the distortion they impose on the crystalline lattice, but unfortunately this was not possible as the matrix was too imperfect to see this effect.

By calculating the pit density for a given surface area ($720 * 540\ \mu m^2$) of two specific regions of the sample surface (as described in figure 4.10a), and comparing this to the corresponding average silicon content detected in these two regions on the coarse scans taken in figure 4.7, a strong correlation can be seen. The data taken from an x-ray mapping as shown in figure 4.11 also shows that the surface silicon concentration varies with position. As in the previous data the top left hand corner of the sample can be seen to contain the largest silicon concentration.

These results indicate that there is in fact a distribution of the silicon content across the volume of the sample, as during polishing the thickness of the sample was reduced from 520 ± 2 μm to 502 ± 2 μm. This loss of around 18μm is by no means negligible when considering that all the surface silicon concentration measurements taken in this investigation were taken at a depth of only 1.5 μm. The annealing of the sample appears to have smoothed the overall distribution of silicon throughout the compound by

sample surface appeared pitted (figure 4.8.), rendering it impossible to distinguish the images of the pitted regions from those of the silicon concentrations.

From the silicon concentration values displayed in figure 4.9 the pitted regions appear to be centres of very high silicon concentration. The large pit defect seen in this figure was measured to have a silicon content around 92 atomic percent. On moving only 4μm to either side of the defect, the silicon concentration was measured to be similar to previously detected values. This indicates that these pit defects are in fact extremely localised centres of high silicon concentration. These pit defects are not observed on the topographs because their size (typically several μm^2) is below the resolution of neutron topography. In addition these very high silicon concentration centres will diffract at a different Bragg angle to that of the surrounding matrix. It was hoped that the precipitation centres could be indirectly imaged through the distortion they impose on the crystalline lattice, but unfortunately this was not possible as the matrix was too imperfect to see this effect.

By calculating the pit density for a given surface area (720 * 540 μm^2) of two specific regions of the sample surface (as described in figure 4.10a), and comparing this to the corresponding average silicon content detected in these two regions on the coarse scans taken in figure 4.7, a strong correlation can be seen. The data taken from an x-ray mapping as shown in figure 4.11 also shows that the surface silicon concentration varies with position. As in the previous data the top left hand corner of the sample can be seen to contain the largest silicon concentration.

These results indicate that there is in fact a distribution of the silicon content across the volume of the sample, as during polishing the thickness of the sample was reduced from 520 ± 2 μm to 502 ± 2 μm. This loss of around 18μm is by no means negligible when considering that all the surface silicon concentration measurements taken in this investigation were taken at a depth of only 1.5 μm. The annealing of the sample appears to have smoothed the overall distribution of silicon throughout the compound by

diffusing silicon to a series of small, highly localised precipitation centres. As these regions will not be detected on any of the neutron data the actual silicon concentration observed by the neutron technique will appear as less than that of the as prepared sample. This effect can be seen from the two transitions illustrated in figures 4.5 & 4.6, where in the as prepared state the transition occurs from 90K to 102K and on annealing the sample these temperatures are elevated to 95K and 103K respectively. These results indicate that, there is a reduction of silicon content within the sample matrix and that the diffracted neutrons associated with the precipitate centers are not detected.

The compositional fluctuations (seen as a variation of intensity on the neutron topographs of figures 4.5, 4.6 & 4.12), can be related to the broadening of the transition observed in the ultrasonic and neutron diffraction data. On passing through the transition a given silicon concentration will produce a first order transition at a specific temperature (Mizuki et al. 1986). As the sample is composed of regions of slightly different composition, each region will pass through the spin flip transition at a different temperature. This will result in the superposition of a series of first order transitions, which as a bulk average will resemble a broader "second order" like transition. This effect was observed through the use of neutron diffraction techniques only on the spin flip transition, but as the sample composition is not modified by passing to the higher temperature paramagnetic to TSDW the same effects will apply. Hence it is concluded that the structure observed in the normally smooth C_{44} data can be explained by local regions of differing silicon concentration passing through the transition at different temperatures.

There are several "τ domain" structures possible (as described in chapter one), on passing into the TSDW phase and it is valuable to know if a certain structure is reproducible on cycling into the LSDW phase and back again. This was tested by taking a topograph in the middle of the spin flip transition at 102.5K on the annealed sample as seen in figure 4.6a. The sample was then cycled through the transition and reset to 102.5K before repeating this previously recorded result (figure 4.6b). These topographs

clearly show that these regions are repeatable after thermal cycling. The fact that after thermal cycling, the sample goes from being a TSDW to a LSDW in the same region along the same τ direction, supports the fact that in the transition it is the magnetic moment of the sample that changes direction and not the τ value of the domains.

The size of the observed domains is also of particular interest, as there has been a great deal of controversy in the past as to the mechanism of domain formation in pure chromium. One of the models, the thermal excitation model, predicted an average domain size of the order of $10^{-16}cm^3$ (Munday & Street 1971, Steinitz et al 1977). This is clearly not the case, unless these domains are bunched very closely, so that what is actually recorded are many intense domains all grouped in specific regions of the sample. This is unlikely to occur because of the large amount of energy required to form the domain walls. The domains imaged were roughly $10^{-3}m$ in dimension, which was concurrent with the domain size observed by Ando & Hosoya (1978) on pure chromium.

The effects seen in this chromium silicon system describe a phase coexistence which is driven primarily by a chemical composition gradient. It is this effect which is seen on the volume averaged techniques of neutron diffraction and the measurement of the elastic constant by ultrasonic methods. However the actual domain shapes imaged by neutron diffraction topography are clearly dependent on other factors. Firstly the sample is divided amongst several different τ domains (of which only one has been imaged in each topograph). Also the sample contains a subgrain which is misoriented from the rest of the lattice of ~ 9 minutes of arc. This subgrain clearly contains a higher than average silicon concentration because as the sample passes through the transition the diffracted intensity resides on the subgrain.

4.3. Ferromagnetic and Helimagnetic phase coexistence in terbium.

There are two different approaches to achieving phase coexistence on the first order transition from a ferromagnetic to a helimagnetic phase in terbium. Simply

decreasing the temperature from within the helimagnetic phase (221K < T < 229K), in zero field conditions will drive the sample into the ferromagnetic phase ("temperature driven transition"). Alternatively, by applying a b axis magnetic field the sample will also be driven into the ferromagnetic phase for a field bigger than the critical field H_C (figure 1.4). This is the field driven transition. These two different paths lead to significant differences in the orientation of the ferromagnetic-helimagnetic phase boundary of a given sample, as will be demonstrated in the following sections.

4.3a. Phase coexistence in a b axis field.

Figure 4.14 shows the integrated intensity and corresponding neutron diffraction topographs of the 002-τ reflection as a function of the magnetic field at a constant temperature of 223K. The topographs show that during the phase coexistence, the ferromagnetic phase (the non diffracting regions of the image) forms whisker like regions within the helimagnetic phase with their interfaces being parallel to the externally applied b axis field and the magnetisation direction. On increasing the applied field above 0.07 Tesla two larger ferromagnetic regions are visible at the extremities of the sample. These regions increase in size on augmenting the applied field.

4.3b Discussion.

At 223K the helimagnetic phase occupies the whole of the sample in zero field, but can be driven wholly ferromagnetic on applying b axis fields larger than 0.015T. Phase coexistence occurs between these two extreme conditions over a range of applied field which corresponds to a constant internal field (which is equal to the critical field as previously described in chapter one). This range of phase coexistence has the same origin as that of the zero valued internal field which occurs during the magnetisation of a ferromagnet (where the internal field is equal to the difference of applied and demagnetising fields). In the particular case of helimagnetic and ferromagnetic phase

Figure 4.14: The variation of the peak diffracted intensity of the 002-τ magnetic satellite as a function of the applied b axis magnetic field

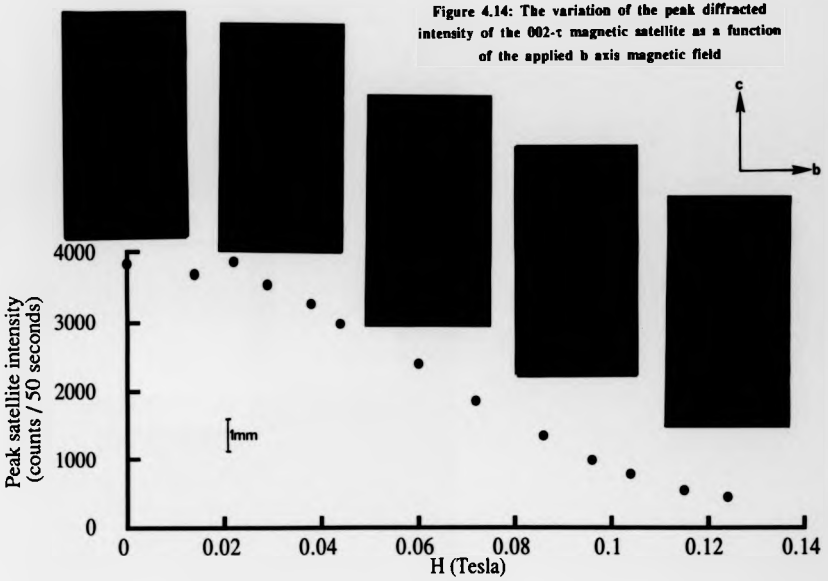

coexistence the internal field only departs from the critical value after the complete disappearance of the interfaces.

The above treatment of the helimagnetic-ferromagnetic phase coexistence can only be considered as a first order approximation due to the absence of energy terms describing any magnetocrystalline, elastic, or phase boundary considerations. However, this approximation appears to be valid as in a recent work by Bar'yakhtar et al. (1986), the elastic energy term was also considered and this gave very similar results to those predicted above.

The topographs of figure 4.14 show the sample divided into a series of striped regions of ferromagnetic and helimagnetic phase, which lie parallel to the direction of application of the applied field. This structure can be described in terms of the magnetostatic energy term which arises from the formation of magnetic free poles at the boundary between as the helimagnetic phase (which shows no net magnetisation), and the ferromagnetic phase. The magnetostatic problem arising from such a phase coexistence is similar to that of a saturated ferromagnetic sample, but with the added complication that the boundary conditions are not necessarily fixed to the physical limit of the sample. Moreover, the phase boundary is allowed to change shape, direction and even traverse the crystal volume.

An analogy to this system in the applied field case is that of the boundary between a ferrofluid and air when under the influence of an externally applied field, as described by Cowley & Rosenweig (1967). Under the application of a field, the ferrofluid (analogous to the ferromagnetic phase) will form a needle like structure on its surface where the ferrofluid penetrates the non magnetic phase (air) along the field direction, in order to reduce the demagnetising factor produced by the free poles

In this case the magnetostatic energy term will be in competition with both the interface energy and the the effects of gravity. These last two energy terms restricts the

penetration of the ferrofluid phase into the non magnetic phase, so that the phase coexistence never reaches the advanced 'column state' as predicted from the magnetostatic energy considerations and as observed in the helimagnetic-ferromagnetic phase coexistence of terbium.

From the above considerations a first approximation of the phase coexistence would suggest that the sample be uniformly divided into stripes of alternate ferromagnetic and helimagnetic phases. On augmenting the applied field the width of these ferromagnetic "whiskers" would then be expected to gradually increase until all the helimagnetic regions had been expelled from the sample. However, in addition to these regular stripes, on increasing the field two larger, predominantly ferromagnetic regions become visible at either end of the crystal. The central region of the crystal remains finely divided between both the ferromagnetic and helimagnetic phases.

The variation in the width of the ferromagnetic regions of during phase coexistence can be related to the shape of the sample. Following the calculations of the demagnetising field for a rectangular prism shaped sample (Joseph & Schlomann (1965)) the demagnetising field was calculated for the ferromagnetic regions imaged in figure 4.14. These demagnetising field values were then used to provide a value for the internal field from equation (8).

As a first approximation the parallel domain structure illustrated in figure 4.15a was used to calculate the variation of the internal field across the sample. This simple phase configuration was found to satisfy the criterion of a nearly constant internal field along the c axis, but the internal field in the b axis was observed to decrease at the sample edges. Improved results were produced when considering needle shaped ferromagnetic regions as were actually observed on the topographs of figure 4.14.

Within the needle tips the magnetic moments were initially assumed to be parallel to the applied b axis field. However, since the ferromagnetic regions have a needle shape

Figure 4.15: A schematic representation of the phase coexistence in the terbium platelet for a) a simple parallel band structure and b) for ferromagnetic regions with needle shaped tips in which the magnetic moments are rotated towards the central position.

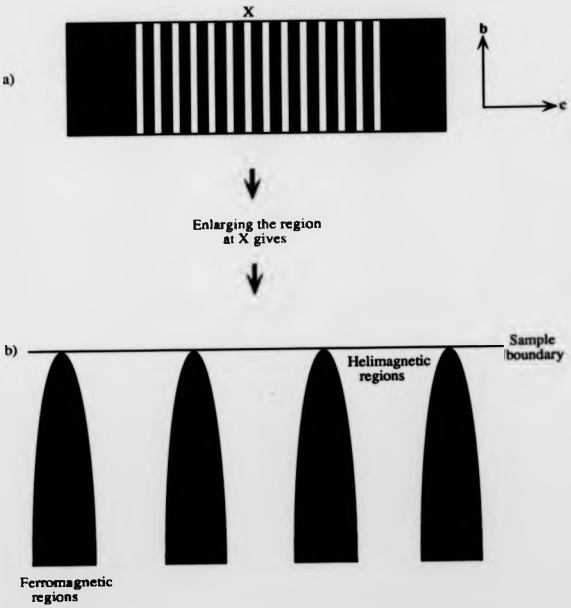

(figure 4.15b), the orientation of the magnetic moments along the b axis will produce a large magnetostatic energy component. By rotating the magnetic moments towards the tips of the ferromagnetic needles (represented by the arrows in figure 4.15b), the magnetostatic energy term can be reduced. The reduction of the magnetostatic energy is opposed by a subsequent increase in the anisotropy energy since the moments are no longer aligned along the applied field direction. However for small angular rotations the magnitude of the anisotropy term will be smaller than that of the magnetostatic one. The demagnetising field of the sample calculated with this refined phase coexistence structure leads to a nearly constant internal field along both c and b axes.

The topographs taken of the terbium sample in an externally applied b axis field were investigated using the Macintosh "Optilab" image digitisation and treatment system. In this system the domain structure is transformed into a digitised two dimensional array of intensities in which the background noise can be reduced by applying a low pass filter to the Fourier transform of the original image. The topograph taken at 0.04 Tesla illustrated in figure 4.14 was treated in the above manner with the digitised topograph (figure 4.16a) being intensity scanned along the c axis, as a function of their b axis position. The helimagnetic phase was detected as a series of intensity peaks across the length of the sample, as shown in figure 4.16b for the central region of the sample from A to B and in figure 4.16c at the edge of the sample from C to D. Whilst the peak to peak amplitude of the detected intensity from the alternating phases was seen to diminish on moving to the sample edge along the b axis, there was no noticeable increase in the frequency of the intensity peaks. The reduction of contrast near the edge of the sample confirms the assumption of section 4.3b that the ferromagnetic regions are reduced at the sample edges.

The absence of any change in the frequency of these peaks indicates that the helimagnetic regions are not interspaced at the sample edges by regions of ferromagnetic phase in an analogous way to the "branched" domains in the ferromagnetic case (Kaczer

(figure 4.15b), the orientation of the magnetic moments along the b axis will produce a large magnetostatic energy component. By rotating the magnetic moments towards the tips of the ferromagnetic needles (represented by the arrows in figure 4.15b), the magnetostatic energy term can be reduced. The reduction of the magnetostatic energy is opposed by a subsequent increase in the anisotropy energy since the moments are no longer aligned along the applied field direction. However for small angular rotations the magnitude of the anisotropy term will be smaller than that of the magnetostatic one. The demagnetising field of the sample calculated with this refined phase coexistence structure leads to a nearly constant internal field along both c and b axes.

The topographs taken of the terbium sample in an externally applied b axis field were investigated using the Macintosh "Optilab" image digitisation and treatment system. In this system the domain structure is transformed into a digitised two dimensional array of intensities in which the background noise can be reduced by applying a low pass filter to the Fourier transform of the original image. The topograph taken at 0.04 Tesla illustrated in figure 4.14 was treated in the above manner with the digitised topograph (figure 4.16a) being intensity scanned along the c axis, as a function of their b axis position. The helimagnetic phase was detected as a series of intensity peaks across the length of the sample, as shown in figure 4.16b for the central region of the sample from A to B and in figure 4.16c at the edge of the sample from C to D. Whilst the peak to peak amplitude of the detected intensity from the alternating phases was seen to diminish on moving to the sample edge along the b axis, there was no noticeable increase in the frequency of the intensity peaks. The reduction of contrast near the edge of the sample confirms the assumption of section 4.3b that the ferromagnetic regions are reduced at the sample edges.

The absence of any change in the frequency of these peaks indicates that the helimagnetic regions are not interspaced at the sample edges by regions of ferromagnetic phase in an analogous way to the "branched" domains in the ferromagnetic case (Kaczer

Figure 4.16. Digitised neutron topographic data of the field driven phase coexistence in the terbium platelet sample: a) The digitised topograph b) an intensity scan of the intensity recorded on the topograph as a function of position alond the line AB and c) a similar intensity scan at the edge of the sample along the line CD.

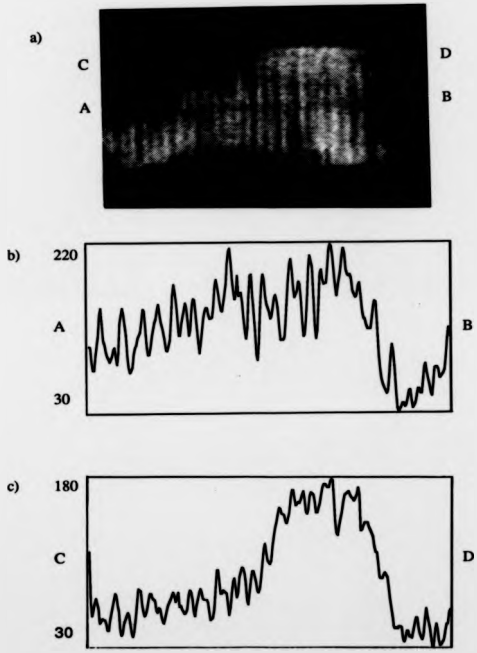

1964) and as proposed by Podkorytov & Yablonskii (1983) in the metamagnetic transition case. There is also the possibility that the size of the branched regions are below the spatial resolution (60 μm), of our observation technique.

4.3c Phase coexistence in zero field conditions.

The temperature driven helimagnetic to ferromagnetic phase transition occurs at a specific temperature and not over a range of temperatures, in contrast with the case of applying an external field. Consequently, it is very difficult to maintain a constant phase coexistence over a sufficiently long time period to perform a topograph (typical exposure times being of the order of 15 hours for the 002 magnetic reflections of terbium). However several topographs were recorded, as a result of very accurate temperature control and a probable slight temperature gradient across the sample.

Figure 4.17 shows the diffracted intensity of the 002-τ magnetic satellite recorded on a series of neutron topographs as a function of decreasing temperature. The phase boundaries are no longer parallel to the b axis but instead take a more random shape, with the centre of the sample remaining in the helimagnetic phase at the lowest temperature. The boundaries of the ferromagnetic phase do however show traces of the previously mentioned "whisker like" alignment, parallel to the b axis as in the field driven case of section 4.3c.

4.3d Discussion.

The "temperature driven phase coexistence" is not expected to exist over range of temperatures. Nevertheless, this type of phase coexistence was observed in this investigation (figure 4.17). The ability to stabilise the phase boundary probably results from a combination of a temperature gradient across the sample and the pinning of the phase boundary on crystal defects.

Figure 4.17. The variation of the diffracted intensity of the 002-τ magnetic reflection recorded on neutron topographs as a function of temperature in zero applied field.

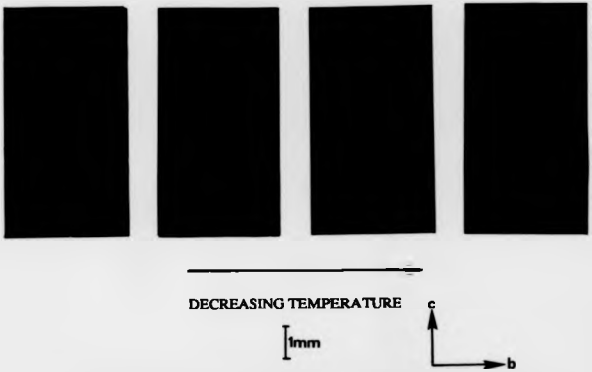

Figure 4.18. The variation of the diffracted intensity of the 002-τ magnetic reflection recorded on neutron topographs as a function of temperature in a 0.004T b axis applied field.

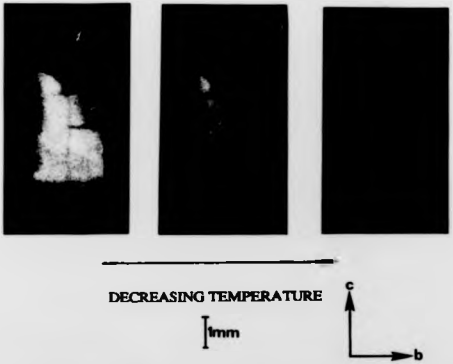

In the absence of an externally applied field the domains of the ferromagnetic phase will reduce the magnetostatic energy term so that the observed interface orientations can be understood as resulting from the competition between this term, the phase boundary energy, and elastic compatibility conditions. The elastic energy term originates from the elastic deformation of the crystalline lattice as a result of magnetostrictive effects (the difference in lattice parameters associated with each magnetic phase) at the phase transition. The increase in the elastic energy is principally dependent on the orientation of the phase boundary and clearly becomes more influential in zero field conditions, when the magnetostatic energy term is reduced by the domains.

In the particular case of terbium the lattice parameters are known to reduce along the **a** and **b** axes and increase along the **c** axis on passing into the ferromagnetic phase. Thus following the work by Nye (1957) a direction of minimum elastic deformation should be contained within the **b**, **c** plane (the surface of the platelet used in this investigation). Unfortunately, this angle cannot be calculated as the critical strains for the three crystallographic axes have not been measured at the Curie point in terbium. However, the topographic data (figure 4.17) indicates that the modulated phase boundary is truncated at an average angle of approximately 49° with respect to the **c** axis. If we assume that this angle corresponds to a minimum elastic deformation direction, then this could lead to the measurement of the relative **b** axis to **c** axis strain at the phase boundary, which would be − 1.1.

In zero field conditions the phase boundary orientation is dominated by the elastic compatibility conditions which produce a overall direction to the boundary. Local variations from this value are believed to be the result of either crystalline defects (which allow a reduction of the elastic energy term) or magnetic impurities (which produce an enhanced magnetostatic energy contribution).

4.3e Temperature driven phase coexistence under a 0.004T b axis field.

Figure 4.18. shows the diffracted intensity of the 002-τ magnetic reflection recorded on a series of neutron topographs in an externally applied 0.004 T b axis field as a function of decreasing temperature.

4.3f Discussion.

The applied field neutron topographic data of figure 4.18 only show minor alterations from those previously seen in the zero field topographs taken on the same reflection (figure 4.17). The elastic energy term still remains dominant, with the phase boundary being angled at approximately 49° to the c axis. A series of small spikes can be seen penetrating up the b axis, which is the direction of application of the small (0.004T) b axis field. These spikes are produced to reduce the magnetostatic energy contribution of the ferromagnetic phase which becomes more influencial on the application of on external magnetic field due to the production of magnetic free poles at the interface. It has been shown by Sandonis (1991) that the energy of the system (as a function of the length of these spiked regions (h)), is a function of a parameter ε which is given by,

$$\varepsilon = \frac{\mu_0 M_{AV}^2}{(\rho_{ANISO} + \rho_{ELAST})} \qquad (72)$$

where M_{AV} is the average magnetisation of the sample and ρ_{ANISO} and ρ_{ELAST} represent the energy densities at the interface for the anisotropy and elastic constraints. The extremum of the energy for a given ε lies on a curve as illustrated in figure 4.19. The curve is plotted as a function of the ratios of L/t and h/t , where L represents the amount of the sample in the ferromagnetic phase and t the sample thickness. The calculations of Sandonis (1991) have shown that increasing either the applied field or the thickness of the sample will have the effect of increasing the length of the spiked ferromagnetic regions.

Figure 4.19: The extremum energy condition for ferromagnetic-helimagnetic phase coexistence as a function of the ferromagnetic volume of the sample and the dimensions of the spikes on the interface for a series of ε parameter values.

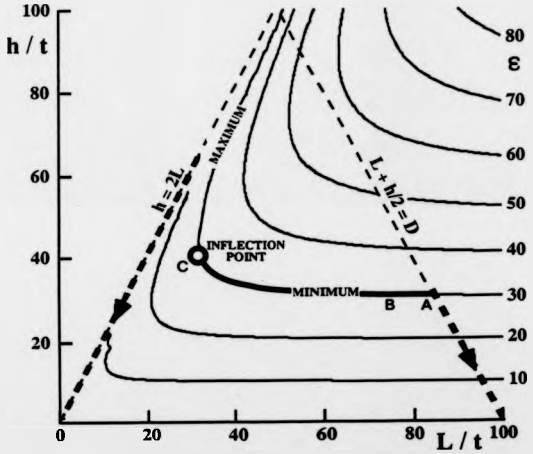

The assumptions of these calculations are that the anisotropy and elastic energy densities are restricted to the interface region and are proportional to the magnitude of the zig-zag structure (h). Within this model it is the elastic term which defines the general orientation of the phase boundary and the modulated structure is then imposed on this orientation by the magnetostatic term.

The ε parameter also applies to the applied field driven transition of terbium (section 4.3), but with the difference that the magnetostatic term is even more dominant than in the above case. It is for this reason that a) the spikes are so long that they span the whole of the sample and b) the phase coexistence can be explained as a first approximation through the constant internal field approach as seen in section 4.3b.

4.4 Ferromagnetic and helimagnetic phase coexistence in MnP.

From the phase diagram of manganese phosphide (illustrated in figure 1.12b), the helimagnetic phase can be entered either from the ferromagnetic phase or from the applied b axis field 'fan' phase. This particular study will demonstrate the passage from the ferromagnetic phase to the helimagnetic phase as a function of temperature in zero applied field and the reverse transition under the effects of moderate (< 0.3T) c axis field.

4.4a Phase coexistence in zero field.

The two polarised neutron diffraction topographs of figure 4.20 show the diffracted intensity from the same (a,c) MnP sample under identical phase coexistence conditions on a) the 200 nuclear reflection and b) the 2+τ,00 magnetic reflection. The intensity recorded on the 200 nuclear reflection corresponds to the summation of the nuclear reflectivity of the whole sample and the magnetic reflectivity which is associated to the regions of the sample which are in the ferromagnetic phase. The intensity detected on the 2+τ,00 satellite reflection only represents the magnetic reflectivity of the helimagnetic regions of the sample. The topograph illustrated in figure 4.20b shows the

Figure 4.20. Two neutron diffraction topographs taken on an a/c MnP platelet sample on a) the 200 nuclear reflection and b) the 2+τ 00 magnetic satellite reflection. Figure 4.20c illustrates the orientation of the sample and its thermal contact point to the cryostat for these particular neutron topographs.

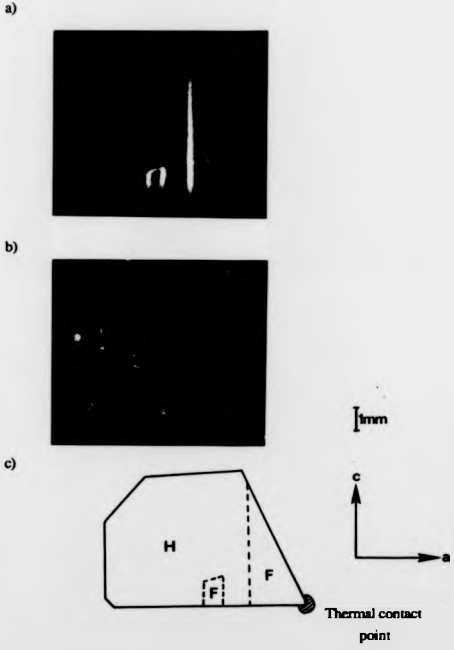

photographic detection of this intensity, where vertical striations in the helimagnetic phase represent the fine "F" type chirality domain structure of this sample. Due to the large exposure time of this topograph (18 hours) several aluminium powder diffraction spots (white speckles) can be seen on this topograph. These spots originate from the casing of the cryostat tail. Figure 4.20c illustrates the orientation of the sample and its thermal contact point to the cryostat for these neutron diffraction topographs.

Figure 4.21 shows a series of zero field white beam synchrotron topographs as a function of the sample temperature. The variation of the diffracted intensity corresponds to a) an initial position which is wholly within the helimagnetic phase to g), a final position where nearly all of the sample is in the ferromagnetic phase after enhancing the temperature by 2.6K. Figure 4.21h illustrates the samples orientation and thermal contact point for these topographs. In the synchrotron topographs the high intensity images represent either crystalline defects or the phase boundary between the helimagnetic and ferromagnetic phases.

4.4b Discussion.

From the zero field topographs of figures 4.20 & 4.21, the helimagnetic-ferromagnetic phase boundary lies predominantly parallel to the c axis, which is the easy magnetic axis of manganese phosphide. In the zero applied field case the ε parameter will be small, but the small magnetostatic energy contribution (which results from the domain structure of the ferromagnetic phase in the absence of an applied field) will favour an orientation parallel to the easy, c axis. However it is the elastic compatibility and interface energies which should be dominant in this particular case.

From the topograph of the 200 nuclear reflection illustrated in figure 4.20a all the phase boundaries exhibit an increased diffracted intensity. This intensity increase can be understood through a gradient of distortion at the phase boundary where the lattice spacing mismatch (of the helimagnetic and ferromagnetic phases) produces a locally

Figure 4.21. A series of zero field synchrotron radiation topographs as a function of increasing sample temperature from a) in the helimagnetic phase to g) where the sample is almost totally in the ferromagnetic phase. h) illustrates the sample orientation

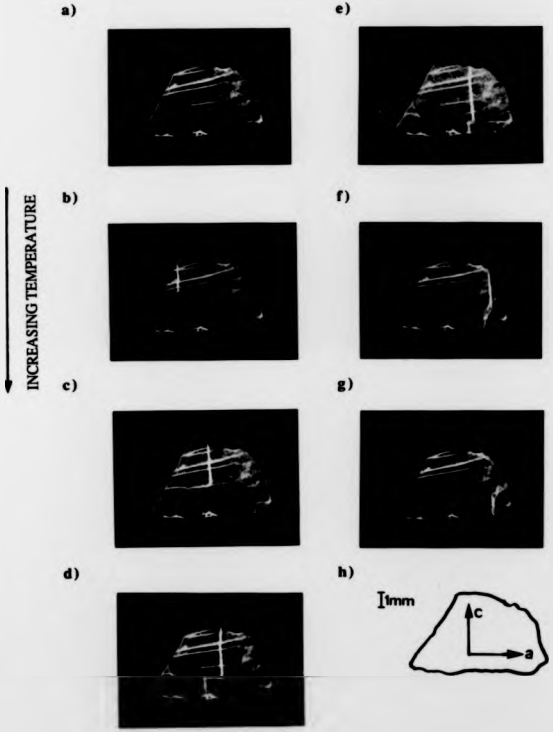

deformed region. This region is imaged as an increase in diffracted intensity due to the local reduction of extinction effects at the boundary. The deformed region around the phase boundary thus produces an increase in the elastic energy term of the ϵ parameter.

The minimisation of this elastic energy is achieved by matching the lattice parameters in the helimagnetic and ferromagnetic phases at the phase boundary (Nye 1957). From the linear thermal expansion measurements shown in figure 1.13 (taken along the three crystalline axes of manganese phosphide by Okamoto et al. 1968), it is clear that a direction of minimum deformation can be found in both the (a,b) and (b,c) planes of MnP. It should be noted that the total elastic energy of the phase boundary not only depends on its orientation but also on the surface area of the boundary within the sample. This area consideration would imply that an (a,b) orientation of the phase boundary would be favourable and this appears to be in agreement with the increased width seen on the vertical phase boundaries of figure 4.20a.

The angle (α) which the phase boundary makes with the a axis on minimising the elastic energy of the system was calculated (following the work of Nye 1957) to be of the order of 32 ± 2 degrees. This value assumes that the c axis magnetostriction does not affect the orientation of the phase boundaries in the (a,b) plane (as indicated from their vertical orientation on the topographs of figure 4.20 & 4.21). As the boundary imaged in these topographs represents the integration of the boundary position across the 178μm thickness of the crystal, the above value of α can be verified by a simple geometrical calculation from the nuclear 200 topograph of figure 4.20a. This method produces an a value of 30 ± 5 degrees which is in agreement with the orientation of minimum deformation ($\alpha \approx 32$ degrees), as given above.

The topographs of figure 4.20 shows an isolated region of ferromagnetic phase which has a phase boundary at approximately 25° to the a axis in the (a,c) plane. It is clear from figure 1.13 that the (a,c) plane does not contain a direction of zero deformation (as $\Delta a/a$ and $\Delta c/c$ are of the same sign) and hence the orientation of this phase boundary

can not be explained by the reduction of elastic energy as described above. A simpler explanation of this phase boundary orientation can be found from the surface defects of the sample (imaged as a series of faint lines tracing horizontally across the synchrotron topographs of figure 4.21).

Close inspection of figures 4.21b & 4.21c show that the orientation of the phase boundary of the isolated region of the ferromagnetic phase in figure 4.20a can be directly attributed to the orientation of these defects. Whilst this is contrary to the magnetostatic energy term, it will reduce the elastic energy considerations due to the improved lattice matching present at the defect. The orientation of the phase boundary along defect lines is a very common feature of the topographs of figure 4.21, where all the boundaries are either parallel to or superimposed on these surface lines.

The isolated region of ferromagnetic phase imaged in figure 4.20a shows a similar configuration to the synchrotron topograph of figure 4.21d, where on increasing the temperature in zero field, the ferromagnetic phase nucleates on the bottom surface of the sample. The ferromagnetic phase is thought to be stabilised at this position as result of a local region of stress induced during the sample preparation. It has been shown (Hirahara et al. 1968) that applied stresses have an effect on the temperature at which the helimagnetic to ferromagnetic transition occurs in manganese phosphide. The local increased intensity detected on the synchrotron topographs at this point is a strong indication that the sample is of poorer crystalline quality.

The temperature variation of the synchrotron topographs of figure 4.21 illustrate the passage of the phase boundary across the sample volume. The phase boundary can either be described through an orientation of approximately 32 degrees to the a axis and parallel to the easy c axis or parallel to a surface defect everywhere except in the bottom left hand corner of these topographs. In this part of the sample there are fewer defects and as such the phase boundary orientation is principally governed by the elastic considerations of all three lattice planes. In this case the boundary is much wider and its

image weaker than observed for the vertical boundaries indicating they are actually along directions of minimum strain.

4.4c Phase coexistence in MnP in an applied 0.015T c axis magnetic field.

Figure 4.22 illustrates a series of white beam synchrotron topographs using the same (a,c) sample as in the zero field topographs of figure 4.21. The topographs were taken as a function of increasing temperature under the influence of a 0.015T c axis applied field.

4.4d Discussion.

The application of a moderate c axis field (figure 4.22) has a spectacular effect on the phase boundary orientation of the temperature driven phase coexistence of MnP. As in the case of terbium the application of a magnetic field increases the magnetostatic energy term and hence the ε parameter (as described in section 4.3f). The preferred orientation of the phase boundary will thus be along the applied field parallel to the easy c axis. However, the effect of the horizontal surface defects on this orientation is still very similar to the zero field case (compare figure 4.21c & figure 4.22d).

On increasing the temperature the ferromagnetic phase propagates into the helimagnetic phase as a series of extended spikes parallel to the applied field direction thus minimising the magnetostatic energy (figures 4.22a & 4.22b). Augmenting the temperature still further (figure 4.22c) produces two regions of ferromagnetic phase in the top left hand corner of the topograph. The energy considerations for this sample are such that as soon as a ferromagnetic volume (defined as being more than a series of individual spikes) exists then the modulated zig-zag structure (which is superimposed over the non vertical phase boundary) is immediately driven to the $L+h/2=D$ limit as shown at A on figure 4.19. Increasing the temperature can now only increase ferromagnetic volume (L) at the cost of reducing the magnitude of the ferromagnetic spikes (h). It should be noted

Figure 4.22. The intensity variation during phase coexistence as recorded on a series of white beam synchrotron radiation topographs on increasing the sample temperature from the helimagnetic phase whilst under the influence of a 0.015 Tesla c axis field.

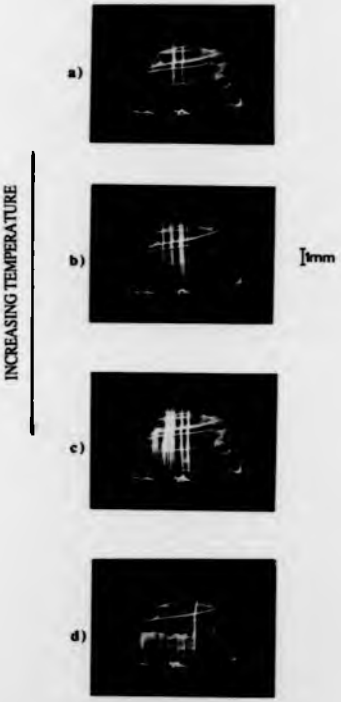

that although this type of transition is thought to occur smoothly (as illustrated in the schematic diagram of figure 1.6) it will in fact follow a more erratic, stepped path due to the pinning of the phase boundary to the surface defects of the sample. This effect was inferred from the passage between figure 4.22c & 4.22d and is thought to be analogous the Barkhausen effect of domain magnetism.

On reversing the transition (entering the helimagnetic phase from the ferromagnetic phase) the pattern can be expected to be slightly different due to the initial nucleation of the helimagnetic phase. Once in phase coexistence (B on figure 4.19) and reducing the ferromagnetic volume of the sample (for a given ϵ parameter), the size of the zig-zag structure will slowly increase until the extremum of the system is no longer a minimum in the energy of the system (point C). At this point the system will pass to the second limiting value h=2L, as clearly the energy cannot become a maximum. This situation corresponds to an alternating band structure as seen in the neutron topographs of terbium in section 4.3a. The passage from C to the h=2L limit in figure 4.19 is not clear. However, it is most likely to occur through a divergence of the magnitude of the spikes and hence an increase in h/t on reducing L/t.

In all of the results reported in this chapter the sample has been attached to the cryostat in such a way as to provide a minimum temperature gradient across the sample without risking inducing any strain into the samples. However even with this goal in mind it is clear from the topographs of the zero field phase coexistence in terbium (figure 4.17) that a small temperature gradient was in fact present. In the following chapter a series of results will be presented in which a special attempt was made to achieve (and control), a temperature gradient across the sample volume.

CHAPTER FIVE

PHASE COEXISTENCE (II)

(UNDER A TEMPERATURE GRADIENT).

5.1 Introduction.

The stabilisation of the temperature driven phase coexistence in the first order phase transition of terbium described in chapter four, was achieved partially by the unavoidable application of a small temperature gradient across the sample volume. The temperature gradient occurred because the sample was fixed to the cold source at a single point (in order to reduce sample stress), as is common with all high quality single crystal topography samples. The crystal was then surrounded by aluminium foil in contact with the cold finger but even so, this was not enough to avoid a slightly non uniform temperature distribution throughout the crystal.

In the cases where a temperature difference is imposed across the crystal it is often possible to analyse this gradient as a function of the direction of phase boundary shift through the phase coexistence (though this was not the case in terbium). It should be noted that in the case of synchrotron topography the spatial temperature variation of the sample can be complicated by the irradiative sample heating of the incident photons as previously observed by Baruchel et al. (1988).

Whilst a non uniform sample temperature may not appear to provide perfect conditions for the analysis of phase coexistence, by enhancing the temperature gradient it is possible to produce two very useful side effects. The first is the ability to stabilise some first order transitions in which the phase coexistence occurs over a very small temperature range. By applying a temperature gradient greater than the "intrinsic" temperature range of

coexistence (which will be zero in the absence of an applied magnetic field), the sample will be divided between the two phases. Secondly by introducing thermal energy at a localised point on the sample surface the phase boundary can be directionally driven through the sample volume. The phase boundary orientation will then be dependent on the thermal contact position and the resulting heat flow.

In this chapter the application of a temperature gradient will be used to give a more controlled study (through the ability to provide a simultaneous local heating and directional cooling at the sample), of the helimagnetic-ferromagnetic phase coexistence in manganese phosphide by taking advantage of the two effects described above. These investigations were undertaken with two aims a) to study the influence of the defect structure of an (a,b) MnP sample on the phase boundary orientation when sweeping the phase transition across the sample volume and b) to observe the phase coexistence of three magnetic phases (the triple point) on the same compound.

5.2 The effect of a temperature gradient in neutron topography on MnP.

A high quality (a,b) manganese phosphide, single crystal, sample was mounted on the sample holder (described in chapter three), as shown in figure 5.1. This arrangement allowed the sample to be simultaneously cooled at its fixation point and heated through the aluminium thermal contact at its base. The sample was set to diffract from the 2+τ 00 magnetic satellite and the detected peak intensity is plotted as a function of the temperature (measured at the tip of the displex cold finger), as illustrated in figure 5.2. It should be noted that these reported temperatures are arbitrary and have only been given to provide a comparison of their relative values. Even so the temperature gradient across the sample can be estimated from these relative values to be approximately 0.4K. It is also clear that the interface position (as seen in the following topographs) will correspond to the metamagnetic transition temperature (T_M) between the helimagnetic and ferromagnetic phases, which in zero field has a value of ≈ 47K.

Figure 5.1: A schematic representation of the orientation and mounting of the (a,b) manganese phosphide sample.

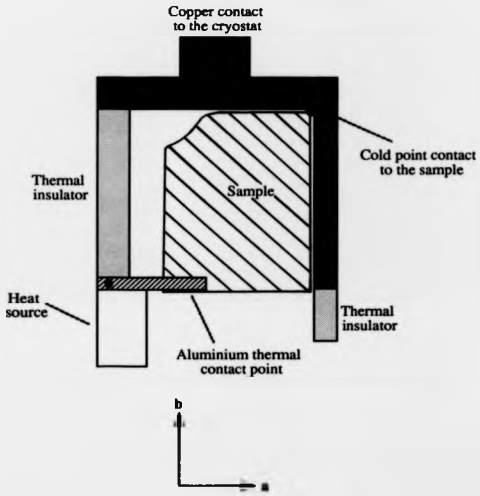

Figure 5.2: The temperature variation (as measured at the cold head), of the peak intensity of the 002+τ satellite reflection of the (a,b) MnP sample.

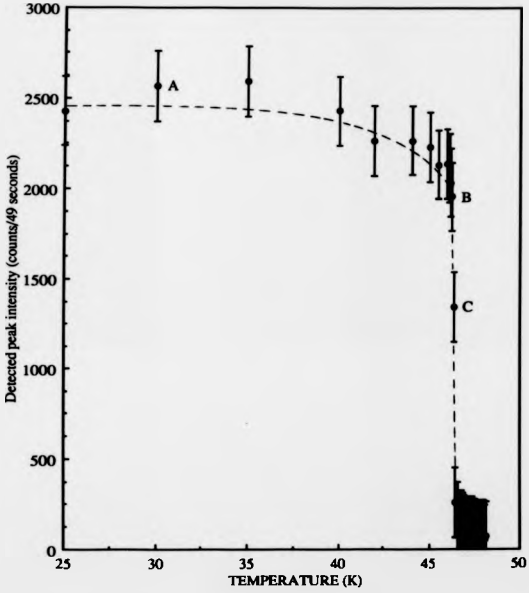

The phase coexistence at positions A, B and C on the phase transition were then imaged in a series of polarised neutron diffraction topographs in a 1.65 Å incident beam. Figure 5.3a shows the topographs of the 2+τ 00, magnetic satellite with the neutron polarisation in both senses (<+> and <->, with the guide field being horizontal and not far from parallel to the a axis). The recorded cold head temperatures at which these topographs were taken were 30 ± 0.2K as indicated at A in figure 5.2. This cold head temperature is approximately 16K below the previously observed temperature transition (T_M = 47K) of Komatsubara et al. (1970). Even after allowing for the temperature difference between the sample and the cold head (which is at most 2K), the sample is still well below T_M and as such would be expected to be wholly helimagnetic. However, a close inspection of the classical "F" type chirality domains indicates that there is a small region of the sample which diffracts from neither of the two helical domain types. From a consideration of the magnetic phase diagrams of manganese phosphide (figure 1.11) the non-diffracting region can only be an isolated ferromagnetic cluster coexisting in the helimagnetic phase.

On increasing the cold head temperature (46.2K) the ferromagnetic phase nucleates in the warmer, lower half of the sample as illustrated in figure 5.3b, which was taken at B on figure 5.2. The first two topographs correspond to the 2+τ 00 magnetic satellite in left <+> and right <-> neutron polarisation states just as in the topographs of figure 5.3a. The third topograph was taken on the 200 nuclear peak, where the ferromagnetic phase (the more illuminated background region) is superimposed over the defect structure of the crystal lattice. The previously observed ferromagnetic cluster is now accompanied by two similar non diffracting regions in the helimagnetic phase, as seen on the two "magnetic" topographs of figure 5.3b. All three of these regions lie along the magnetically hard a axis and perpendicular to the helimagnetic "F" domains .

Increasing the temperature further still drives the phase boundary higher up the sample until the above mentioned isolated ferromagnetic regions are engulfed into the

Figure 5.3: A series of neutron topographs taken in both polarisation states on the 2+τ 00 magnetic satellite at a) 30.0K and with additional topographs of the 200 nuclear reflection at b) and c) for temperatures of 46.2K and 46.3K respectively.

a) T = 30.0K

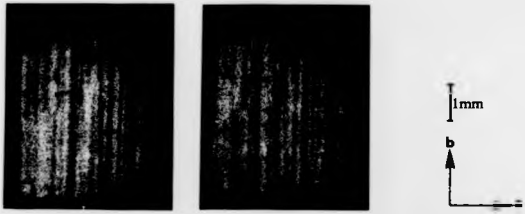

2+τ 00 <+> 2+τ 00 <->

b) T = 46.2K

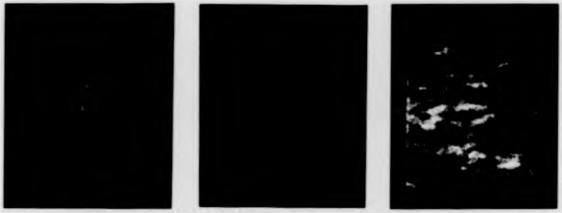

2+τ 00 <+> 2+τ 00 <-> 200

c) T = 46.3K

2+τ 00 <+> 2+τ 00 <-> 200

ferromagnetic phase. Figure 5.3c shows this situation on three topographs which were recorded on the same three diffraction peaks as in figure 5.3b. The enhancement of the ferromagnetic phase through the vertical movement of the phase boundary indicates that the sample is actually under the expected temperature gradient, with the coldest part of the sample being the thermal contact point to the head of the cryostat.

These topographs also indicate that isolated regions of the helimagnetic phase remain in the non-diffracting ferromagnetic matrix. These helimagnetic regions take a more random shape than their ferromagnetic counterparts, but just as in the bulk helimagnetic phase region they are divided into "F" type chirality domains.

A schematic representation of the regions of the sample which show increased crystalline distortion (imaged as high intensity regions on the 200 nuclear Bragg reflections of figure 5.3b & 5.3c) is given in figure 5.4a. The positions of the two phase boundaries seen on the magnetic reflection topographs of figures 5.3b & 5.3c are illustrated on a schematic representation of the sample area in figure 5.4b. Figure 5.4c shows a photograph of the surface defects of the face of the (a,b) manganese phosphide sample. The final image of this series (figure 5.4d) is a synchrotron radiation topograph taken on the 140 reflection at an incident wavelength of 0.7Å on the same (a,b) manganese phosphide platelet. The regions of high deformation are visible as the random regions of increased intensity and are concurrent with those present on the schematic diagram of the neutron topographs and the defects seen on the surface photograph of this figure.

From figure 5.4 a clear correlation can be seen between the defect structure and the boundary of the ferromagnetic phase. This is also the case for the isolated ferromagnetic regions which nucleated in the helimagnetic phase on increasing the average sample temperature. Moreover the remanent regions of the helimagnetic phase seen on the magnetic topographs of figure 5.3c also rest at positions of high crystal distortion as indicated from the nuclear topograph in this figure. All of the topographs of

Figure 5.4: The defect structure of the manganese phosphide (a,b) sample as shown in a) a schematic representation of the intensity detected on the 200 nuclear reflection using neutron diffraction topography, c) a photograph of the sample surface and d) a synchrotron radiation topograph taken on the 140 reflection. Figure 5.4b describes the two phase boundary positions observed in Figure 5.3b & 5.3c as measured at B and C on figure 5.2.

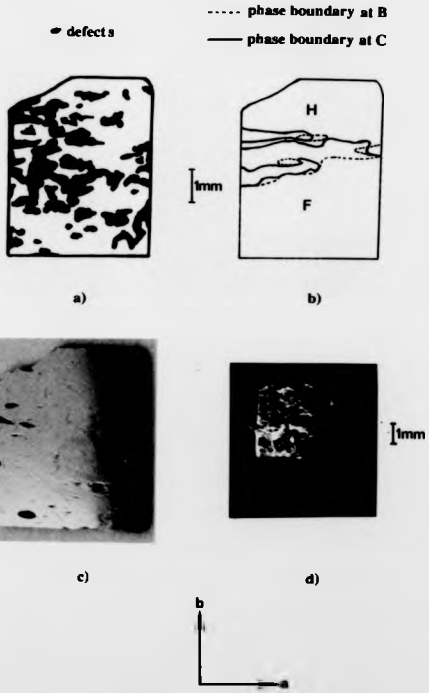

figure 5.3 were produced from a neutron beam which was polarised nearly along the horizontal a axis (to satisfy the condition for imaging chirality domains).

For the topographs illustrated in figure 5.5 the horizontal guide field was aligned in the vertical plane (down the b axis of the sample) along with an additional applied field of 0.186 Tesla in the same direction. Figure 5.5 shows two topographs taken at the same stage of phase coexistence as previously imaged in figure 5.3b & 5.3c. From the topograph taken on the $2+\tau$ 00 satellite reflection (figure 5.5a), the ferromagnetic phase can be seen to nucleate well into the helimagnetic phase, but with the application of a field the majority of the remanent helimagnetic phase has been lost from the ferromagnetic region at the base of the sample. On the nuclear topograph of figure 5.5b both the defect structure (local regions of high intensity) and the ferromagnetic phase (the more illuminated background) are visible. These two topographs were recorded at a cold head temperature of 40.95K due to characteristic effect of lowering the transition point on the application of a b axis field in the manganese phosphide (figure 1.11).

5.2a Discussion.

Prior to any analysis of the effect of the defect structure on the spatial distribution of the magnetic phases the defect type should be classified. The majority of these defects are precipitation centres, formed during the very last stages of the solidification of the crystalline sample from a molten flux. On spark cutting the topography platelet one of its main surfaces appeared damaged by a series of pitted regions which correspond to the above mentioned precipitation centres. These pitted regions can be seen as holes on the surface photograph of the (a,b) sample illustrated in figure 5.4c. The position of the surface pit defects clearly correspond to the majority of distortion centres imaged on the nuclear topographs of figure 5.3, with the remainder of the defect images probably originating from defects contained within the bulk of the sample.

Figure 5.5: The neutron topographs of the 2+τ 00 magnetic and 200 nuclear reflections under an applied 0.186 Tesla b axis field at a cold head temperature of 40.95K.

Following the work of Eshelby (1956), it is now accepted that precipitates will form localised stresses in the crystal lattice. These stresses can be both compressional or tensional depending on the precipitate size and position. This distortion partially remains even if the precipitate itself is no longer present. Hence the (a,b) manganese phosphide sample can be considered as a high quality crystal lattice which is interspersed with local regions of high stress induced by precipitation centres.

Hirahara et al. (1968) performed an investigation into the effect of the application of a uniaxial stress on the transition temperatures of the manganese phosphide system The most profound effects were observed along the a and c axes, with the b axis showing only 10% of this effect. These results are however in contradiction with the thermal expansion measurements of Okamoto et al.(1968), which show that the a axis undergoes the smallest effect on passing through the metamagnetic transition. It should be noted that the results of Okamoto et al. (1968) have been adjusted following the publication of Ishizaki et al. (1970) on the magnetostriction of MnP where it was suggested that the proposed axis notation did not actually follow the convention of Huber & Ridgley (1964), where a > b > c. The results of Ishizaki et al. (1970) are in total agreement with the modified results of Okamoto et al. (1968) for both c and b axis applied fields.

It is thus concluded here that in light of these results the axis notation of Hirahara et al. (1968) is incorrect and the axes a and b should be changed to represent the b and a axes respectively. Assuming this notation, the results of Okamoto et al. (1968) predict that a compressional stress along the b axis will increase the T_M whilst compression along the a and c axes will decrease T_M. These effects are inferred to explain the stabilisation of the ferromagnetic phase from within the helimagnetic phase and the residual helimagnetic phase which is left in the ferromagnetic phase on the passage of the phase boundary (figure 5.3c).

Clearly a defect which produces compression along a b axis will locally reduce T_M allowing the nucleation of a localised ferromagnetic phase. Alternatively, if a phase boundary passes through a region leaving a helimagnetic region in a majority ferromagnetic phase, then this can be attributed to a local compressional stress along either the a or c axis (which has the effect of increasing the transition temperature). The stress produced by a given defect cannot be represented by a uniaxial stress and as such it is slightly misleading to describe these effects in terms of a single axis. However, the ferromagnetic regions (imaged on the magnetic topographs illustrated in figure 5.3) appear to elongate only along the a axis on increasing the sample temperature. Evidence related to the depth of these isolated regions of ferromagnetic phase can be gained by digitising the topography data.

Figure 5.6 shows a digitised version of the topograph illustrated in figure 5.3b along with a series of three line profiles indicating the spatial distribution of the intensity detected on the topograph. The profiles illustrated in figure 5.6b, c and d were taken horizontally at the positions B, C, and D respectively. These three scans show that the intensity modulations (representative of the chirality domain structure) seen above and below the isolated cluster can also be detected across the ferromagnetic region as seen at C. Thus it can be concluded that the ferromagnetic region does not exist across the whole thickness of the sample but merely a fraction of it. This result supports the assumption that the ferromagnetic regions are actually nucleated on the defect pits (which are located at the sample surface), and that they stabilised predominantly along the a axis of the sample.

From the above data it appears that the stabilisation of these isolated ferromagnetic regions do occur along a single crystalline axis. Moreover, since the application of a b axis field does not have a noticeable effect on these regions it is thought that they could be stabilised as a result of a localised a axis stress produced as a result of the precipitation points within the sample.

Figure 5.6: The digitised version of the neutron topograph shown in figure 5.3b <+> showing the isolated region of ferromagnetic phase (F) with a series of line profiles of the intensity values across the sections taken at A (slightly above F), B (at F) and C (below F).

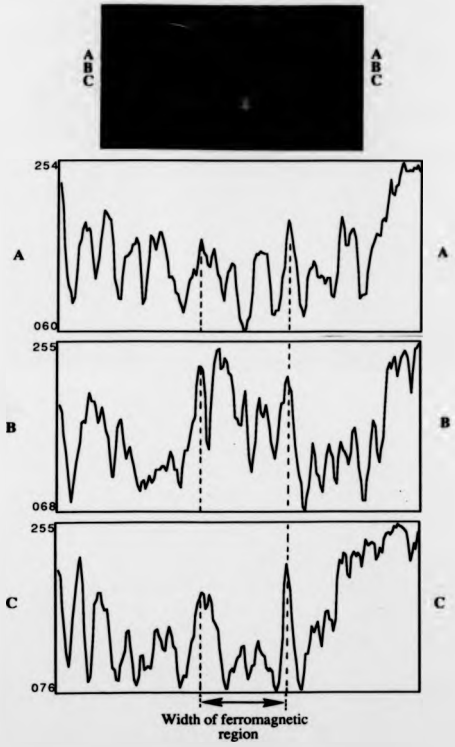

A similar effect of strain induced nucleation was reported by Jourdan et al (1988) in a synchrotron radiation topography investigation of the α to β phase transition in titanium. In the case of titanium each of the two phases could be nucleated in the other as a result of the presence of sample defects within the mother phase. The stabilisation and subsequent growth of these regions of isolated phase were supported by the presence of local strains as postulated above for the case of manganese phosphide.

The topographs shown in figure 5.5 represent an attempt to reorientate the growth of the ferromagnetic phase along the **b** axis (which is magnetically more favourable than the **a** axis and parallel to the chirality domain structure of the sample), by the application of a parallel external **b** axis field. In this configuration (neutron polarisation perpendicular to the propagation of the helix) it is not possible to image chirality domains. However, several vertical striations can be seen on the magnetic topographs of figure 5.5a. These lines represent a reduction of extinction on crossing the chirality domain walls as previously described by Baruchel & Schlenker (1989).

A comparison of the topographs of figure 5.5 with those taken in a moderate **a** axis field (figure 5.3) show no variation in the dimensions of the isolated ferromagnetic clusters. From a magnetostatic viewpoint it can be concluded that the **b** axis field has limited effect on the dimensions of the ferromagnetic cluster as a result of its domains running perpendicular to **b**, along the **c** easy axis. These topographs also show that the isolated regions of helimagnetic phase (figure 5.3b & 5.3c) are reduced on the application of the **b** axis field. This effect is to be expected since the **b** axis field (0.186 Tesla) is not sufficient to drive the sample into the fan phase, but it will however favour the ferromagnetic phase as seen by Ishizaki et al. (1970). Bearing in mind that the sample is under a temperature gradient (and possibly by accident a slight applied field gradient), then the effect of applying the *b* axis field can be represented as a percentage decrease in the ferromagnetic volume of the sample (the shaded region of the figure 5.7), at a given sample temperature. Since the sample is in phase coexistence at this point, a small

Figure 5.7: The reduction of the helimagnetic volume of a sample during phase coexistence by the application of a b axis field.

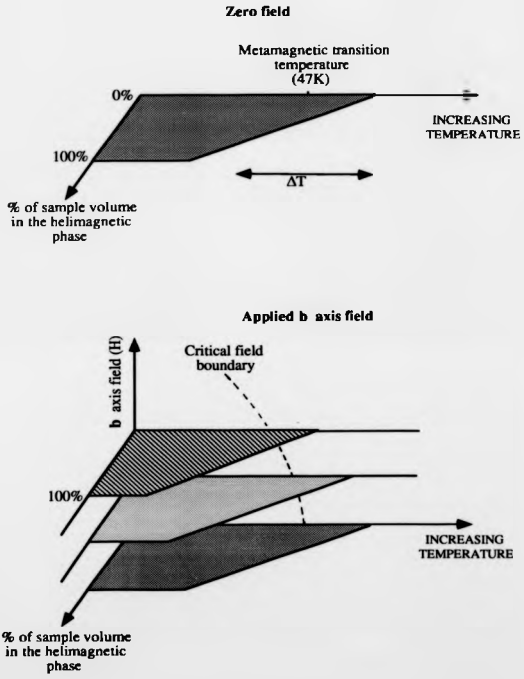

variation of the phase boundary condition could drive the isolated helimagnetic regions into the ferromagnetic phase as seen in figure 5.5.

5.3 The Triple point of manganese phosphide.

The critical field diagram of manganese phosphide (figure 1.11) shows that at a certain temperature and on the application of a relatively small (≈ 0.3 Tesla) **b** axis field the sample can be driven to a position where three magnetic phase boundaries (between the helimagnetic, ferromagnetic and fan phases) will all meet. This point is termed a triple point.

The application of a temperature gradient (ΔT) across the sample simplifies the location of the triple point by allowing the applied magnetic field to be varied over a fixed effective temperature range (figure 5.8a). A second possibility (and one which was used on the (**b**,**c**) manganese phosphide sample) is to apply a magnetic field gradient (ΔH) to the sample as well. This can be achieved by simply placing the sample as near as possible to one of the magnetic pole pieces of the electromagnet. Increasing the applied magnetic field in this state is equivalent to vertically translating a rectangle through the phase diagram (figure 5.8b), where the vertical dimension of the rectangle would represent the value of ΔH across the sample and the horizontal dimension the ΔT value.

Figure 5.9 shows a series of synchrotron radiation topographs taken on the 140 reflection of the (**a**,**b**) manganese phosphide platelet whilst under the influence of an applied **b** axis field. The noticeable features of these topographs are a) the passage of the helimagnetic-ferromagnetic phase boundary (from left to right) on increasing the field from 0.198 Tesla to 0.226 Tesla and b) the disappearance of this boundary (on increasing the field further still) on the occurrence of a second transition. The presence of two transitions is not evident (except by the disappearance of the original phase boundary), from the still topographs of figure 5.9. However, by monitoring the realtime variation of the diffraction spot with a video system both transitions were clearly visible. Moreover,

Figure 5.8: The experimental procedure to observe the triple point for a given temperature and a variable applied b axis field (along the arrows) for a sample with a) a temperature gradient and b) both a temperature and an applied field gradient, across the volume.

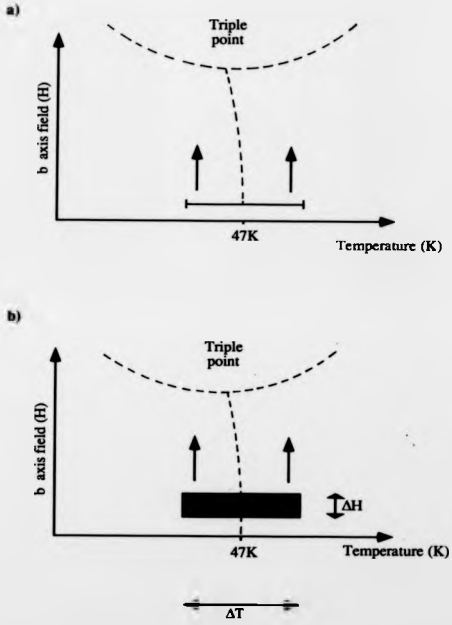

Figure 5.9: A series of synchrotron radiation topographs showing the variation of the diffracted intensity of the 140 reflection of the (a,b) manganese phosphide crystal as a function of the applied b axis field for a fixed cold head temperature of 39.55K.

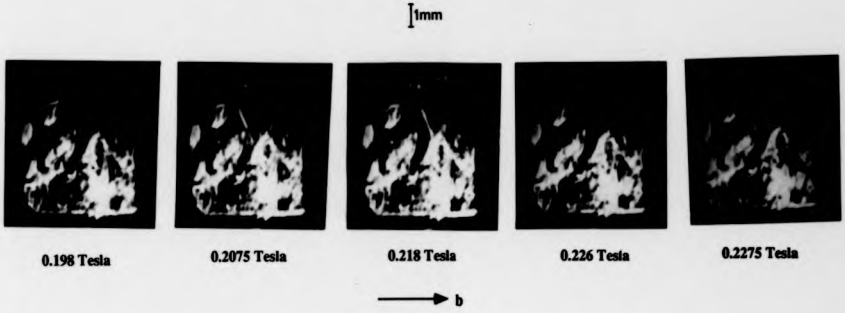

the second transition appears to grow from the initial helimagnetic-ferromagnetic phase boundary and passes directly to the edges of the sample.

Figure 5.10 shows the temperature variation of the critical fields in the (b,c) manganese phosphide sample as a function of the different tilt angles applied to the electromagnet. These measurements were taken by observing the appearence of the phase boundaries on the 020 reflection using real time synchrotron radiation topography. It should be noted that the temperature values given in figure 5.10 have been corrected to be representative of the actual sample temperature, as the thermometry is set around 8mm from the sample position and the sample is also subject to the radiative heating of the incident beam. It can be seen from these data that as the tilt angle of the electromagnet is increased both the initial critical field and the magnetic triple point (marked as T_T in figure 5.10) migrate to higher temperatures. At the limit of tilting the electromagnet the critical field values begin to resemble the curve given in figure 1.11b for a purely b axis field.

The two sets of synchrotron radiation topographs illustrated in figures 5.11 & 5.12 were taken at a fixed temperature on the 020 reflection of a (b,c) manganese phosphide for a tilt angle at the electromagnet of 2 and 3.5 degrees respectively. As in the previous topographs of figure 5.9, the sample contains two coexisting magnetic phases (heli-ferro) with a single type of phase boundary (vertical spikes along the easy c axis direction), at lower applied b axis fields. On increasing the applied field to a given point, a third magnetic phase appears with an associated increase in the number of different types of phase boundary. The ferro-fan boundary takes the form of a spiked region oriented slightly off the vertical direction and the broader, curved boundary being that of the transition from a helical to fan phase. The black spots present in all of these topographs originate from the incident synchrotron beam and not from the sample. They are thought to be absorbing depositions on one of the beryllium windows of the beam guide but their exact origin is not known. On the topographs shown in figures 5.11 & 5.12 the left hand edge is less intense than the rest of the image. This reduction of

Figure 5.10: The temperature variation of the critical field of the (b,c) manganese phosphide sample as a function of tilt of the electromagnet from the horizontal axis.

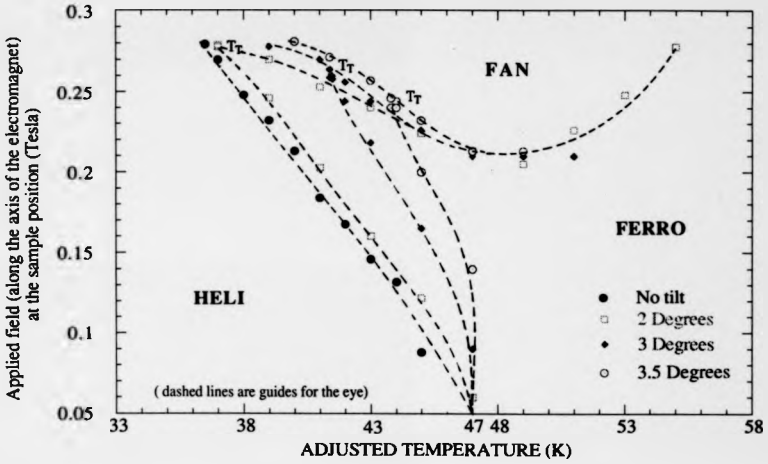

Figure 5.11: The applied field variation of a series of synchrotron radiation topographs taken on the (b,c) manganese phosphide sample at an adjusted sample temperature of 38.5K with the electromagnet tilted two degrees from the horizontal.

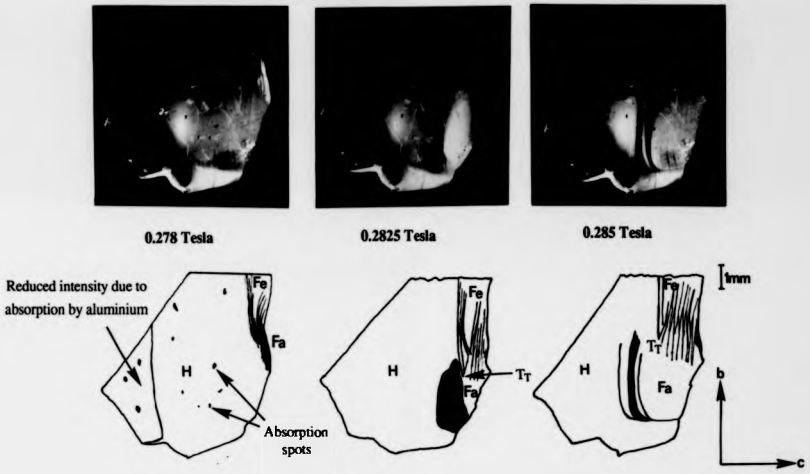

Figure 5.12: The applied field variation of a series of synchrotron radiation topographs taken on the (b,c) manganese phosphide sample at an adjusted sample temperature of 38.5K with the electromagnet tilted 3.5 degrees from the horizontal.

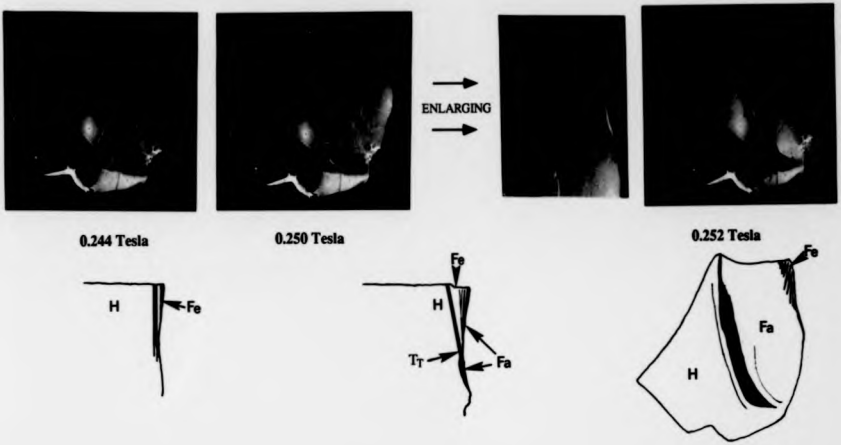

intensity is the result of absorption of the incident beam by an increased thickness of aluminium on the sample holder.

5.3a Discussion.

The synchrotron radiation topographs illustrated in figure 5.9 show the passage of the (a,b) MnP sample from a state of binary phase coexistence (ferromagnetic-helimagnetic) through a magnetic triple point and into a fan phase on increasing the applied b axis field. The passage through the triple point follows exactly the same path as described in figure 5.8 for a temperature gradient across the sample. Unfortunately, this limited series of 'still' topographs provides a poor representation of the real time effect of this transition, where the fan phase clearly nucleates from within the initial phase boundary before propagating (in the directions of both higher and lower temperature) towards the sample edges. This propagation of the fan phase is predictable from the magnetic phase diagram of MnP given in figure 1.11 for the (a,b) sample at a fixed temperature (as the component of the applied field in the easy c axis will be very small).

As seen in the previous neutron topographs (figure 5.3) the application of a b axis field has little effect on the direction of the phase boundary in the (a,b) MnP sample, since the elastic energy, driven by the presence of crystalline defects is the dominant energy term. For this reason it was decided to change the sample for one of much higher crystalline quality, but with the disadvantage that it had a (b,c) orientation. The (b,c) orientation is not favourable because if the sample is not mounted with the b axis perfectly horizontal then on the application of a horizontal field the sample will have a field component along the magnetically easy c axis. If the c axis component is too large then the sample will not pass into the fan phase, but will have a similar behaviour to that shown in figure 1.11a.

This c axis component can be reduced by tilting the electromagnet (figure 5.10) with the effect of reducing the field and increasing the temperature at which the triple

point occurs. The topographs illustrated in figure 5.11 were taken with the electromagnet tilted at 2 degrees to the horizontal and at an adjusted temperature of 38.5K as shown in figure 5.10. Below each diagram a schematic interpretation of the topograph is given where the labels H, Fe and Fa represent the regions of the sample which are in the helimagnetic, ferromagnetic and fan phases respectively.

The initial topograph (taken at 0.278 Tesla), shows all three magnetic phases but only two phase boundaries since the fan phase is bordered by either the ferromagnetic phase or the edge of the sample. The H-Fe phase boundary has a vertical spiked structure which lies parallel to the easy c axis of manganese phosphide. The orientation of the spiked boundary changes on passing from H-Fe to a Fe-Fa phase coexistence on the same topograph. The reorientation of these spikes prevents free poles forming at the Fe-Fa interface by producing a normal component to the interface which is the same for both phases. The orientation angle of these spikes from the vertical is dependent on the magnitude of the net ferromagnetic moment in the fan phase.

On increasing the applied field to 0.2825 Tesla the fan phase migrates across the ferromagnetic phase and through the H-Fe boundary. This topograph now shows three magnetic phases (H, Fe and Fa), three distinct phase boundaries (H-Fe, H-Fa and Fa-Fe), and a triple point (T_T) as marked on the schematic representation of this figure. The H-Fa phase boundary shows an increased width (approximately forty times larger than the previous boundaries) and in this case is represented by a very intense, smoothly curved region. Increasing the field further still (0.285 Tesla) drives the fan phase into both the helimagnetic and ferromagnetic regions of the sample. The triple point still exists but is now located at a different position to that of the previous topograph. It can be stated that both of these positions in the sample will be under exactly the same temperature and applied field conditions since the triple point can only be located at one specific value of temperature and applied field (given as 45.35K and 0.248T in the b axis by Ishizaki et al.(1970)). The H-Fa phase boundary is again represented by an intense area of increased

width but in this case it is surrounded by a region of very low intensity. In the central region of the sample the H-Fa boundary appears to be aligned predominantly parallel to the orientation of the Fe-Fa boundaries.

The approach to the triple point on the (b,c) sample differs from that observed on the (a,b) sample because the tangents to the critical field lines were changed on the application of a substantial c axis component of the applied field (figure 5.10). It is for this reason that the fan phase was not nucleated at the helimagnetic-ferromagnetic boundary (as seen in the topographs of figure 5.11), for a 2 degree tilt on the electromagnet. However in this configuration the possibility does exist to nucleate the ferromagnetic phase from within the helimagnetic-fan phase boundary by simply heating the sample from base temperature under an applied field. Unfortunately this was not possible here as the electromagnet was already working at its limit and consequently the ferromagnetic phase could not be completely expelled from the sample.

By tilting the electromagnet to the maximum value of 3.5 degrees the c axis component of the applied field was reduced further still in order to nucleate the fan phase within the helimagnetic-ferromagnetic phase boundary. The synchrotron radiation topographs taken in this regime are illustrated on the topographs of figure 5.12 as a function of increasing the applied field for an adjusted temperature of 43.8K. The initial topograph of this series was taken in an applied field of 0.244 Tesla and again shows the characteristic spiked H-Fe phase boundary. On increasing the the applied field to 0.25 Tesla the sample once again shows all three phases, three phase boundaries and a triple point. Although the topograph has been taken just at the onset of the fan phase it is not clear (even from the enlargement of the topograph) if it actually nucleated in the H-Fe phase boundary. From the critical field diagram taken at this configuration (figure 5.10) it does not seem very likely but the combination of both the applied field and the complicated temperature gradients across the sample make this prediction very difficult to confirm.

The final topograph shown in figure 5.12 (taken in an applied field of 0.252 Tesla) no longer shows a triple point since the fan phase has propagated too far into the ferromagnetic and helimagnetic phases. All three phases still exist but they are only separated by two (Fe-Fa and H-Fa) phase boundaries. The H-Fa phase boundary no longer appears to be oriented along a given direction but instead takes the form of a smooth curve. Neither the width nor the orientation of the H-Fa phase boundary are as yet understood.

5.3b The main results on the triple point of manganese phosphide.

The triple point of manganese phosphide has been directly observed using white beam synchrotron radiation topography. Three distinct phase boundaries have been observed between the coexisting helimagnetic, ferromagnetic and fan phases. The shapes of two of these interfaces (H-Fe and Fe-Fa), are at least quantitatively explained through the competition between the elastic and magnetostatic energy terms.

It has been shown that the triple point can be reached by nucleating the fan phase directly from the helimagnetic-ferromagnetic phase boundary when under the influence of an applied b axis field.

The presence of a c axis component to the applied field influences the fan phase to nucleate solely in the ferromagnetic phase. On increasing the applied field the fan phase then propagates across the ferromagnetic phase and into the helimagnetic phase to produce a triple point. The variation of mother phase (in which the third phase is nucleated) can be understood through the variation of the tangents to the phase boundaries at the triple point (figure 5.10). The presence of both temperature and field gradients allows the triple point to be moved across the sample surface (along a line of triple points) on increasing the applied field .

Further work to be done in this area includes a closer investigation of the helimagnetic-fan phase boundary as both the orientation and form of this boundary are as yet not fully understood. Secondly, an investigation into the proposed multiple transitions within the fan phase on increasing the b axis field (Beccera et al.(1988)), should be undertaken following a series of measurements where we have observed effects which could be interpreted as a second transition in the fan phase.

On increasing the applied b axis field to around 1.65 Tesla (above the limit of our present electromagnet) a second triple point can be located at the convergence of the paramagnetic, ferromagnetic and fan phases (Shapira et al.(1981)). This second triple point is particular in that the tangents of all the three phase boundaries are the same value at the triple point. This type of triple point is called a Lifshitz point. By following the ferromagnetic-fan critical field (the only phase boundary which corresponds to a first order transition at the high field triple point in manganese phosphide), the variation of the Fe-Fa phase boundary can be studied until its expected disappearance at the Lifshitz point.

The final proposed experiment of this chapter involves reducing the temperature and applied field gradients as much as possible and repeating the observation the Fe-Fa-H triple point. In this way the relative orientations of the phase boundaries (at the triple point), would be representative of their relative energies per unit surface (Landau & Lifshitz (1986)). Clearly with a spatial variation of the temperature and applied field across the sample the analysis of these phase boundaries would be more complicated. Achieving such 'clean' experimental conditions would be possible in a flow cryostat (where the cooling power is not restricted to the passage through a single point), with the sample centered between the poles of the electromagnet. As stated in the earlier sections of this chapter, as the temperature and applied field characteristics of the sample become more uniform then the observation of the triple point will become increasingly more difficult.

CHAPTER SIX

THE 20K PHASE TRANSITIONS IN HOLMIUM

6.1 Introduction.

The proposed first order transition from a helical antiferromagnet to a low temperature conical phase in holmium is as yet not fully understood. The "spin slip" model proposed by Bohr et al. (1986) describes the majority of the phase diagram of holmium in terms of a periodic absence of magnetic moments aligned around the six easy basal plane directions and discommensurations. However at the onset of the conical phase the spin slip model predicts a single anomaly rather than the double anomaly observed by Bates et al.(1988) from ultrasonic attenuation measurements. Allied to this is the claim by McMorrow et al.(1991) of a lack of neutron diffraction evidence to support the existence of a conical phase with a component of the magnetic moment along the c axis. Finally there is the unexplained increase in the integrated intensity on passing through the helical to conical transition as first observed by Drillat (1983).

This chapter will deal initially with the anomalous increase in the integrated intensity detected on the 002$\pm\tau$ magnetic satellite reflections. An attempt will be made to detect a c axis component of the magnetic moment and these results will be used to clarify the complex magnetic transition at 20K.

6.2 The transition from helical to the low temperature phase in holmium.

The holmium crystal used in the following neutron diffraction and topography data was spark cut from a single crystal rod, in the form of a (b,c) axis disc, 5 mm in diameter and approximately 0.3 mm thick. The crystal was grown by solid state

electrotransport at the University of Birmingham by Dr. D. Fort, using the purest materials available from the Ames Laboratory. The resistivity ratio of the sample is ≈100.

The holmium sample was mounted on S20 (as previously described in Chapter three), in zero applied field, with an incident 1.7Å monochromatic beam produced by a Heusler alloy 111 monochromator. All the reported integrated intensity measurements using this monochromator actually represent the summation of the integrated intensities from both 'up' and 'down' polarisation states. Figure 6.1 shows the thermal evolution of a) the integrated intensities and b) the widths of the rocking curves, of the 002-τ and 002+τ reflections in the temperature range from 13K to 26K. Figure 6.1c shows a plot of the temperature variation of the interplanar turn angle (obtained from the satellite positions as described in equation (6)), over the same range.

The widths of the two satellite peaks plotted in figure 6.1b. clearly increase in the region of 19K. The peak values of the magnetic satellite widths coincide exactly with the central position of the abrupt change in the interplanar turn angle (ϕ), as plotted in Figure 6.1c. The width of the nuclear peak has not been plotted as it remains constant (0.15 degrees) across the whole temperature range. The turn angle reaches a low temperature limiting value of 30 degrees, which corresponds to the 1/6 "lock in" structure as previously observed by Koehler et al. (1966) and Cowley et al. (1989).

Figure 6.2 shows the temperature evolution of the ratio of the integrated intensities of the 002-τ satellite to the 002 nuclear reflections for incident neutron wavelengths of 1.0, 1.7 and 2.4 Å. As in figure 6.1 the 1.7 Å data were taken using a Heusler 111 monochromator whilst the 1.0 Å and 2.4 Å data were taken with a Cu 111 monochromator and a Ge 111 monochromator respectively, in order to avoid $\lambda/2$ contamination.

Figure 6.3 shows two polarised neutron topographs taken at a) 18.9K which corresponds to the position of the peak in the integrated intensity previously observed in

Figure 6.1: The temperature evolution of a) the integrated intensities of the 002±τ and 002 nuclear reflections, b) the widths of the 002±τ reflections and c) the interplanar turn angle, of a (b,c) holmium sample in zero applied field.

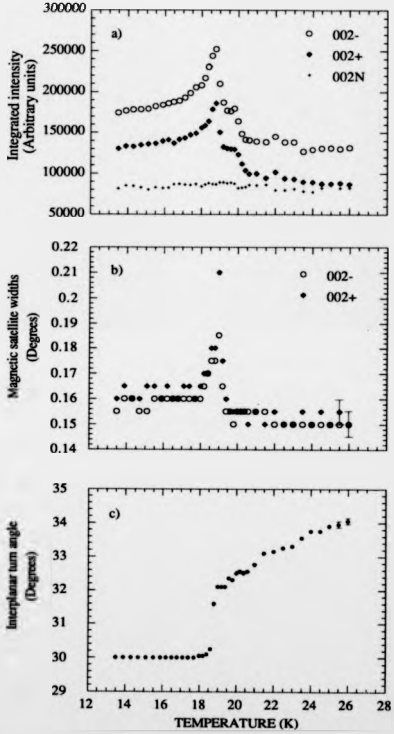

Figure 6.2: The temperature variation of the ratio of the integrated intensities of the 002-τ and the 002 reflections as a function of the incident neutron wavelength.

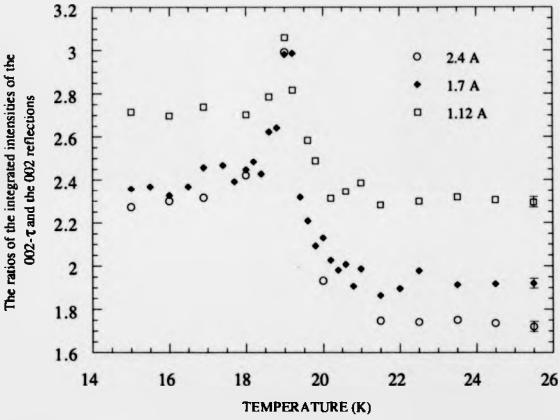

Figure 6.3: Two polarised neutron diffraction topographs of the 002-τ magnetic satellite reflection taken in the down state neutron polarisation at a) 18.9K in a 0.04T c axis field and b) 18.6K in a 0.025T c axis field.

a)

1mm

b)

figure 6.1 and b) 18.6K which is just below the transition in the low temperature phase. Both of these topographs show a similar, characteristic "P" type chirality domain structure (formed on entering the helimagnetic phase from the paramagnetic phase). Only minor differences can be seen in the chirality domain patterns of these two topographs.

Figure 6.4 shows the temperature variation of the 110 nuclear reflection as measured in zero field using a Ge 111 monochromator at a wavelength of 2.4 Å, together with the results of Koehler et al. (1967), which were adjusted to our results for temperatures greater than 24K.

The magnetisation data of Figure 6.5 shows a smooth increase in the c axis magnetisation (recorded on the same holmium crystal as used in the neutron diffraction investigation), when decreasing the temperature to just above 20K. Slightly below 20K an anomalous maximum occurs, which on the application of increasingly large c axis fields migrates to lower temperatures and becomes less pronounced. Hysteresis of the magnetisation was observed around these anomalous maxima on thermal cycling the sample.

Figure 6.6 shows the variation of the sample magnetisation as a function of the applied c axis field for a selection of sample temperatures. These data show a nearly constant susceptibility on decreasing the sample temperature.

The integrated neutron intensity also displays hysteresis on cycling in temperature as illustrated in the scans taken on the 002-τ satellite using a Cu 111 monochromator at 1.7 Å (Figure 6.7). The intensity remains constant throughout the low temperature "conical" phase on heating the sample and eventually passes back to the helical phase at 20.5K. This appears to be a true temperature effect as no temporal variation was observed on any of the measured integrated intensities over periods of up to eight hours.

Figure 6.4: The temperature variation of the integrated intensity of the 110 nuclear reflection; (⊙) as measured in this investigation and (•) as measured by Koehler et al (1966). The dotted lines are guides for the eye.

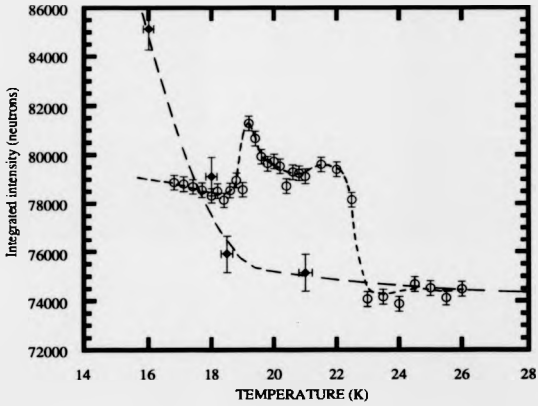

Figure 6.5: The temperature variation of the sample magnetisation as a function of the applied c axis field.

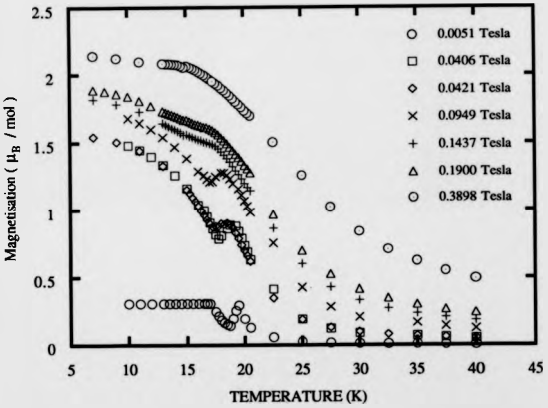

Figure 6.6: The applied field variation of the sample magnetisation as a function of the sample temperature.

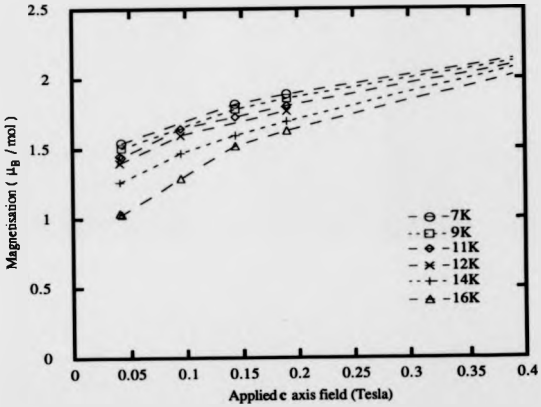

Figure 6.7: The temperature evolution of the ratio of the integrated intensity of the 002-τ magnetic satellite to the integrated intensity of the 002 nuclear reflection (which remains practically constant), for the holmium (b,c) sample in a 0.03 Tesla applied c axis field.

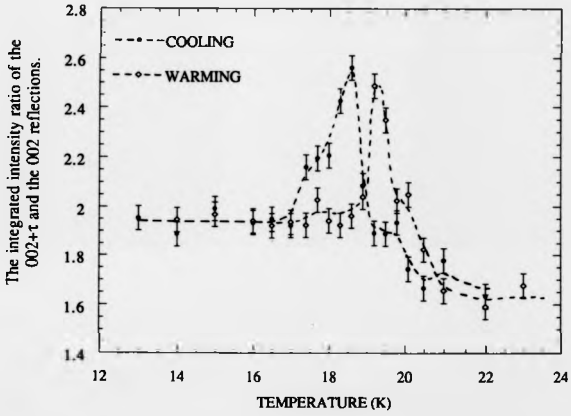

The application of moderate fields (up to 3.5 .10^{-2} T) along the c axis shifts the maximum in integrated intensity to lower temperatures, as seen in the series of scans illustrated in figure 6.8. The ratios of the integrated intensities of the 002-τ magnetic satellite to the 002 nuclear reflection (which were again measured as constant across the the limited temperature range of 13 to 26K), are plotted as a function of temperature for several applied c axis fields. The shift of the peak value to lower temperatures on the application of an applied field is a reversible process with the peak intensities occurring at the same temperature values on removing the field. The application of a c axis field appeared to have the irreversible effect of increasing the ratio in the peak intensity values. The increase in the satellite peak width and the abrupt change in the interplanar turn angle both followed this migration of the peak intensity to lower temperatures on the application of a 0.025 Tesla c axis field. However, no evidence was found for the stabilisation of a given propagation vector under the influence of this moderate c axis field.

Figure 6.9 shows the ratios 002-τ magnetic to the 002 nuclear integrated intensities as a function of temperature on the application of a $3x10^{-2}$T b axis field. Two abrupt intensity increases can be seen at 22.5K and 19.2K in this data. As in the similar data of figure 6.1 the maxima of each of these integrated intensity peaks occur at the same temperature as the central regions of the two abrupt changes in the interplanar turn angle (figure 6.7c.). There was no observable increase in satellite width related to the higher temperature intensity peak at 22.5K.

Longitudinal ultrasonic measurements under a c axis applied field have confirmed both the above mentioned hysteretic behaviour, where the transitions shift to lower temperatures on the application of increasingly large c axis magnetic fields, and the existence of a double anomaly as reported by Bates et al. (1988).

Figure 6.8: The temperature evolution of the ratio of the integrated intensity of the 002+τ magnetic satellite to the integrated intensity of the 002 nuclear reflection as a function of the applied c axis field for the holmium (b,c) sample.

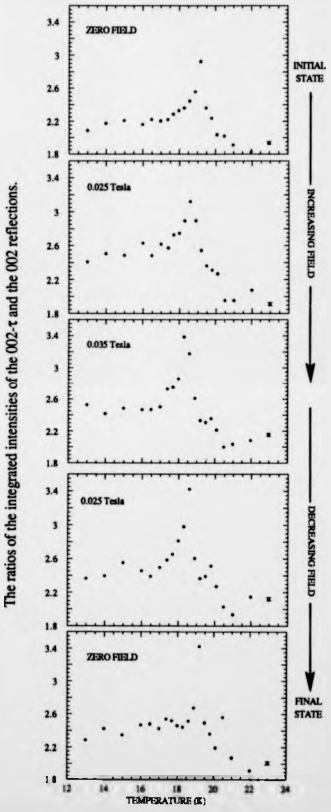

Figure 6.9: The temperature evolution of a) the integrated intensities of the 002±τ and 002 nuclear reflections, b) the widths of the 002±τ reflections and c) the interplanar turn angle, of a (b,c) holmium sample in a 0.025 Tesla 'b' axis applied field.

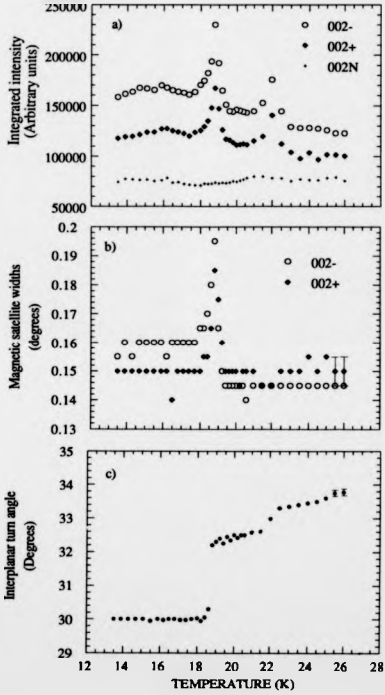

6.2a The anomalous integrated intensity increase.

The large variation in the intensity of the two 002±τ magnetic reflections on passing through the helimagnetic to the low temperature phase transition is not predicted by a simple consideration of the rotation of the magnetic moments. Moreover, a reduction of approximately three percent is expected (from the kinematical theory approach), by the reported 10 degree canting of the basal magnetic moments along the c axis (Bohr et al 1986).

The peaks in the integrated intensity (illustrated in figure 6.1a) were recorded in zero field at 19.2K, which is approximately the same temperature at which the transition from a helical to a conical magnetic structure had been previously observed at (Koehler et al. 1967). It is clear (figure 6.1c) that the transition to a commensurate phase is first order. The unexpected increase in the integrated intensity could be therefore at least partially attributed to a reduction of extinction arising from local disorder during this transition.

From the data illustrated in Figure 6.2 the maximum values of the ratios of the 002-τ satellite and 002 nuclear integrated intensities for the neutron wavelengths of 1.0, 1.7 and 2.4 Å are all less than 3.7 (the value predicted by the kinematic theory of diffraction for the ratio of the integrated intensity detected on the 002-τ magnetic satellite to that detected at the 002 nuclear position). These integrated intensity ratios also decrease on increasing the incident neutron wavelength. Both of these phenomenon are characteristic of extinction effects.

Neither the integrated intensity nor the full width half maximum of the rocking curve of the 002 nuclear reflection exhibit increases similar to those observed on the magnetic satellites. This was the case for all the measurements of the integrated intensities and the FWHM of the 002 nuclear reflection which were carried out in this investigation. The absence of any modification to these nuclear diffraction characteristics indicates that if

the increase in integrated intensity is to be explained by extinction effects, then this should be confined solely to magnetic extinction effects.

Following the work of Baruchel et al. (1986) and Baruchel & Schlenker (1989) an obvious next step is to image the chirality domain structure both within the transition and at a temperature just below the transition. If the average chirality domain size is reduced on passing through this transition, then this could be attributed to an equivalent decrease in the characteristic block size of the mosaic model as employed in standard secondary extinction theories. Such a decrease in block size would then explain the origin of the enhancement of integrated intensities as seen in Figures 6.1, 6.7, 6.8 and 6.9.

Figure 6.3 shows two such polarised neutron topographs taken at a) 18.9K (the position of the peak in integrated intensity), and b) 18.6K which was below the first order transition in the low temperature phase. Only a few minor details of the chirality domain structure are modified on passing through the transition and hence this does not appear to be the cause of the anomalous increase in intensity.

6.2b The application of the mosaic block model.

The modelling of the temperature variation of the integrated intensities measured through the transition will be performed using the mosaic block model. Within this model the two basic parameters which can be used to define the crystalline structure are the mosaic block size (R) and the mosaic misorientation of the sample described by the parameter (g). This mosaic misorientation can be divided into two subgroups; the deviation from the average orientation of mosaic blocks ($\Delta\theta$), and the lattice spacing gradient ($\frac{\Delta d}{d}$). The lattice spacing, or cell parameter gradient can be seen to be related to average angular misorientation by differentiating Braggs law, for a fixed wavelength,

$$2d \cos\theta \, \Delta\theta + 2\Delta d \sin\theta = 0$$

$$\frac{\Delta d}{d} = \frac{\Delta\theta \cos\theta}{\sin\theta}$$

which gives,

$$\frac{\Delta d}{d} = \frac{\Delta \theta}{\tan \theta} \qquad (73)$$

The magnetic analogies of these nuclear parameters can be clearly expressed in the helimagnetic state. The magnetic coherence length (R_m) of the helical structure represents the mosaic block size parameter. It should be noted that R_m can be smaller than the average chirality domain size if the coherence is lost within a given domain. This is an important consideration as the chirality domain size is almost constant across the low temperature phase transition (figure 6.3).

Just as for the nuclear misorientation two analogous magnetic misorientation parameters can be described by the one variable g_m. The direct angular misorientation will be described by the deviation of the direction of the propagation vector of a given helical region from the mean value of the system. The magnetic analogy to the lattice parameter gradient will be represented by a magnitude variation of the helical propagation vector or equivalently, the variation of interplanar turn angle (ϕ) across the sample volume.

The ratios of the integrated intensity curves shown in figure 6.2 were initially modelled using Zachariasen's (1967) interpretation (modified by Becker & Coppens 1974) of the mosaic model. The high temperature (25.5 K) integrated intensity ratios were taken to represent an initial, "stable state" and were modelled as a function of two general parameters R and g. These two parameters were assumed to represent the whole system at 25.5K and could be divided into variable R_m and g_m parameters at lower temperatures, but with their values being fixed for the nuclear parameters R_n and g_n. This simulation produced a very large mosaic block size ($R > 100\ \mu m$) and a misorientation of less than 10 seconds of arc (where the misorientation is given by $1/(3g)$), as is typically associated with a sample of high crystalline quality. The predicted extinction coefficients were approximately $y_N = 0.32$ and $y_s = 0.17$ which are clearly below the limit of validity of Zachariasen's model (given in chapter two to be $y \sim 0.8$). The value of 0.34 for the

goodness of fit parameter also indicated that this simulation was not generating acceptable values.

The treatment of secondary extinction effects through Sabine's treatment of the mosaic model allows the description of samples which have extinction coefficients much smaller than the $y \sim 0.8$ limit of Zachariasen's model. The 25.5 K intensity data of figure 6.2 were thus modelled (using a simple FORTRAN 77 program), in accordance with the equations furnished by Sabine (1988) through the two parameters R and g.

The simulation generated the general values for a characteristic block size of 41.6μm and a g value of 1500 (implying a misorientation of ~ 46 seconds of arc). These values were then fixed for the nuclear intensity (which was observed to be constant as a function of temperature) and then a selection of intensities were modelled as a function of a magnetic block size (R_m) and a magnetic misorientation (g_m) at 20.0; 19.6, 19.0, 18.0, 16.0 and 15.0 K.

The predicted values of R_m and g_m can be seen in figure 6.10 as a function of temperature, along with a measure of the accuracy of the simulation and the predicted extinction coefficients for a neutron beam of wavelength 1.7 Å. This data indicates that the simulation is more dependent on the magnetic misorientation of the sample than on the magnetic block size, as the variation of R_m is minimal compared with that of g_m across the transition. This result was contrary to our first expectation that the reduction in the 'magnetic' integrated intensity below the transition point was in fact due to an increase in the magnetic coherence length of the system. It should be noted that the goodness of fit parameter increases substantially around the transition point (18 and 19K), which indicates that this solution is not wholly acceptable.

The dependence of the system on the misorientation parameter g_m can be exaggerated by fixing R_m to the arbitrary value (35 μm) and only allowing g_m to vary, as shown in figure 6.11. The result is a very large predicted variation of the misorientation

Figure 6.10: The predicted values for the computer fit of the integrated intensity data of figure 6.2 for a selection of sample temperatures.

Temperature (K)	Goodness of fit	R (μm)	g	Extinction coefficient y(002-)	Extinction coefficient y(002N)	Extinction coefficient y(002+)
25.5	$1.31.10^{-2}$	40.4	1800	0.224	0.466	0.248
20.0	$3.71.10^{-2}$	37.9	1400	0.248	0.466	0.274
19.6	$2.32.10^{-2}$	35.8	1310	0.262	0.466	0.289
19.0	$6.83.10^{-2}$	31.1	340	0.348	0.466	0.373
18.0	$4.78.10^{-2}$	35.0	730	0.293	0.466	0.318
16.0	$2.08.10^{-2}$	34.8	980	0.282	0.466	0.308
15.0	$1.23.10^{-2}$	34.5	1100	0.279	0.466	0.305

Figure 6.11: The variation of the magnetic parameter g_M (using the secondary extinction interpretation of Sabine) as a function of temperature for fixed values of the parameters R_M, R_N and g_N.

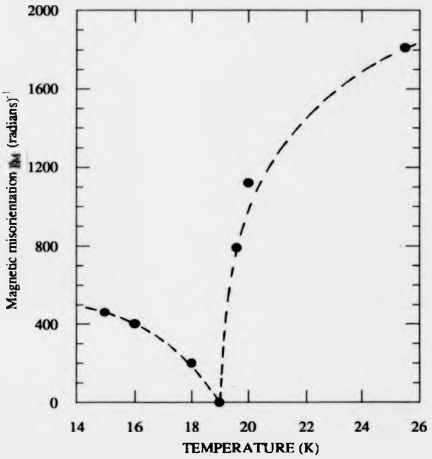

parameter (g_m) which at its maximum value corresponds to a misorientation greater than 360 degrees. Such a misorientation is nonsensical and hence the introduction of a third free parameter was considered to describe the transitional region of the integrated intensities.

The average blocksize parameter has been taken here to represent the average coherence length of the helical structure, but what is particularly interesting for the description of the anomalous integrated intensity increase are the regions of the sample which exhibit the smallest coherence lengths. If the coherence length of a given region is much smaller than the extinction length, then this region will diffract in accordance with the kinematic theory, producing an increased diffracted intensity. Hence the introduction of an associated kinematical fraction of the sample volume as a third free parameter would take into account the regions of smaller coherence length as well as reducing the misorientation parameter g_m to a meaningful value. However, care must be taken when introducing extra free parameters since an adequate description of a system can always be achieved given enough free parameters.

6.2c The RED theory simulation.

The RED theory offers an elegant solution to this problem since the asymmetric γ function, which describes the reflectivity, automatically compensates for regions of the sample which diffract in the kinematical approximation by allowing the mosaic width parameter (α) to tend to zero. Moreover, the RED theory separates the two contributions to the magnetic misorientation (g_m) through the parameter c. When the parameter c tends to 1 then the misorientation is attributed to a lattice parameter gradient in the nuclear case and a variation of the interplanar turn angle in the magnetic case. As c tends to zero then the magnetic misorientation is attributed to the variation of the direction of the propagation vector of the helical modulations.

A reduced selection of intensity ratios were consequently fitted to the RED theory of diffraction through a computer program developed by J. Kulda. During the computer

simulation the value of the c parameter was much nearer to one than zero which indicates that it is the variation of the interplanar turn angle which plays the major role in the magnetic misorientation. Moreover the results shown in figure 6.12 show that around 19K (the temperature which corresponds to a maximum in the detected integrated intensity), the misorientation becomes even more dependent on the interplanar turn angle with the c parameter giving a value of 0.9975. Throughout these fits the α parameter was free to vary, but in each case produced values which were not significantly different from zero (indicating an exponential form to the reflectivity curve hence describing a series of small highly distorted regions). As previously mentioned, all the parameters related to the nuclear reflection were fixed, with only the magnetic bending radius (R_m) showing any fluctuation across the transition. As in the secondary extinction simulation (figure 6.10) the goodness of fit parameter was increased at the transition position, but in this case only to twice the value seen in the low temperature phase.

The proposed dependence of the misorientation on the interplanar turn angle can be substantiated by measuring the rocking curves of the 002-τ magnetic satellite at temperatures which correspond to the two wave vector states before and after the abrupt reduction of wave vector. By adding these two peaks together and measuring the subsequent FWHM this will provide an indication of the misorientation induced in the system as a result of the coexistence of two different wave vector states. The rocking curve of the intensity measurement made at T=18.4K in figure 6.9. was added to that taken at T=19.0K and the FWHM of the resultant rocking curve was measured as 0.21 degrees. This simplified approach, will yield the maximum misorientation since it assumes that both wave vector states (corresponding to the peak position of two measured rocking curves) exist in equal proportions at the transition. Clearly any fraction of this value can be achieved down to the limiting values of the FWHM values of the component rocking curves by varying the compositional quantities of each wave vector state. This being the case, the substitution of the FWHM value into equation (68) produces an average magnetic misorientation of 8.0 ± 1.0 minutes of arc within the sample. This value

Figure 6.12: The temperature variation in the fitting parameters of the RED primary extinction model as applied to the integrated intensities of the 002 magnetic reflections of holmium.

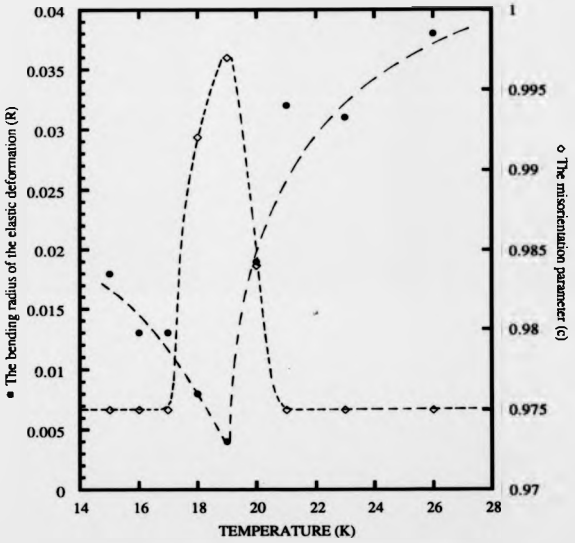

is of the same order of magnitude as that predicted from the initial treatment using the secondary extinction model proposed by Sabine (1990). A direct comparison to this misorientation value cannot be given for the RED treatment since it is not appear as a free parameter of the model. Nevertheless, the treatment of the anomalous integrated intensity increase by RED model clearly indicates that this is a result of the reduction in the extinction due to the coexistence of regions of different interplanar turn angle.

6.3a The c axis component of the magnetic moment.

The temperature variation of the integrated intensity measured on the 110 nuclear intensity (indicated by the open circles of figure 6.4) shows a 5% increase on passing into the low temperature phase. The results of Koehler et al. (1966) (plotted in the same figure as diamonds) also show an increase in the integrated intensity of the 110 reflection. However, Koehler et al. measured a 14% increase over the limited temperature range investigated here and an overall increase of around 21% on measuring down to 5K.

The origin of the increase in integrated intensity measured here is not thought to be due to an extinction related event as the FWHM of the 110 nuclear reflection has been measured at 0.44 degrees using a high quality Ge111 monochromator. This increase in FWHM indicates that the crystalline quality is anisotropic with the (110) planes being of inferior crystalline quality to those previously observed on the 002 peak.

Koehler et al (1966) explained the increase in the 110 nuclear integrated intensity as a 1.7 μ_B ferromagnetic component along the c axis. McMorrow et al. (1991) tried to confirm this claim by measuring the temperature variation of integrated intensity of the 100 nuclear peak and reported that this value was almost independent of temperature between 40 and 4.5K. However, a closer inspection of this data would indicate that they did in fact measure an approximate 14% increase in intensity in this region. This value is still below that measured by Koehler et al. (1966) and this discrepancy was tentatively explained by McMorrow et al. as being a result of the inferior crystal quality employed by

Koehler et al., which resulted in a coupling of the moments to the defect structure. No such effects should be present in our high purity sample.

Accepting (however small) a ferromagnetic c axis component of the magnetic moment would imply a conical phase and hence the simple measurement of the c axis magnetic moment on a magnetometer should clarify this point. The results of a series of magnetisation measurements taken over a range of applied c axis fields are illustrated in figure 6.5. The plateau in the magnetisation on the application of a small c axis field (0.0051 Tesla) occurs as a result of a demagnetising field effect, where the applied field is too small to saturate the sample.

The applied c axis field variation of the measured magnetisation is plotted in figure 6.6 as a function of a series of low temperature measurements (7 to 16K). The spontaneous magnetisation of the sample can be deduced by extrapolating the measured magnetisation value to zero applied field along the path of the susceptibility. The values of the susceptibility had to be taken at low temperature values because of the appearance of the anomalous boss in the magnetisation data at higher temperatures (figure 6.5). Even so, the susceptibility (which is a perpendicular susceptibility) still appears to be rather constant below 16K.

The temperature variation of the spontaneous magnetisation is plotted in figure 6.13. Extrapolating to 4.2 K predicts a spontaneous magnetic moment of $1.53 \pm 0.1\ \mu_B$ / mol along the c axis. This value is very close to the $1.7\ \mu_B$ / mol c axis magnetic moment predicted by Koehler et al. (1966) at 4.2K from a series of neutron diffraction measurements. These results give conclusive evidence for the existence of a net c axis magnetic moment at low temperatures (< 25K) in holmium.

Figure 6.13: The temperature variation of the c axis spontaneous magnetisation in holmium.

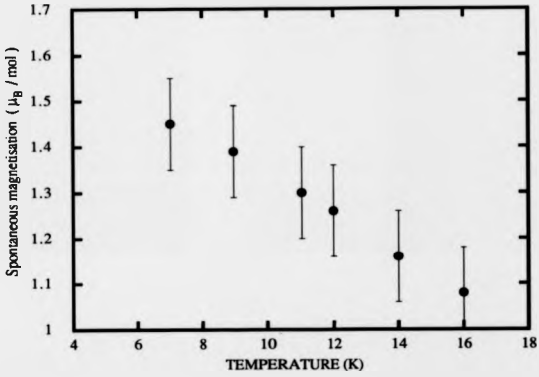

6.4 The 20K transitions.

In this chapter a large amount of data has been presented on the 20K transitions of holmium and as such it is important to clarify exactly what has been measured in each case. The neutron diffraction scans of the 110 nuclear peak and the c axis magnetisation measurements give evidence that the low temperature phase contains a net c axis moment and as such is conical in nature

The onset of the conical phase can be deduced from the magnetisation data of figure 6.5 by extrapolating to zero magnetisation along the tangent of the curves at their steepest point. In this manner the conical phase can be seen to be driven to higher temperatures on augmenting the applied c axis field. This effect can be understood as a lowering of the energy of the low temperature (conical) phase due to the action of the Zeeman term ($-\mu_o MH$), where the applied field (H) is parallel to the c axis magnetisation (M) of the cone axis.

The neutron diffraction scans of the 002 magnetic satellite indicate that the interplanar turn angle (ϕ) undergoes a first order transition to the "$^1/_6$ lock in" structure as previously observed by Koehler et al.(1966) and Cowley & Bates (1988). This transition results in an increase in the magnetic integrated intensity (figure 6.1), which has been explained in section 6.3 through a reduction of magnetic extinction. The abrupt change in interplanar turn angle and the increase in the integrated magnetic intensity are thus expected to occur at the same temperature as seen in figure 6.1. On the application of moderate c axis fields (up to 3×10^{-2} T), the increase in the integrated intensity of the 002-τ magnetic satellite migrates to lower temperatures (figure 6.8). This migration is reversible, with the peak position returning to its higher temperature value on removing the field.

Clearly the onset of the conical phase and the first order transition to the $^1/_6$ "lock in" structure are not one in the same, as the application of a c axis field has the opposite effect on the low temperature phase in each case.

On the application of a $3x10^{-2}$ T b axis magnetic field (figure 6.9), two peaks were measured in the integrated intensities of the 002-τ magnetic satellite reflection. As in the zero field and c axis field data both intensity increases correspond to abrupt changes in the interplanar turn angle of the system. The major peak in integrated intensity occurs at the same temperature as in the zero field case and again corresponds to the centre of the transition into the $1/6$ "lock in" structure. The second peak in the integrated intensity was recorded at 22.5K and corresponds to the $2/11$ "lock in" structure.

A noticeable feature of figure 6.9b is that the full width half maximum of the magnetic satellites does not increase at the position of the high temperature increase in integrated intensity. The absence of such an increase could be interpreted as there not being a sufficiently large change in turn angle between regions of the helimagnetic structure in the high temperature incommensurate wave vector state and those in the $2/11$ lock in structure (the change in wave vector at the $2/11$ lock in being three times smaller than that of the transition to a $1/6$ structure). Hence the superposition of the two rocking curves (which correspond to the $2/11$ and the incommensurate wave vector states), would not be sufficiently separated to cause a broadening of the detected peak on taking into account the instrumental resolution. This was in fact the case as the two individual rocking curves (taken at either side of the abrupt change in interplanar turn angle as illustrated in figure 6.9), were measured to have FWHM values of 0.14 degrees which were nearly the same value as that measured for the summation of the two individual rocking curves. This effect is still in keeping with the results of the RED primary extinction model. Moreover the increased integrated intensity allows the indirect observation of the coexistence of regions of different interplanar turn angle through a reduction of the magnetic extinction.

From the above data, the $2/11$ structure appears to be stabilised in both higher and lower temperatures on the application of a b axis field. The stabilisation of the $2/11$ structure can also be understood through the reduction of the energy of the system by the Zeeman term . Hence on applying a b axis field this commensurate state will exist over an

extended temperature range, causing an abrupt change in turn angle at a given temperature. If the b axis field is sufficiently large then the situation can be envisaged where the $^{2}/_{11}$ structure will pass directly into the $^{1}/_{6}$ structure on reducing the temperature. It should be noted at this point that the application of this b axis field appeared to have no effect on the low temperature $^{1}/_{6}$ transition. This is not surprising as the $^{1}/_{6}$ structure does not have a net basal plane moment which will restrict the energy reduction through the Zeeman term.

The c axis magnetisation data of figure 6.5 shows an anomalous maximum which migrates to lower temperatures on applying a c axis field (as previously seen for the transition to a $^{1}/_{6}$ structure in the neutron diffraction data of figure 6.9). This increase in magnetisation is due to the presence of the $^{2}/_{11}$ lock in structure which is believed to contain the c axis ferromagnetic component of the conical phase. Moreover we propose here that the appearance of the $^{2}/_{11}$ structure actually signifies the onset of the conical transition.

On increasing the c axis field the minimum which separates the anomalous boss from the low temperature steady increase in magnetisation is observed to decrease in magnitude. The minimum is believed to result from the incommensurate wave vector states, which show no c axis moment and exist between the $^{1}/_{6}$ and $^{2}/_{11}$ structures. This incommensurate region has already been seen to diminish on the application of small b axis fields ($2.5 .10^{-2}$ Tesla) due to the increase of the $^{2}/_{11}$ structure. The stabilization of the $^{2}/_{11}$ structure could arise from a misalignment of the sample along the c axis (normally this is of the order of three degrees when done by eye), which would produced an applied field component along the b axis. Thus on increasing the c axis field the $^{2}/_{11}$ structure can be stabilized until all the incommensurate phase has been eliminated (the removal of the minimum in magnetisation seen in figure 6.5).

Both the magnetic neutron diffraction (figure 6.6) and magnetisation data show thermal hysteresis around the lock in transition to the $^{1}/_{6}$ structure (the rise in

magnetisation below the minimum in the magnetisation data). The presence of hysteresis indicates that the low temperature transition to a lock in structure is first order. However, the onset of the conical phase (seen as the gradual increase of the magnetisation in figure 6.7) does not appear to be quite so abrupt and could even be described as second order. Unfortunately, the poor statistics of the onset of the c axis component from the 110 neutron diffraction data do not allow the confirmation of this result, but all the same they do not contradict this idea.

6.5 Speculations and future experiments.

The speculation that the increase in the magnetic satellite width corresponds to the coexistence of two different propagation vector states within the sample can be easily verified. A series of high resolution neutron diffraction scans (omega-two theta, with a tightly collimated detector) carried out on the $002\pm\tau$ magnetic satellite would indicate whether the previously observed increase in width could be separated into two distinct contributions. From the previous results of figure 6.9 these two contributions are expected to be centered at propagation vector values which correspond to an interplanar turn angle of 30.0 and 32.2 degrees respectively. Unfortunately this experiment was not possible as a result of the untimely shut down of the high flux reactor at the Institute Laue-Langevin in April 1991.

A second experiment is proposed in order to resolve any questions about the stabilisation of the $2/11$ phase by either a c or a b axis component in the magnetisation data. The proposed experiment would allow the sample magnetisation to be detected as a function of the angle of tilt of both the c and b axes away from the direction of the applied field. In this manner the b axis component of the applied field can either be reduced to a minimum value or its effect on the magnetisation data could be studied quantatively.

CHAPTER SEVEN

ACTING ON CHIRALITY DOMAINS.

7.1 Introduction.

The chirality domain structure of a helimagnetic material is sensitive to a large number of external factors. It has already been stated in chapter one that their shape is primarily dependent on their thermal history, with striped "F" domains (perpendicular to the helical axis and parallel to the magnetisation of the ferromagnetic phase) being formed on entering the helical phase from the ferromagnetic phase and randomly shaped "P" domains on passing from the paramagnetic phase. The size of both of these domain structures has been shown by Palmer et al. (1986) to be dependent on the samples crystalline purity. In the same publication Palmer et al. also showed that by diffusing impurities into a terbium sample the characteristic memory effect of a chirality domain structure can be modified, but as before at the cost of reducing the average domain size.

The relative domain populations of the two enantiomorphs are generally equally occupied, but exceptions have been observed where the population ratios have been as high as three to one. This asymmetry was observed by Drillat (1983) and is thought to be due to the local interaction of the helical structure with crystalline defects.

The application of a uniaxial stress also reduces the average chirality domain size (ACDS) as reported by Patterson et al (1985). The application of a magnetic field in the ferromagnetic phase and during the transition to a helical phase led to a ten fold increase in the average chirality domain size. This increase in ACDS was explained as the removal of Bloch walls in the ferromagnetic phase on the application of a magnetic field. The Bloch

walls are known nucleation centres, and hence a reduction of their frequency will increase the average "F" chirality domain size (Baruchel et al. 1988b).

In this investigation the average chirality domain size is monitored as a function of thermal cycling within the helimagnetic phase. The change in chirality domain size is inferred through a local modification of the extinction effects around domain walls. This variation of the secondary extinction parameter (y) is calculated for the variation of the integrated intensity of the magnetic satellite reflections, where the diffracted intensity is described by the kinematic theory of diffraction. The magnetic extinction parameter is defined in this case for a type II sample (equation 53), as proposed in the secondary extinction model of Zachariasen (1967). A mechanism for domain wall movement and ultimately domain removal will be proposed as a function of thermal cycling.

7.2 Thermal cycling within the helimagnetic phase of MnP.

A manganese phosphide, (a,c) platelet sample was thermally cycled in the helimagnetic phase from 11K to 45K using a "Displex" closed cycle cooler. The peak intensity values of the 2+τ 00 magnetic satellite intensity were detected as a function of the thermal cycling. These intensity values were expressed as a ratio with the intensity detected by the white beam monitor, thus reducing the error caused by main beam fluctuations. Each measurement of the peak intensity was taken at 11K in an incident 1.7Å monochromatic beam as produced by a 111 Heusler alloy monochromator. The neutron polarisation was set in the vertical plane so that the neutron beam behaved, for this particular experiment like an unpolarised beam. These results are plotted in Figure 7.1, showing a reduction in the peak magnetic satellite intensity on repeated thermal cycling. A reduction of the peak intensity does not necessarily imply a reduction of the integrated intensity. Consequently, the integrated intensity was recorded for the 2±τ 00 magnetic satellites and the 200 nuclear peak in the same experimental conditions as described for the peak intensity measurements of figure 7.1. The integrated intensity results are illustrated in figure 7.2 as the ratio of the average integrated intensity of the two magnetic satellites to

Figure 7.1. The ratios of the intensity detected on the 200-τ magnetic satellite and the white beam monitor as a function of thermal cycling.

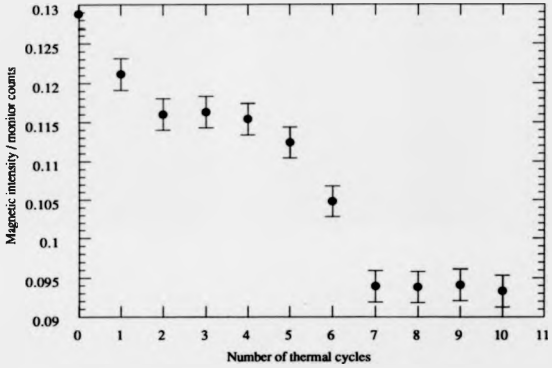

Figure 7.2: The ratios of the integrated intensities of the average of the magnetic satellites to that of the nuclear reflection as a function of the number of thermal cycles for the 002 reflections of the (b,c) MnP platelet.

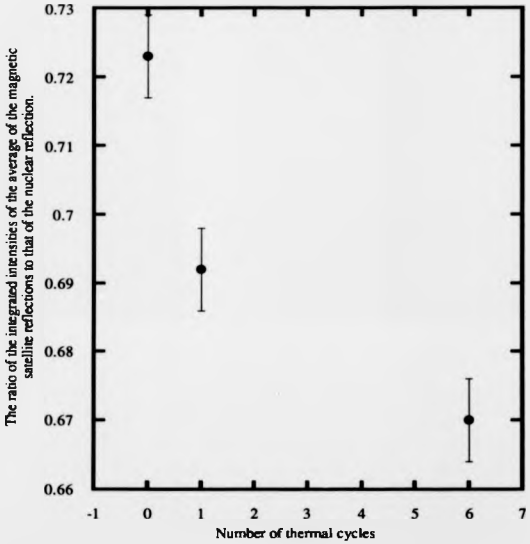

that of the nuclear reflection. This integrated intensity ratio was reduced on repeated thermal cycling just as in the case of the peak intensity values.

No observable differences in the chirality domain size was recorded on a series of neutron topographs taken as a function of thermal cycling with a horizontal neutron polarisation (in order to enable the chirality domains to be directly imaged). The integrated intensity of the nuclear reflection was measured as constant to within the beam fluctuation on thermally cycling the sample.

7.2a Discussion.

The gradual reduction of the magnetic integrated intensity was thought to be caused by an increase in secondary extinction within the sample, associated to an increase in the average chirality domain size. The detected intensity can be related to the frequency of domain walls by considering the possible beam paths of a neutron incident on a sample which is divided into domains (figure 7.3). The neutron path at "a" will pass through a single domain, whilst at "b" it will pass through two domains, by traversing a domain wall as indicated at "c". Since a given chirality domain will diffract only one neutron polarisation then each domain will receive an incident intensity of $I_o/2$, where I_o is the total incident intensity. The diffracted intensity for the case "a" where the neutron crosses a single domain will be proportional to

$$I_{a1} \propto R_A(t) \frac{I_0}{2} \qquad (74)$$

where (t) is the neutron beam path within the crystal and R_A is the reflectivity of the chirality domain "A". The diffracted intensity related to the neutron path which crosses the domain wall at "c" is proportional to the sum of the intensities diffracted by the domains A and B (which are incoherent as they correspond to different neutron polarisations), and is given by

$$I_{a2} \propto \left(R_A(t_1) + R_B(t_2) \right) \frac{I_0}{2} \qquad (75)$$

Figure 7.3: The possible neutron beam paths taken in a sample which is divided into domains.

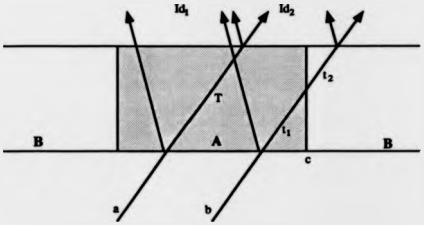

Figure 7.4: The dependence of the diffracted intensity on the neutron path length in the crystal on passing through a single domain and on traversing a domain wall.

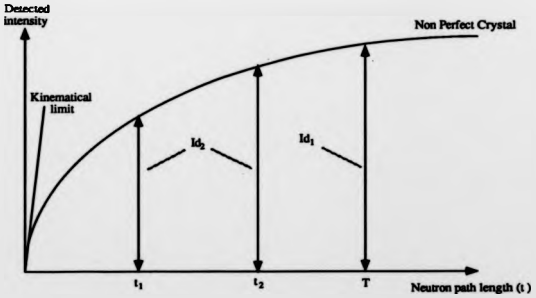

From the graph (figure 7.4) of the diffracted intensity versus the crystal thickness for an imperfect crystal it is clear that

$$I_{a2} > I_{a1} \qquad (76)$$

Thus by increasing the ACDS the frequency of domain walls will be reduced and this produces a reduction of the integrated intensity detected at the magnetic satellite positions. The invariance of the nuclear integrated intensity on thermal cycling is consistent with this proposed purely magnetic extinction effect.

A room temperature topograph of the 200 nuclear reflection (figure 7.5) was taken in order to assess the crystalline quality of the manganese phosphide (a,c) platelet. The total reflectivity ($\mathcal{R}_N$) detected on the topograph of the 200 nuclear reflection of figure 7.5 can be expressed as,

$$\mathcal{R}_N = \left[(1 - \alpha)\, \mathcal{R}_D + \alpha\, d\, Q_N \right] . \exp - \mu t \qquad (77)$$

where α is the percentage of the sample area which diffracts kinematically, μ is the absorption coefficient, t is the neutron path length in the sample, d is the thickness of the kinematical region and Q_N is the kinematical reflecting power. From the topograph of figure 7.5 it was assumed that the most intense regions (as seen at the base and along the right hand edge of the sample) were diffracting in the kinematical approximation, whilst the remainder of the sample diffracted a reduced intensity which can be described by the dynamical diffraction theory. Thus approximately 91% of the samples surface area was assumed to diffract kinematically with the remaining 9% being described by the dynamical diffraction.

The thickness of the kinematical region was not known and hence was left as a free parameter. The nuclear reflectivity of the sample ($\mathcal{R}_N$) is calculated from the following experimentally measured quantities,

Figure 7.5: A neutron diffraction topograph taken on the 200 nuclear reflection of an (a,c) manganese phosphide, platelet sample at room temperature.

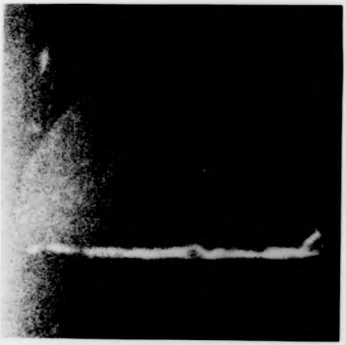

$$\mathcal{R}_N = \frac{I_N \cdot \Delta\omega}{I_o} \qquad (78)$$

where I_N is the integrated intensity of the nuclear peak, $\Delta\omega$ is the detector step size, and I_o is the incident intensity received at the sample surface. The value of I_o was corrected for the deadtime of the ^{3}He detector by using a cadmium attenuator.

The dynamical reflectivity ($\mathcal{R}_D$), is defined by

$$\mathcal{R}_D = \frac{\lambda^2 |F_N|}{\sqrt{\sin 2\theta}} \qquad (79)$$

which shows the characteristic $|F_N|$ dependency of the dynamical theory as opposed to the $|F_N|^2$ dependency of the kinematic approximation.

Substituting the physical values of these quantities into equation (77) produces a depth of 348 μm for the kinematical region. This depth is very close to the thickness of the manganese phosphide sample (measured to be 400 ± 5 μm), and thus by adjusting the dynamical proportion of the surface area of the sample to 8% then the kinematical region will occupy the whole of the crystal thickness.

Having verified that the majority (92%) of the crystal surface cannot be described by the kinematical theory of diffraction it is now clear that the diffraction properties of the sample should be described under the constraints of an extinction theory. Moreover when detecting from a purely magnetic reflection the kinematical region previously observed on the nuclear topography (a result of fracture and surface damage) will no longer be present. Hence the whole sample can be treated by a universal extinction parameter and one which will be solely dependent on the magnetic diffraction of the sample.

The measured reflectivity of a magnetic satellite can now be described by the kinematical reflectivity multiplied by a secondary extinction coefficient (y) as shown below,

$$\mathcal{R}_{EXP} = \mathcal{R}_{KIN} \cdot y = Q\left[\frac{1 - \exp -(\mu t)}{\mu}\right] \cdot y \qquad (80).$$

On substituting the expressions for the kinematical reflecting power (equation 40) and the secondary extinction coefficient for a type II sample (equations 51 to 53), the measured reflectivity can be written as,

$$\mathcal{R}_{EXP} = \frac{|F|^2 \lambda^3}{V^2 \sin 2\theta} x \left[\frac{1 - \exp - (\mu t_0 / \sin\theta)}{\mu}\right] x \frac{1}{\sqrt{1 + \frac{2 |F|^2 t_0 R \lambda^2}{V^2 \sin\theta}}} \qquad (81).$$

The value of $\mathcal{R}_{EXP}$ can be calculated from equation (78) by using the integrated intensity of the magnetic satellites. Thus by substituting $\mathcal{R}_{EXP}$ into the above equation it is possible to determine an experimental value of the block size parameter (R), which in this case represents the ACDS.

The variation of the measured, magnetic, integrated intensities indicated an increase in the ACDS from 8μm to 10μm on increasing the number of thermal cycles from zero to six (figure 7.6). This predicted increase in the ACDS cannot be experimentally verified by directly imaging the domains, due to the experimental resolution limit (60 μm) of the instrument S20.

The acceptance of an increase in the ACDS not only implies that the domain walls move on thermal cycling but also that a number of domains are eliminated from the original domain structure. A mechanism for this domain loss process is proposed as a function of the temperature variation of the pitch of the helix.

7.3 A proposed mechanism for domain loss.

For the elementary case of two domains which have their position and magnetic moment direction pinned at the two extremities of the system (x_0 and x_2) a simple geometrical argument can be used to describe domain wall movement. Two such chirality

Figure 7.6: The variation in the average chirality domain size (ACDS) as a function of thermal cycling as proposed by a secondary extinction treatment.

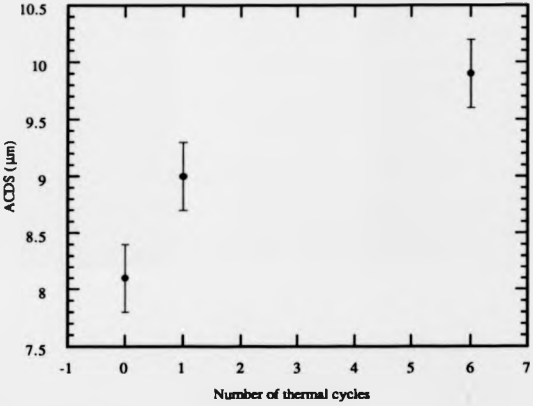

domains are illustrated in Figure 7.7, where the three domain walls are perpendicular to the propagation vector of the helix (τ) as observed in the previously described "F" type chirality domains which corresponds to the case of manganese phosphide. The positions of the three domain walls (W_0, W_1 and W_2), are given as x_o, x_1 and x_2 of which only x_1 is allowed to change its value.

On changing the temperature of the sample the propagation vector of the helix will pass from τ_0 to τ_1. In order that domains A and B are matched at the domain wall this implies that the domain wall at x_1 moves to x_1'. This process is reversible and hence by reversing the temperature change the value of τ will be reduced and the domain wall will move back in the opposite direction.

The population of the sample by the domain types A and B can be described by the population parameter (P) which is equivalent to the volume of domain type A minus the volume of domain type B. By assuming that the total change in turn angle $\Delta\phi$ is constant (due to the pinning of the magnetic moment direction at the sample extremity) it is possible to define P in terms of τ as shown below.

$$P = (x_1 - x_o) - (x_2 - x_1) \quad \text{and } \Delta\phi = \phi_2 - \phi_0$$

But
$$\phi_2 - \phi_0 = (x_1 - x_o)\tau - (x_2 - x_1)\tau = P\tau \tag{82}$$

therefore,
$$P = \frac{\Delta\phi}{\tau} \tag{83}$$

In this particular case where x_o and x_2 are fixed then the position of x_1 is solely determined by the propagation vector (τ). Hence increasing τ as shown in figure 7.7 will have the effect of reducing the population parameter to zero, where the sample will be equally populated by domains of type A and type B. By reducing τ the population parameter will increase, i.e. one of the two domains will be favoured with respect to the other.

Figure 7.7: A schematic representation of a helimagnetic sample containing two chirality domains which are separated by a domain wall at W_1.

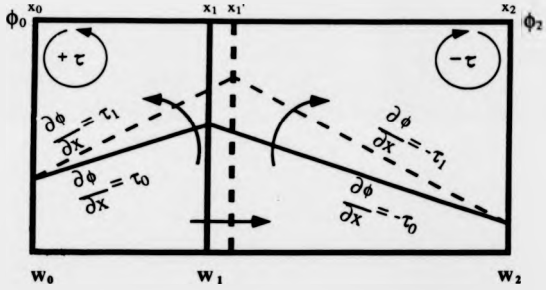

Although the preferential population of a given domain is dependent on the sign of the temperature variation of the turn angle, by thermally cycling the sample both dependencies can be satisfied. Consequently this mechanism for domain wall movement can be used to describe both positive and negative temperature dependencies of the interplanar turn angle as seen in terbium and manganese phosphide respectively.

If the population parameter of the chirality domains reaches zero during the thermal cycling when the sample will be equally divided into the two domains, then further domain wall movement will not be possible as the optimum position of the system will have been reached. In a multiple domain structure this situation is less likely to arise than in the simple two domain system described above. Even though the average population parameter will be very close to zero (as seen from flipping ratio measurements), there will be large localised variations from this limiting case which promote domain wall movement. If a domain wall is sufficiently displaced so that it is superimposed over a second domain wall then the domain which existed between these two walls is deemed to have been annihilated. Within this mechanism there is no possibility for the lost domain to be recreated or for any new domains to be created.

Equation (83) only describes a simple two domain system. In order to describe a multiple domain structure (as mentioned above), it would be sensible to introduce a positional energy for each domain wall instead of fixing their positions and orientations. In this case Sandonis et al. (1991) have shown that it was necessary to solve a series of nonlinear equations in order to describe domain wall movement. Just as in the simple two domain case the magnetic moment orientation in two neighbouring domains should be matched at the domain wall boundary. This condition can be represented in the following way,

$$\phi_i = \phi_{i-1} + (-1)^{i-1}\ \tau\ (x_i - x_{i-1}) \qquad i = 1,\ldots,N \tag{84}$$

The position of the domain walls and their moment orientation at equilibrium are described by the following two equations

$$\frac{\partial S(\phi_0)}{\partial \phi} + \frac{\partial S(\phi_N)}{\partial \phi} + \sum_{k=1}^{N-1} \frac{\partial V(x_k,\phi_k)}{\partial \phi} = 0 \qquad (85)$$

$$(-1)^{i-1}\tau\left[\frac{\partial S(\phi_0)}{\partial \phi} + \frac{\partial S(\phi_N)}{\partial \phi} + \sum_{k=1}^{i-1} \frac{\partial V(x_k,\phi_k)}{\partial \phi} - \sum_{k=i+1}^{N-1} \frac{\partial V(x_k,\phi_k)}{\partial \phi}\right] + \frac{\partial V(x_i,\phi_i)}{\partial \phi} = 0 \qquad (86)$$

where x_0 & x_N are the positions of the crystal extremities and x_i are the indices of the domain walls where i ranges from 1 to N-1. The orientations of the magnetic moments at these domain wall positions are given by ϕ_i where i has a range from 1 to N. The surface anisotropy term at the sample edges $S(\phi)$, is dependent on the magnetic moment orientation. The internal energy related to each domain wall ($V(\phi,x)$) is dependent on both their position and magnetic moment orientation.

The domain structure is treated as a quasi-static system by incrementing the temperature and calculating its effect on the interplanar turn angle and the resultant domain wall movement. After each iteration the values of ϕ and x were updated and the next temperature increment was applied. The thermal fluctuations were assumed to be very small in comparison to the energy of the system, as the domain walls were considered to be a single entity and not a summation of independently influenced sections.

The equations 85 and 86 were solved numerically using a Newton's method based routine of the Macintosh software package of MATHEMATICA. The results were used to model a 1mm long sample in the particular case where the anisotropy was represented as $S(\phi) = -\cos^2(\phi)$ and the internal domain wall energy as $V(\phi,x) = S(\phi)$. The propagation vector was varied from 0.1 to 0.06Å^{-1} which corresponds to half of a thermal cycle.

From the results shown in figure 7.8. one of the original domains has been lost due to an increase in the population parameter. On reversing the temperature direction the domain walls will move in the opposite direction, but the domain which was lost will not be recreated as the sample will now be at a lower energy state. After reducing the non-linear equation system to account for the loss of a domain, continued thermal cycling can reduce further still the number of chirality domain in the sample. Hence it has been shown that through cycling in temperature the ACDS can either remain constant or increase, but it can not decrease.

However there are still several problems remaining to be solved regarding the nucleation and memory effects observed in chirality domains.

Figure 7.8: A three dimensional representation of the evolution of the chirality domain configuration of a helimagnetic sample on the variation of the propagation vector (τ) in half a thermal.

CONCLUSIONS

Throughout the topography results presented in this work it is clear that in order to produce a clear image of either the magnetic domain structure or the phase coexistence the sample should ideally be a platelet shaped high quality single crystal of high purity and homogeous chemical structure. The experiments reported in this thesis provide examples of the importance of each of these sample characteristics.

Sample impurities and compositional inhomogenieties can have very strange effects on the magnetic behaviour of some crystals as seen for the (a,b) manganese phosphide and Cr-0.6 at. % Si samples which both contained a series of precipitation centres. In the case of MnP these precipitation centres formed nucleation points for the ferromagnetic phase within the parent helimagnetic phase. Moreover the strains induced by these precipitates in the crystalline lattice stabilised the ferromagnetic regions predominantly along the a axis of the sample. These elongated regions were observed to influence the migration of the phase boundary on the application of a temperature gradient. A second example of such an effect is the variation of silicon content within the Cr-0.6 at. % Si samples. A combination of neutron diffraction and topography techniques were used to show that the broadening of the first order transitions of this system was a result of a silicon inhomogeneity in the sample and compositional analysis of the same sample quantitively confirmed this variation of the silicon concentration.

The requirement that the sample should be in the form of a thin platelet allows the analysis of all the anisotropy effects of the crystal. The magnetostatic anisotropy was investigated in manganese phosphide through the effect of the variation of the direction of applied field in the (b,c) plane on the low temperature triple point in manganese phosphide. In the case of increasing the b axis field the fan phase was nucleated in the helimagnetic-ferromagnetic phase boundary. But on increasing the c axis component of

the applied field the helimagnetic to ferromagnetic transition occurs before reaching the triple point. In this case the triple point can only be reached (under a temperature gradient) by increasing the field and physically driving the fan phase through the ferromagnetic one.

The orientation of two of the three phase boundaries (Ferro-Heli and Fan-Ferro) can be understood through their associated elastic and magnetostatic energy terms. However the size, shape and orientation of the Heli-Fan phase boundary is not understood. Further investigations are proposed for this interface in reduced temperature and applied field gradients. If both gradients are reduced as much as possible and the triple point imaged then the angles between phase boundaries at the triple point will be proportional to their relative energies.

The final constraint that the sample should be a high quality single crystal leads to the analysis of the majority of the integrated intensity measurements of these samples by extinction theories. Whilst in most diffraction experiments extinction is thought of as a nuisance, in topography it is frequently used as an extra tool to extract data from integrated intensity measurements.

In manganese phosphide the reduction in magnetic integrated intensity on thermally cycling the sample was modelled using the mosaic block model to describe an increase in the average chirality domain size (ACDS). A mechanism was then proposed for the removal of chirality domain walls (increasing the ACDS) on thermally cycling within the helimagnetic phase. This model is dependent on the temperature variation of the interplanar turn angle and the relative pinning of domain walls through interactions with the defect and impurity structure of the sample. A simple experimental test can be applied by thermally cycling a holmium sample in a fixed propagation vector state (the $^1/_6$ lock in structure) in which case no evidence of an increase in the ACDS should be seen.

The complex magnetic structure of holmium in the region of 20K has been described in terms of the commensurate $^1/_6$ and $^2/_{11}$ lock in structures proposed by the

spin slip model of Bohr et al. (1985). The increase in the integrated intensity measured on the magnetic reflections of holmium is thought to result from the coexistence of regions of the sample which exhibit two different interplanar turn angles. Further investigations are proposed to clarify this point by carrying out an accurate omega two theta scan on the $002\pm\tau$ satellites with a tight slit collimation at the detector and a monochromator of minimal mosaic spread. The appearance of two distinguishable peaks in the width of the magnetic satellite will prove that the increase in intensity is due to the coexistence of two different interplanar turn angles.

Complementary magnetisation measurements on holmium have shown the presence of a c axis component of the magnetic moment in both of the above mentioned commensurate structures. The spontaneous magnetisation of holmium was measured to be around 1.53 ± 0.1 μ_B/atom which was very close to the value previously measured by Koehler et al. (1967). These magnetisation measurements show a field dependent minimum which has been attributed to the presence of incommensurate spin slip structures between the $^1/_6$ and $^2/_{11}$ commensurate regions.

Following a description of the general characteristics of sample requirements for topography a brief resume of the results presented in this thesis has been given. Each specific investigation primarily illustrates the ability of neutron diffraction and topography to observe the magnetic phase coexistence, domain structure and phase transition behaviour in magnetic materials. These observations have been supported by several complementary measurement techniques and some of these (magnetisation and compositional analysis) have allowed a quantitative description of the results. In each case these additional techniques have helped provide a more balalnced understanding of the magnetic properties of materials.

REFERENCES

Ando M. and Hosoya S.,
J. Appl. Phys., **49**, 6045 (1978).

Arajo S., Anderson E.E. and Ebert E.E.,
Il Nuovo Cimento, **4B**, 40 (1971).

Armstrong R.W.,
in "Characterisation of Crystal Growth Defects by X-Ray Methods",
Edited by B.K. Tanner and D.K. Bowen, NATO Advanced Study Institutes Series, Plenum Press, 349 (1980).

Authier A.,
Advances in X-ray Analysis, **10**, 9 (1967).

Bacon G.E. and Lowde R.D.,
Acta Cryst., **1**, 303 (1948).

Bacon G.E.,
Acta Cryst., **14**, 823 (1961).

Baruchel J., Schlenker M. and Roth W.L.,
J. Appl. Phys., **48**, 5 (1977).

Baruchel J.,
Ph.D. Thesis, University of Grenoble (1980).

Baruchel J., Palmer S.B. and Schlenker M.,
J. de Physique, **42**, 1279 (1981).

Baruchel J., Malgrange C. and Schlenker M.,
in "Position sensitive detection of Thermal Neutrons",
edited by J.B. Forsyth and P. Convert, Academic Press, London (1983).

Baruchel J., Patterson C. and Guigay J.P.,
Acta Cryst. A, **42**, 47 (1986).

Baruchel J., Patterson C. and Palmer S.B.,
Phil. Mag. B, **57**, 505 (1988).

Baruchel J., Palmer S.B. and Patterson C.,
J. de Physique, **49**, C8-1893 (1988)b.

Baruchel J. and Schlenker M.,
Physica B, **156 & 157**, 666 (1989).

Baruchel J., Schlenker M. and Palmer S.B.,
Nondestr. Test. Eval., **5**, 349 (1990).

Bar'yakhtar V.G., Bogdanov A.N. and Yablonski D.A.,
Sov. Phys. Solid State, **28**, 1876 (1986).

Bates S., Patterson C., McIntyre G.J., Palmer S.B., Mayer A., Cowley R.A. and Melville R.,
J. Phys. C : Solid State Phys., **21**, 4125 (1988).

Becerra C.C., Oliveira Jr. N.F. and Shapira Y.,
J. de Physique, **49**, C8-895 (1988).

Becker P.J. and Coppens P.,
Acta Cryst., **A30**, 129 (1974).

Batterman B.W. and Cole H.,
Reviews of modern Physics, **36**, 681 (1964).

Berger H.,
J. Appl. Phys., **34**, 1914 (1963).

Blume M.,
Phys. Rev., **130**, 1670 (1963).

Bohr J., Gibbs D., Moncton D.E. and D'Amico K.L.,
Physica, **140A**, 349 (1986).

Cable J.W.,
J. M. M. M., **5**, 112 (1977).

Cowley M.D. and Rosensweig R.E.,
J. Fluid Mech., **30**, 671 (1967).

Cowley R.A. and Bates S.,
J. Phys. C : Solid State Phys., **21**, 4113 (1988).

Cowley R.A., Jehan D.A., McMorrow D.F. and McIntyre G.J.,
Submitted to Phys. Rev. Letts. (1990).

Dachs H.,
Neutron Diffraction Topics in Current Physics, Vol. 6, Berlin, Springer Verlag (1978).

Darwin C.G.,
Phil. Mag., **43**, 800 (1922).

Dietrich O.W. and Als-Nielsen J.,
Phys. Rev., **162**, 315 (1967).

Doi K., Minakawa N., Motohashi H. and Masoki N.,
J. Appl. Cryst., **4**, 528 (1971).

Drillat A.,
PhD. Thesis, University of Grenoble (1983).

Drillat A., Baruchel J., Bates S. and Palmer S.B.,
J.M.M.M., **44**, 232 (1984).

El Kadiri M.,
PhD. Thesis, University of Grenoble (1986).

El Kadiri M., Baruchel J., Rodriguez F., Moreno M. and Henry J.Y.,
J.M.M.M., **54**, 853 (1986).

Endoh Y., Mizuki J. and Ishikawa Y.,
J. Phys. Soc. Japan **51**, 2826 (1982).

Enz U.,
Physica, **26**, 698 (1960).

Eshelby J.D.,
The Continuum Theory of Lattice Defects, Solid State Physics, **3**, Academic Press, New York, (1956).

Fawcett E., Holden T.M., Muir W.C. and de Camargo P.D.,
Sov. Phys. JETP, **67**, 646 (1988).

Fawcett E.,
Reviews of Modern Physics, **60**, 209 (1988).

Felcher G.P.,
J. Appl. Phys., **37**, 1056 (1966).

Felcher G.P., Lander G.H. and Brun T.O.,
J. de Physique, **C1**, 577, (1971).

Felcher G.P., Lander G.H., Arai T., Sinha S.K. and Spedding F.H.,
Phys. Rev. B., **13**, 3034 (1976).

Flippen R.B.,
J. Appl. Phys., **34**, 2026 (1963).

Forsyth J.B., Pickert S.J. and Brown P.J.,
Proc. Phys. Soc., **88**, 333 (1966).

Gerstein B.C., Griffel M., Jennings L.D., Miller R.E., Skochdopole R.E. and Spedding F.H.,
J. Chem. Phys., **27**, 394 (1957).

Gibbs D., Moncton D.E., D'Amico K.L., Bohr J. and Grier B.H.,
Phys. Rev. Lett., **55**, 234 (1985).

Hamilton W.C.,
Acta Cryst., **10**, 629 (1957).

Hegland D.E., Legvold S. and Spedding F.H.,
Phys. Rev., **131**, 158 (1963).

Hirahara E., Suzuki T. and Matsumura Y.,
J. Appl. Phys. **39**, 713 (1968).

Hiyamizu S. and Nagamiya T.,
Int. J. Magnetism, **2**, 33 (1971).

Huber Jr. E.E. and Ridgley D.H.,
Phys. Rev., **135**, A1033 (1964).

Hubert A.,
"Theorie der Domänenwände in geordneten Medien"
Ed. W. Beiglböck, Berlin, Heidelberg, N.Y. (1974).

Ishizaki A., Komatsubara T. and Hirahara E.,
Supp. of Prog. of Theo. Phys., **16**, 256 (1970).

Ishizaki A., Komatsubara T. and Hirahara E.,
J. Phys. Soc. Jpn., **30**, 292 (1971).

Izyumov Y.A.,
Sov. Phys. J.E.T.P., **15**, 1162 (1962).

Jensen J. and Mackintosh A.R.,
Phys. Rev. Lett., **64**, 2699 (1990).

Jiles D.C., Blackie G.N. and Palmer S.B.,
J.M.M.M., **24**, 75 (1981).

Jiles D.C., Palmer S.B., Jones D.W., Farrant S.P. and Gschneidner Jr. K.A.,
J. Phys. F : Met. Phys., **14**, 3061 (1984).

Joseph R.I. and Schlomann E.,
J. Appl. Phys., **36**, 1579 (1965).

Jourdan C., Gastaldi J. and Grange G.,
Acta Metall, **36**, 2979 (1988).

Kaczer J.,
Sov. Phys. JETP., **19**, 1204 (1964).

Kasuya T.,
Progress of Theoretical Physics **16**, 45 (1956).

Koehler W.C., Cable J.W., Wollan E.O. and Wilkinson M.K.,
J. Phys. Soc. Japan, **17**, Suppl. B-111, 32 (1962).

Koehler W.C., Child H.R., Wollan E.O. and Cable J.W.,
J. Appl. Phys., **34**, 1335 (1963).

Koehler W.C.,
J. Appl. Phys., **36**, 1078 (1965).

Koehler W.C., Cable J.W., Wilkinson M.K. and Wollan E.O.
Phys. Rev., **151**, 414 (1966).

Koehler W.C., Cable J.W., Child H.R., Wilkinson M.K. and Wollan E.O.,
Phys. Rev., **158**, 450 (1967).

Komatsubara T., Shinohara H. and Hirahara E.,
J. Appl. Phys., **40**, 1037 (1964).

Komatsubara T., Suzuki T. and Hirahara E.,
J. Phys. Soc. Jpn., **28**, 317 (1970).

Komatsubara T., Ishizaki A., Kusaka S. and Hirahara E.,
Solid State Commun., **14**, 741 (1974).

Kulda J.,
Acta Cryst., **A40**, 120 (1984).

Kulda J.,
Acta Cryst., **A43**, 167 (1987).

Kulda J.,
Acta Cryst., **A44**, 283 (1988).

Kulda J.,
Acta Cryst., **A44**, 286 (1988).

Kulda J.,
Submitted to Acta Cryst. A (1991).

Kulda J.,
Submitted to Acta Cryst. A (1991).

Lajzerowicz J. and Niez J.J.,
J. Physique Lett. **40**, L165 (1979).

Landau L.D. and Lifshitz E.M.,
Statistical Physics 3rd Edition Part 1, Pergamon Press, 289 (1986).

Lee M.C., Trader R.A. and Levy M.,
Phys. Lett. **A38**, 499 (1972).

Lee M.C., Trader R.A. and Levy M.,
J. Phys. Chem. Solids **36**, 1281 (1975).

MacKenna T.J.,
Ph.D Thesis, University of New South Wales, Australia (1980).

Mackintosh A.R.,
Phys. Today, 23 June (1977).

Malgrange C., Petroff J.F., Sauvage M., Zarka A. and Englander M.,
Phil. Mag., **33**, 743 (1976).

McMorrow D.F., Cowley B.A. and Jehan D.,
ILL Research Proposal (1991).

Mezei F.,
in "Imaging processes and coherence in physics", Proc. Les Houches, ed. by M. Schlenker et al. (1979).

Miltat J. and Sauvage-Simkin M.,
in "Applications of X-Ray Topographic Methods to Materials Science", Edited by S. Weissmann et al., Plenum Press, 185 (1984).

Mitsek A.I.,
Phys. Stat. Sol. (b), **59**, 309 (1973).

Mizuki J., Copley J.R.D., Endoh Y. and Ishikawa Y.,
J. Phys. F: Met. Phys., **16**, L195 (1986).

Moon R.M.,
J. Appl. Phys., **53**, 1956 (1982).

Munday B.C and Street R.,
J. Phys. F: Met. Phys., **1**, 498 (1971).

Nye J.F.,
"Physical Properties of Crystals" , Oxford University Press, 108 (1957).

Obara H., Endoh Y., Ishikawa Y. and Komatsubara T.,
J. Phys. Soc. Japan, **49**, 928 (1980).

Okamoto T., Kamigaichi T., Iwata N. and Tatsumoto E.,
J. Phys. Soc. Japan, **25**, 1730 (1968).

Palmer S.B.,
J. Phys. F : Metal Phys., **5**, 2370 (1975).

Palmer S.B., Jiles D.C. and Isci C.,
J. Physique Coll., **40**, C5 33 (1979).

Palmer S.B., Baruchel J., Drillat A., Patterson C. and Fort D.,
J.M.M.M., **54**, 1626 (1986).

Palmer S.B, Melville R.J. and Sousa J.B,
I.L.L. Experimental Reports, 228 (1988).

Patterson C., Palmer S.B., Baruchel J. and Ishikawa Y.,
Sol. Stat. Comm., **55**, 81 (1985).

Pechan M.J. and Stassis C.,
J. Appl. Phys., **55**, 1900 (1984).

Podkorytov V.N. and Yablonskii D.A.,
Sov. Phys. (Solid State), **25**, 634 (1983).

Rhodes B.L., Legvold S. and Spedding F.H.,
Phys. Rev., **109**, 1547 (1958).

Rhyne J.J. and Clark A.E.,
J. Appl. Phys., **38**, 1379 (1967).

Ruderman M.A. and Kittel C.,
Phys. Rev., **96**, 99 (1954).

Sabine T.M.,
Acta Cryst., **A44**, 368 (1988).

Sabine T.M.,
International Tables of Crystallography, Volume C (1990).

Sandonis J.,
Thesis to be submitted to Universidad de Santander (1991).

Sandonis J., Pearce A.S., Baruchel J., Parlinski K. and Palmer S.B.
Accepted by J.M.M.M. (1991).

Schlenker M. and Schull C.G.,
J. Appl. Phys., **44**, 4181 (1973).

Schlenker M. and Baruchel J.,
Physica, **137B**, 309 (1986).

Schlenker M.,
Notes from "HERCULES" (1991).

Shapira Y., Becerra C.C., Oliveira Jnr. N.F., and Chang T.S.,
Phys. Rev. B., **24**, 2780 (1981).

Shirane G. and Takei W.J,
J. Phys. Soc. Japan, **17**, 35 (1962).

Shirane G, Cowley R., Majkrzak C., Sokoloff J.B., Pagonis B., Perry C.H. and Ishikawa Y.,
Phys. Rev. B., **28**, 6251 (1983).

Simpson A.M., Jericho M.H. and Jain M.C.,
Can. J. of Phys., **54**, 1172 (1976).

Siratori K., Akimitsu J., Kita E. and Nishi M.,
J. Phys. Soc. Japan, **48**, 1111 (1980).

Sivardière J.,
Solid State Comm., **5**, 289 (1967).

Smith H.G.,
Rev. Sci. Inst., **34**, 914 (1962).

Squires G.L.,
"Introduction to the Theory of Thermal Neutron Scattering"
Cambridge University Press (1978).

Steinitz M.O.,
J. M. M. M. **60**, 137 (1986).

Steinitz M.O., Fawcett E., Windsor C.G, Wedgewood F.A. and Lowde R.D.,
Solid State Commun., **21**, 357 (1977).

Strandburg D.L., Legvold S. and Spedding F.H.
Phys. Rev., **127**, 2046 (1962).

Tachiki M., Lee M.C., Treder R.A. and Levy M.,
Solid St. Commun., **15**, 1071 (1974).

Thomas H. and Wolf P.,
Proceedings S731 de I.C.M. Nottingham (1964).

Tindall D.A., Steinitz M.O. and Plumer M.L.,
J. Phys. F : Metal Phys., **7**, L263 (1977).

Villian J.,
J. Phys. Chem. Solids, **11**, 303 (1959).

Wang S.P., Shull C.G. and Phillips W.C.,
Rev. Sci. Inst., **33**, 126 (1962).

Werner S.A.,
Acta Cryst., **A27**, 665 (1971).

Yosida K.,
Phys. Rev., 106, 893 (1957).

Zachariasen W.H.,
Acta Cryst., 23, 558 (1967).

Zachariasen W.H.,
Acta Cryst., A24, 421 (1968).

Publications arising from the work contained in this thesis

Baruchel J., Sandonis J. and Pearce A. S.,
Physica B, 156 & 157, 765 (1989).

Pearce A.S., Baruchel, J., Palmer S.B. and Sousa, J.B.,
Nondestr. Test. Eval., 5, 369 (1990).

Pearce A.S., Baruchel, J. and Palmer S.B.,
Physica B, 174, 121 (1991).

Sandonis J., Pearce A.S., Baruchel J., Parlinski K. and Palmer S.B.,
Accepted by J.M.M.M. (1991).

Sandonis J., Baruchel J., Schlenker M. and Pearce A. S.,
Accepted by J.M.M.M. (1991).